

**COUPLED PORE-TO-CONTINUUM MULTISCALE MODELING OF  
DYNAMIC PARTICLE FILTRATION PROCESSES IN POROUS  
MEDIA**

A Dissertation

Submitted to the Graduate Faculty of the  
Louisiana State University and  
Agricultural and Mechanical College  
in partial fulfillment of the  
requirements for the degree of  
Doctor of Philosophy

in

The Department of Petroleum Engineering

by

John Rayner Blears

B.S., Washington University in St. Louis, 2013

M.S., Louisiana State University, 2015

December 2019

This work is dedicated to my family and friends, whose support and sacrifices throughout my life have made this work possible.

## **Acknowledgements**

I would like to thank my committee members for their guidance and time spent during the research for this work. I am truly grateful for the opportunities you have given me, which greatly improved my analytical and communication skills. Specifically, I would like to thank Dr. Karsten Thompson for the opportunity to work under his guidance as a teaching assistant, masters candidate, and doctoral candidate. I also thank Dr. Richard Hughes and Dr. Mayank Tyagi for the opportunities they gave me to work as a teaching assistant and for their support in the research process.

My family and friends have given me the support and encouragement needed to undertake and complete this work. I am extremely grateful to my parents for their dedication to my wellbeing and education. and to my siblings for their care and support. Also to Valentina Rosasco for being with me during the course of this work and to all my friends who have assisted me along the way, I thank you.

## Table of Contents

Acknowledgements .....	iii
Abstract .....	v
Chapter 1. Introduction .....	1
1.1. Overview .....	1
1.2. Applications .....	3
1.3. Experimental Observations .....	4
1.4. Continuum-scale Modeling .....	6
1.5. Pore-scale Modeling .....	9
1.6. Coupled Modeling .....	21
1.7. Objectives .....	24
Chapter 2. Technical Approach .....	25
2.1. Resources Available.....	25
2.2. Finite Difference Model .....	36
2.3. Finite Difference Model Verification and Validation.....	40
2.4. Concurrently Coupled Model .....	54
Chapter 3. Results and Discussion .....	55
3.1. One-Dimensional Concurrent Coupling .....	55
3.2. Three-Dimensional Concurrent Coupling.....	108
Conclusion .....	119
Appendix. Supplementary Input Data File for Chapter 3 .....	121
References .....	126
Vita.....	137

## Abstract

Modeling particle transport and retention in porous media is important in fields such as hydrocarbon extraction, groundwater filtration, and membrane separation. While the continuum-scale ( $>1$  m) is usually of practical interest, pore-scale (1-100  $\mu\text{m}$ ) dynamics govern the transport and retention of particles. Therefore, accurate modeling of continuum-scale behavior requires an effective incorporation of pore-scale dynamics. Due to current computational limits however, the large spatial and temporal discrepancies of these scales prohibit modeling an entire continuum-scale system as a single pore-scale model. Even if a pore-scale model could incorporate every pore contained in a continuum-scale system, an upscaling scheme that coupled pore- and continuum-scale models should in principle be more efficient and achieve acceptable accuracy. In this work, a continuum-scale model for particle transport and retention has been developed using the concurrent coupling method. In the model, pore network models (PNMs) were embedded within continuum-scale finite difference grid blocks. As simulations progressed the embedded PNMs periodically provided their continuum-scale grid blocks with updated petrophysical properties. The PNMs used a Lagrangian particle tracking method to identify particle dispersion and retention coefficients. Any changes in permeability and porosity due to particle trapping were also determined. Boundary conditions for the PNM simulations were prescribed by fluid velocity and influent particle concentration information from the continuum-scale grid blocks. Coupling in this manner allowed for a dynamic understanding of how particle induced changes at the pore-scale impact continuum-scale behavior.

# Chapter 1. Introduction

## 1.1. Overview

The study of particle transport and retention in porous media, also referred to as particle filtration in this work, has been ongoing since the 1960s and has a wide range of applications in multiple disciplines (Gao, 2008). Applications include water filtration (Yao et al., 1971), pathogen transport in groundwater (McDowell-Boyer et al., 1986), hydrocarbon reservoir damage (Gao, 2007), and transport of engineered nanoparticles (Molnar et al., 2015). For these and all other applications, a model capable of predicting how retention of particles will impact field-scale parameters would be highly useful. Such a model would aid in the design of effective treatments to mitigate or enhance particle retention, depending on the nature of the application. Analytical, experimental, and numerical methods, which have been used to understand the processes involved in particle filtration, have provided the foundation to develop predictive continuum-scale models. To date however, accurate models have been difficult to develop due to the complex pore geometry and multi-scale nature of porous media.

Particle filtration models can be categorized as either continuum-scale or pore-scale models. Continuum-scale models can be subsequently classified as trajectory analysis models or phenomenological models. Trajectory analysis models use force balances to compute particle trajectories and determine whether or not retention will occur (Imdakh and Sahimi, 1991). The porous media in these models is typically represented as a collection of so-called unit collectors which provide an attachment surface for suspended particles. While this configuration allows for semi-analytical solutions of fluid flow and particle trajectory, the underlying simplifications of the medium inhibit accurately modeling many systems of interest (Sahimi et al., 1990).

Alternatively, phenomenological models treat fluid and solid species concentrations as smooth functions of time and space and are primarily based on numerical solutions to various forms of the advection-dispersion equation (Sahimi et al., 1990). In phenomenological models, particle retention is typically accounted for with an additional term that uses a mass transfer rate coefficient. The mass transfer coefficients are typically empirically obtained from particle filtration core flooding experiments (Gao, 2008). Although simpler to utilize, phenomenological models make simplifying assumptions concerning microscopic properties of the porous medium and do not explicitly consider the mechanisms responsible for particle retention, such as particle size (Feng et al., 2015). These simplifications limit the practical usefulness of phenomenological models.

In contrast, pore-scale models determine particle retention by considering the forces and transport mechanisms acting on particles as they flow through a porous medium. Pore-scale models can be categorized as either direct models or pore network models (PNMs). Direct models solve the governing equations of transport and retention on direct representations of the porous medium (Mehmani and Balhoff, 2015a). Modern computed tomography (CT) imaging techniques, such as micro-CT scanning, have allowed for the generation of three-dimensional models of pore structure with resolutions of a few microns (Blunt et al., 2013). Fluid flow and particle retention can then be computed on models extracted directly from the pore-space images using numerical techniques, such as the Lattice Boltzmann Method (LBM) or the finite element method (FEM). The high

resolution and accuracy of modern direct pore-scale models however, is associated with large computational requirements. For systems containing tens or hundreds of interconnected pores, analytical complexities are compounded, causing the computational requirements needed to obtain solutions to become intractable (Tartakovsky et al., 2007).

In comparison, PNMs represent porous media as simplified networks of pores connected by throats. Both pores and throats are given simple geometries, with the most commonly used geometries being spheres for pores and cylinders for throats (Xiong et al., 2016). The simple geometries used in PNMs allow for analytical treatments, which greatly reduces computational demand compared to direct methods. This reduced computational demand allows for the simulation of larger, more statistically representative systems. Advanced PNMs have recently been developed specifically to model particle filtration and consider many transport and retention mechanisms, including hydraulic drag, gravity, electrostatic and van der Waals forces, Brownian motion, and surface roughness (Yang and Balhoff, 2017). Although these advanced PNMs are capable of accurately predicting particle retention at the core-scale (1-10 cm), limited efforts have been made to fully couple PNMs to continuum-scale models.

Most conventional approaches use PNM simulations to obtain continuum-scale parameters, such as permeability, which are then used as inputs to continuum-scale models. The purpose of this sequential coupling is to validate or replace the more costly and time-consuming results obtained from traditional core flooding experiments (Dakshinamurthy et al., 2014). Although the sequential approach can add value, approaches that fully couple pore-scale and continuum-scale simulators, referred to as hybrid multiscale models (Scheibe et al., 2007), provide more predictive power and accuracy. In one type of hybrid multiscale model, known as a concurrently coupled model, continuum-scale grid blocks are embedded with PNMs. The continuum-scale grid blocks periodically provide boundary condition information to the PNMs, which in turn provide continuum-scale parameters to the continuum-scale grid blocks. This two-way communication between the pore-scale and continuum-scale models allows for the spatial and temporal prediction of how particle retention will impact continuum-scale flow dynamics (Sheng and Thompson, 2013). In their work on multiphase immiscible displacements, Sheng and Thompson (2013) demonstrated the ability of a concurrently coupled model to incorporate pore-scale phenomena to model continuum-scale processes with an accuracy unobtainable through traditional methods. The concurrently coupled model of Sheng and Thompson (2013) however, was limited to one dimension and had less than five continuum-scale grid blocks that received updated property values from embedded pore-scale models. A more fundamental challenge that Sheng and Thompson (2013) observed was that discrepancies could arise between phase saturations in the finite difference grid cells and their embedded pore-scale models. Although the root cause of the discrepancies was determined to result from obtaining relative permeability values from steady state pore-scale simulations, no methodology was provided to constrain the models and resolve the inconsistency. Furthermore, unlike in this work, Sheng and Thompson (2013) did not provide a quantitative analysis of how model accuracy was impacted by the size discrepancy between continuum-scale grid blocks and their embedded pore-scale models.

French (2015) created a concurrently coupled PNM and continuum-scale reservoir simulator that captured changes in permeability caused by particle retention. The work demonstrated the importance of including pore-scale effects in the determination of continuum-scale parameters.

The model developed in that work however, was not shown to be capable of simulating a truly continuum-scale system. While most practical continuum-scale applications involve upwards of hundreds of continuum-scale grid blocks simulated in three-dimensional systems, the concurrently coupled system tested was one-dimensional and consisted of five continuum-scale grid blocks, each embedded with a single PNM of the same size. This work is thought to provide the first example of an efficient hybrid model capable of accurately modeling particle filtration at the continuum-scale by incorporating pore-scale processes.

## 1.2. Applications

Particle filtration is a field of study with a wide range of practical applications. A significant amount of research relevant to particle filtration has been dedicated to water and waste water filtration. Contaminants such as viruses and bacteria can migrate over significant distances in saturated soils and pollute groundwater drinking sources (Bouwer, 1984). Groundwater contamination by micro-organisms led to over 46 disease outbreaks and several deaths in the United States alone between the years 1998 and 2002 (John and Rose, 2005). Engineered nanoparticles originating from aerosols, exhaust emissions, and consumer products can also contaminate wells supplying drinking water and thereby threaten public health (Molnar et al., 2015). Considering that an estimated fifty percent of the world's drinking water originates as groundwater (United Nations, 2003), contaminant transport to and filtration out of groundwater are issues of great significance.

Damage to hydrocarbon bearing formations is another application of particle filtration that has generated much attention. Solids contained in drilling mud, added to increase its density, can penetrate permeable formations and lead to a build-up of a filter cake (McDowell-Boyer et al., 1986). Filter cake can significantly decrease the permeability of hydrocarbon bearing rock and thus reduce well productivity. Additionally, filter cake build-up can lead to differential drillpipe sticking and inhibition of well log interpretation (Ferguson and Klotz, 1954). Improved understanding and prediction of filter cake formation would allow for these deleterious effects to be mitigated.

The migration of particles in hydrocarbon reservoirs can also lead to permeability loss and decreased well performance. For production wells, damage is typically caused by preexisting fines, which are defined as loose or unconfined particles smaller than 37 microns that exist naturally in sandstone formations (Huang et al., 2008). Fines may become suspended in the fluid flowing towards a production well due to drag forces exerted by the fluid or due to changes in pH or salinity. Mobile fines may be retained and aggregate near the wellbore, thereby causing significant permeability loss over time. Fines not retained by the porous medium or by downhole filters, such as gravel packs, may enter the wellbore and severely damage production tubing and surface equipment (Salama, 1998).

Reduced efficiency of injection wells is often caused by particles suspended within the injected water. Although the concentration of particles in injection fluids is small, severe damage may occur because large quantities of water are utilized in most waterflooding and waste water disposal operations (Gao, 2008). In one case, five water injection wells in the Gulf of Mexico experienced a decline in injection rate from 7000 bbl/day to under 1000 bbl/day in only 200 days, despite the



injection water having been filtered to ten microns (Sharma et al., 1997). For that case, near wellbore retention of particles suspended in the injected water was determined to have been the main cause of the reduced injectivity.

The use of engineered nanoparticles to improve hydrocarbon exploration and production is a more recent area of interest (Bera and Belhaj, 2016). Ongoing research is investigating the potential usefulness of tracer-like nanoparticles, designed with detectable electromagnetic properties, being added to injection fluids and used as contrast agents (Rahmani et al., 2015). If successful, such nanoparticles could aid in mapping flood fronts and bypassed oil regions during waterflooding, and in characterizing fracture lengths and stimulated reservoir volumes during hydraulic fracturing. Encapsulated nanoparticles could also be used to transport and release chemical payloads deep in the reservoir. To improve conformance control for example, crosslinking agents could be encapsulated and used to divert flow from high permeability zones and into unswept hydrocarbon bearing zones (Zhang et al., 2009). While the aforementioned applications may involve different systems, particles, and objectives, all are dependent on similar underlying characteristics, and demonstrate the potential benefit of developing predictive continuum-scale models of particle filtration.

### 1.3. Experimental Observations

Experimental research has greatly aided the understanding of mechanisms that underlie particle transport and retention in porous media. Early studies used membrane filters to represent porous media, however the current standard approach involves the use of core flooding tests (Gao, 2007). Most researchers use an apparatus similar to that depicted in Figure 1.

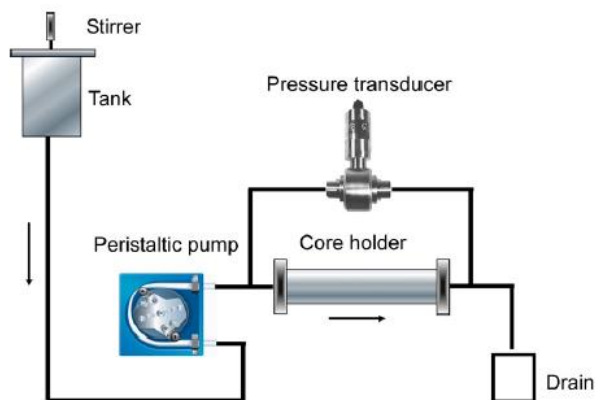


Figure 1. Standard core flooding experimental apparatus (Gao, 2007).

In core flooding experiments, particle suspension is achieved by mechanical stirring of a carrying fluid contained in a tank. The particle-fluid mixture is then pumped into a core sample whereupon particles are either retained by the core sample, or exit the sample in the effluent fluid. As the experiment progresses, a transducer records the inlet and outlet pressures. Pressure changes due to particle retention can then be related to the permeability decrease of the core sample. To determine

the extent of retention at different depths, additional pressure sensors may be placed along the core sample.

Todd et al. (1984) flooded sandstone cores with aluminum oxide particles to investigate the relationship between particle size and depth of retention. Particles less than 3 microns in diameter were found to be retained throughout the entire length of the 7.6 cm cores, while slightly larger particles with diameters of 4 to 6 microns exhibited more retention in the first 12 mm of the cores. The retention of larger particles of 8 to 10 microns in diameter was observed to decrease permeability by 90% in the first 5 mm of the cores and cause a filter cake to form on the core inlet. These observations demonstrated that a significant relationship exists between particle size and depth of particle transport.

The work of Vetter et al. (1987) used Berea sandstone cores and also found a relationship between particle size and depth of particle transport. Smaller particles, 0.05 to 7 microns, were observed to penetrate deeper into the core sample with a more gradual loss of permeability compared to larger particles. Larger particles caused shallower but more rapid permeability loss. Additionally, Vetter et al. (1987) studied the impacts of flow rate, particle concentration, and particle charge on retention. Lower flow rates were observed to cause greater permeability loss, while higher flow rates led to greater depth of transport. Higher concentrations of injected particles were observed to cause larger permeability losses. Particle charges were altered by adding surfactants to the flowing fluid, and were observed to have a significant impact on particle retention. Subsequent work by Baghdolkhan et al. (1989), who used a packed sand core injected with mostly sub-micron clay particles, validated the findings of Vetter et al. (1987).

The observations in these and other experimental studies demonstrate that particle retention can be attributed to three primary mechanisms: gravity settling, adsorption, and size exclusion. These three retention mechanisms are depicted in Figure 2.

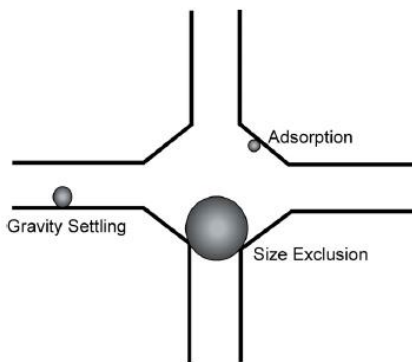


Figure 2. Particle retention mechanisms (Gao, 2007).

Gravity settling occurs when density differences between suspended particles and the surrounding fluid cause particles to interact with and become retained by the porous media. The observed increase in particle retention under lower velocity conditions can be mostly accounted for by

gravity settling (Gao, 2008). At lower velocities, gravitational forces dominate over hydrodynamic forces and thus retention through gravity settling dominates.

Electrostatic attraction between particles and media surfaces that leads to retention can be viewed as adsorption. The relationship between particle charge and retention observed by Vetter et al. (1987) and Baghdliklan et al. (1989) can be attributed to adsorption. If attractive forces exist between particle surface charges and those of the matrix surfaces, then retention through adsorption will normally occur (Molnar et al., 2015). Therefore, the presence of surfactants or other additives that change the charge properties of fluids can have a substantial impact on adsorption. Also, small particles are more likely to be retained at low velocities because Brownian motion dominates hydrodynamic forces. This makes particle contact with surfaces, and thus adsorption, more likely.

The dominant retention mechanism for larger particles is size exclusion, where particles are retained because they are too large to enter a pore throat (Sharma and Yortsos, 1987a). As observed by Todd et al. (1984), size exclusion can result in severe permeability loss with limited penetration into the formation. While experimental work has helped greatly in the understanding of retention mechanisms, any empirical formulation for particle retention is inherently limited to the range of conditions under which the experiments were conducted. Predicting retention behavior in novel systems requires a new set of experiments and is thus impractical. Numerical modeling provides a more practical way to investigate known particle retention mechanisms and thereby provide quantitative predictions of the effects of particle retention.

## 1.4. Continuum-scale Modeling

### 1.4.1. Phenomenological Modeling

Phenomenological models treat fluid and solid species concentrations as smooth functions of time and space and are primarily based on numerical solutions to various forms of the advection-dispersion equation (ADE) (Sahimi et al., 1990). The ADE is a partial differential equation that describes the transport of non-reactive solute concentrations in homogenous porous media. As demonstrated by Socolofsky and Jirka (2005), the ADE can be derived using a conservation of mass approach, which results in

$$\frac{\partial C^k}{\partial t} = \frac{\partial}{\partial x_i} \left( D_{ij} \frac{\partial C^k}{\partial x_j} \right) - \frac{\partial}{\partial x_i} (u_i C^k) \quad (1)$$

where  $C^k$ ,  $t$ ,  $D_{ij}$ , and  $u_i$  represent concentration of species  $k$ , time, hydrodynamic dispersion coefficient tensor, and interstitial velocity respectively.

Advection, which accounts for particle motion caused by the flow of the surrounding fluid, is modeled via the second term on the right side of Equation 1. Particle motion due to dispersion is modeled by the first term on the right hand of Equation 1. The hydrodynamic dispersion tensor quantifies the degree to which particles spread independent of advection. Hydrodynamic dispersion is caused by the combined effects of mechanical dispersion and molecular diffusion. Mechanical dispersion refers to the spreading of particles due to different flow velocities and flow

paths present in the porous media, whereas molecular diffusion refers to the spreading of particles due to concentration gradients. A commonly used formulation used to express the hydrodynamic dispersion tensor is that proposed by Bear (1972 and 1979)

$$D_{xx} = \alpha_L \frac{u_x^2}{|u|} + \alpha_T \frac{u_y^2}{|u|} + \alpha_T \frac{u_z^2}{|u|} + D^m \quad (2a)$$

$$D_{yy} = \alpha_L \frac{u_y^2}{|u|} + \alpha_T \frac{u_x^2}{|u|} + \alpha_T \frac{u_z^2}{|u|} + D^m \quad (2b)$$

$$D_{zz} = \alpha_L \frac{u_z^2}{|u|} + \alpha_T \frac{u_x^2}{|u|} + \alpha_T \frac{u_y^2}{|u|} + D^m \quad (2c)$$

$$D_{xy} = D_{yx} = (\alpha_L - \alpha_T) \frac{u_x u_y}{|u|} \quad (2d)$$

$$D_{xz} = D_{zx} = (\alpha_L - \alpha_T) \frac{u_x u_z}{|u|} \quad (2e)$$

$$D_{yz} = D_{zy} = (\alpha_L - \alpha_T) \frac{u_y u_z}{|u|} \quad (2f)$$

Where  $D_{xx}$ ,  $D_{yy}$ ,  $D_{zz}$  are the diagonal components of the dispersion tensor,  $D_{xy}$ ,  $D_{yz}$ ,  $D_{xz}$ ,  $D_{zx}$ ,  $D_{yz}$ ,  $D_{zy}$  are the off-diagonal components of the dispersion tensor,  $\alpha_L$  is longitudinal dispersivity,  $\alpha_T$  is transverse dispersivity,  $D^m$  is the molecular diffusion coefficient,  $u_x$ ,  $u_y$ ,  $u_z$  are the x, y, and z components of the velocity vector, and  $|u|$  is the velocity magnitude. Longitudinal and transverse dispersivity characterize particle spreading in the direction parallel to fluid flow, and in the direction orthogonal to fluid flow, respectively.

Experimental results have shown that transverse dispersivity is typically on the same order-of-magnitude as molecular diffusion (Cirpka et al., 2006), and at least an order-of-magnitude smaller than longitudinal dispersivity (Herrera, 2009). In many studies, transverse dispersivity and molecular diffusion are considered negligible compared to mechanical dispersion (Zheng and Wang, 1999). However, the effects of molecular diffusion and transverse dispersivity have been shown to become significant at low flow velocities (Bijeljic and Blunt, 2007).

To model particle filtration, additional terms can be added to Equation 1 that represent individual retention mechanisms. A commonly used approach is to express all retention mechanisms with a single term. As demonstrated by Soo and Radke (1986), particle filtration modeled through a single retention term can be written as

$$\frac{\partial C^k}{\partial t} = \frac{\partial}{\partial x_i} \left( D_{ij} \frac{\partial C^k}{\partial x_j} \right) - \frac{\partial}{\partial x_i} (u_i C^k) - k_r C^k \quad (3)$$

The retention coefficient,  $k_r$ , accounts for all mechanisms of particle retention and is typically obtained by analyzing effluent concentration data from core flooding experiments (Gao, 2008).

Experimental studies, such as those of Tufenkji and Elimelech (2004) and Porubcan and Xu (2010), have shown that the single-coefficient model of particle transport, given by Equation 3, can accurately describe particle transport in systems where adsorption is the dominant retention mechanism and all particles are of uniform size. However, for systems in which adsorption is not the dominant retention mechanism, numerous experimental studies have demonstrated that the single-coefficient model overestimates the degree of particle retention (Molnar et al., 2015). Commonly encountered systems that are not dominated by adsorption include those containing micron-sized particles, where size exclusion often dominates transport behavior.

In their work, Tufenkji and Elimelech (2004) and Porubcan and Xu (2010) provided alternate retention models to the single-coefficient model of Equation 3. These models were shown to accurately predict transport behavior in systems with limited adsorption. Despite their improved accuracy, the alternate models introduced empirical coefficients dependent on the availability of supporting experimental data, thus limiting their utility. Furthermore, Xu and Saiers (2009) demonstrated that these models failed to predict transport behavior in systems involving particles of more than one size. Although Xu and Saiers (2009) were able to establish a phenomenological model that could predict transport in systems containing two particle sizes, the authors concluded that extending their model to polydisperse systems would require the introduction of many empirical parameters. This would compromise the usefulness of the model and indicated that future work should focus on developing more simplified models for the straining of polydisperse particle suspensions.

Whatever form of the ADE used, phenomenological models treat the continuum-scale system as an accumulation of representative elementary volumes (REV) (Bear, 1972). When numerically solving the ADE, particle concentration, and all other continuum-scale parameters, are treated as constant within each REV. Although the use of REV and empirically derived retention coefficients make phenomenological models relatively simple to utilize, the underlying assumptions, and need to fit experimental data to obtain key parameters, limit the usefulness of these models (Molnar et al., 2015). For example, if any parameter not directly accounted for by the model changes, such as the size of particles being filtered, a new retention coefficient must be empirically determined. An alternative approach called trajectory analysis, while introducing its own limitations, allows for more flexible modeling (Rajagopalan and Tien, 1976).

#### 1.4.2. Trajectory Analysis Modeling

Some of the earliest models of particle filtration in porous media, such as that proposed by Yao et al. (1971) in their work on colloid filtration theory (CFT), utilized trajectory analysis. In trajectory analysis, also commonly referred to as mechanistic modeling, the porous media is represented using a single collector upon the surface of which particles may be retained. These models assume that a continuum-scale system can be considered as a grouping of identical collectors and thus that pore-scale processes can be directly upscaled to the continuum-scale (Seetha et al., 2017). To simplify the determination of the flow field around the collector, the collector is usually given a spherical geometry and assumed to be surrounded by an infinite fluid (Sahimi et al., 1990). Once the flow field is specified, particle trajectories are determined by integrating a trajectory equation based on a force balance on the suspended particle. A particle is considered to be retained

irreversibly if its trajectory intercepts the collector. Trajectory analysis models do not track the paths of individual particles, but rather provide a correlation equation that can be used to determine an overall contact efficiency,  $\eta$ , defined as the fraction of particles that enter the system which contact the collector (Yao et al., 1971). The correlation equations are comprised of various dimensionless parameters and are determined by running the trajectory analysis models within a specified range of system conditions.

Multiple correlation equations for  $\eta$  have been proposed that use different collector geometries and incorporate different forces acting on particles. For example, Yao et al. (1971) included hydrodynamic and gravitational forces in their analysis, whereas Payatakes et al. (1973, 1974a, b) also incorporated electric double layer and London dispersion forces in their analysis. Over 10 such trajectory analysis models exist. A detailed review of the forces and geometries accounted for by these models, as well as their correlation equations for  $\eta$ , can be found in Molnar et al. (2015). The models can successfully predict  $\eta$  for micron-sized particles under “favorable” conditions, where electrostatic repulsion between particles and collection surfaces is negligible (Rajagopalan and Tien, 1976). For “unfavorable” conditions, where repulsive forces exist between particles and collection surfaces, trajectory analysis models erroneously underpredict particle retention (Elimelech and O’Melia, 1990). Unfavorable conditions represent most natural systems and attempts have been made to account for the reduction in contact efficiency resulting from repulsive electrostatic forces. Despite these efforts, a correlation equation for  $\eta$  under unfavorable conditions does not currently exist (Seetha et al., 2017). Trajectory analysis models, while useful in understanding the effects of pore-scale retention mechanisms, have additional limitations.

The models do not accurately account for Brownian diffusion, which has led to overpredictions of  $\eta$  for smaller particles whose movement is more influenced by diffusion (Long and Hilpert, 2009). The models also typically do not include mechanical straining as a retention mechanism, where a particle is retained because it is too large to enter a pore throat. This is a significant limitation for systems involving larger particles, where size exclusion is known to be a dominant retention mechanism (Rege and Fogler, 1987). Additionally, the use of simplified geometries for collectors, which neglect grain-grain contacts, leads to unrealistic flow field solutions and trajectory errors (Li et al., 2010). One of the most significant limitations of trajectory analysis models is that they only accurately determine the initial value of  $\eta$  for the system (Tien and Payatakes, 1979). The models do not account for the fact that as particles are retained, they can dramatically alter flow dynamics and continuum-scale properties. Such models are thus inadequate in their ability to reliably predict how key continuum-scale parameters, such as permeability, will change temporally as more and more particles are retained (Sahimi et al., 1990). The efforts to overcome the limitations of trajectory analysis methods has led to the development of models that more accurately represent geometries of individual pores and connections between pores.

## 1.5. Pore-scale Modeling

### 1.5.1. Direct Modeling

Direct pore-scale models solve the equations governing transport and retention using direct representations of the porous medium (Mehmani and Balhoff, 2015a). Recent technological advances have enabled high resolution models to be extracted directly from images of porous

media samples. The most commonly used imaging techniques for model extraction are micro-CT and synchrotron computed microtomography (Blunt et al., 2013). In these techniques, three-dimensional images of rock and fluid are generated by subjecting samples to X-rays at different angles and recording the level of absorption. Images containing  $1000^3$  to  $2000^3$  voxels with resolutions of a few microns are currently possible with samples of a few millimeters in length (Blunt et al., 2013). Voxels are the three-dimensional equivalent of pixels in two-dimensional space and are assigned grayscale intensity values proportional to the imaged material's density. High resolution images from micro-CT scanning allow for realistic three-dimensional models of porous media to be constructed without damaging the imaged sample. A detailed review of pore-scale imaging techniques and capabilities is provided by Wildenschild and Sheppard (2012).

Multiple processing steps are required to convert an image of a porous media sample into a digital three-dimensional model that can be used to simulate fluid flow. First, voxel data should be corrected to remove any artifacts from the imaging process, such as beam hardening artifacts (Wildenschild and Sheppard, 2012). Beam hardening occurs because all sources of X-rays currently used in imaging contain a spectrum of energies. Lower energy parts of the spectrum do not penetrate as deeply as high energy parts of the spectrum and thus are more readily absorbed at the sample surfaces. The resultant images thus appear to show greater hardness near their surfaces compared to their interiors. The effect can be mitigated by post-processing the voxel data (Iassonov and Tuller, 2010).

Following the removal of imaging artifacts, the image undergoes a process of segmentation in which voxels belonging to various phases of the porous media are identified and differentiated (Wildenschild and Sheppard, 2012). Segmentation typically classifies voxels as either belonging to a single fluid phase or the solid phase which constitutes the matrix of the porous medium, although additional fluid or solid phases can be identified. Numerous methods exist to perform image segmentation and a detailed review is provided by Iassonov et al. (2009). A simple but commonly used segmentation method is to define a threshold voxel intensity value above which voxels are classified as solid phase, and below which voxels are classified as fluid phase. Such thresholding methods may however produce poorly segmented images if significant amounts of noise in the voxel data exist and are not filtered in a pre-processing step (Wildenschild and Sheppard, 2012).

Once segmentation is complete, the image is finally evaluated for any remaining imaging artifacts requiring removal. These artifacts, such as a group of solid phase voxels suspended in fluid phase voxels, may occur from inadequate filtering of noise or from improper selection of a voxel intensity threshold value (Wildenschild and Sheppard, 2012). With segmentation and image artifact removal complete, the fluid phase may then be discretized so that fluid flow may be simulated.

Fluid flow and particle retention can be computed numerically on discretized fluid phase domains. Among the most popular numerical methods are the Lattice Boltzmann Method (LBM) and methods incorporating computational fluid dynamics (CFD) (Molnar et al., 2015). The LBM simulates fluid flow as a collision process between particles that represent fluid packets (Blunt et al., 2013). The main advantages of LBM are the use of Cartesian grids to represent irregular pore geometries (which eliminates the need to generate a numerical mesh) and efficiency, when run on parallel computing systems (Yang et al., 2015). In porous media applications, LBM has been

successfully used to calculate macroscopic properties of interest, such as permeability in single phase systems (Ahrenholz et al., 2006), capillary pressure curves in multi-phase systems (Pan et al., 2004), and relative permeabilities in multi-phase systems (Ramstad et al., 2009). Long and Hilpert (2009) used a LBM approach to study the filtration of diffusion dominated particles in random sphere packings.

CFD methods, such as the finite element method (FEM), calculate fluid flow on a discretized mesh by numerically solving the Navier-Stokes equations (Yang et al., 2015). The Navier-Stokes equations govern fluid flow and are derived from applying Newton's second law to a fluid system of constant mass. For incompressible Newtonian fluids in the absence of external forces the Navier-Stokes equations may be written as

$$\rho \left( \frac{\partial u}{\partial t} + u \cdot \nabla u \right) = -\nabla P + \mu \nabla^2 u \quad (4)$$

where  $\rho$ ,  $u$ ,  $P$ , and  $\mu$  represent fluid density, velocity field, pressure, and dynamic viscosity respectively. The two terms on the left side of Equation 4 represent inertial and convective forces, while the two terms on the right side correspond to pressure and viscous forces. For systems with Reynolds numbers much less than one, also known as creeping flow systems, inertial forces become negligible relative to viscous forces. Creeping flow systems are governed by the Stokes equations

$$\nabla P = \mu \nabla^2 u \quad (5)$$

and are solved in conjunction with the continuity equation, which represents conservation of mass

$$\frac{\partial \rho}{\partial t} + \nabla \cdot (\rho u) = 0 \quad (6)$$

For incompressible systems, the continuity equation becomes

$$\nabla \cdot u = 0 \quad (7)$$

Many systems of interest are associated with low flow rates that constitute creeping flow, such as transport in groundwater systems with no external pumping (Molnar et al., 2015).

Initial research using FEM to model fluid flow in porous media focused on simple two-dimensional geometry and sphere pack systems. Ghaddar (1995) calculated transverse permeability values using FEM in two-dimensional systems with cylindrical inclusions of uniform diameter. These results were compared with analytic solutions for creeping flow and found to be in good agreement in moderate and high porosity systems, but in poor agreement in low porosity systems. Fourar et al. (2004) used FEM to examine velocity profiles in homogenous sphere packings at various Reynolds numbers. Panfilov and Fourar (2006) applied FEM to the Navier-Stokes equations to calculate velocity profiles at high Reynolds numbers in a two-dimensional periodic channel representing an element of a porous medium.



The most recent FEM approaches have used unstructured tetrahedral meshes to model complex interfaces between solid and fluid phases present in porous media. The resolution of the unstructured mesh can be adjusted independently of the underlying resolution of the image's voxel data. This enables higher resolution in areas of interest, such as pore surfaces, and thus more accurate representations of pore geometries (Shen, 2014). Image resolutions on the order of nanometers can be achieved (Mayo et al., 2003). The two most common methods used for mesh generation are based on either Delaunay tessellation or the advancing front technique (Shen, 2014). Delaunay tessellation approaches begin with a point insertion step, where points are added to the domain until the desired mesh resolution is achieved. This is followed by a Delaunay construction step, where a unique set of non-intersecting tetrahedrons is constructed. The advancing front technique on the other hand, first applies a triangular mesh to the domain surface boundaries, and then iteratively constructs a tetrahedral mesh in the domain interior (Shen, 2014).

Lane and Thompson (2010) developed a robust unstructured tetrahedral meshing algorithm capable of generating meshes directly from three-dimensional rock images. This algorithm and FEM was used to model Stokes flow in a Berea sandstone sample. A characteristic scale for permeability of approximately 1mm was reported, and mesh coarsening was shown to effect simulated permeability and porosity values. Shen (2014) continued the work of Lane and Thompson (2010) and used an image-based FEM model to simulate flow in proppant packings and propped fractures. The effects of loading stress on fracture permeability, non-Darcy flow coefficient, void space geometry, and pore-level flow behavior were analyzed. Limited research has been performed that uses FEM to analyze particle transport and retention in porous media.

The FEM approach has the deficiency that the required meshes can be time consuming to generate. This is especially true for high resolution meshes that may contain millions of tetrahedral elements, although highly efficient mesh generation algorithms are a promising field of ongoing research (e.g., Geuzaine and Remacle, 2009). The utility of FEM in modeling particle filtration is currently limited to smaller particles, which are assumed to have a negligible impact on the flow field of the system. In principle, larger particles may be simulated, however each time a larger particle is retained, it may alter the flow field. Thus, accurate modeling would require the pressure field to be recalculated each time a particle is trapped, which could occur tens of thousands of times in a single simulation. Therefore, because solving the pressure field for large or high resolution meshes can be time consuming, computational constraints currently pose a significant challenge to modeling particle filtration using FEM, which limits its utility.

Even if the pressure field recalculation could be avoided, FEM and all other direct modeling methods are associated with large computational requirements. These computational requirements are due to the high levels of mesh resolution required to map the complex geometries contained in porous media. For systems containing tens or hundreds of interconnected pores in multiple directions, analytical complexities are compounded, causing computational requirements to become intractable (Tartakovsky et al., 2007). The desire to model larger more statistically representative systems has made network modeling a significant area of research in the field of pore-scale modeling.

### 1.5.2. Network modeling

In a pore network model (PNM), the void space of porous media is represented as a simplified network of pores connected by throats. The simple geometries used in PNMs allow for analytical treatments and greatly reduce the computational demand per unit volume simulated compared to direct methods. This reduced computational demand allows for the simulation of larger systems that incorporate more heterogeneity. The most commonly used geometries in PNMs are spheres for pores and cylinders for throats (Xiong et al., 2016).

Prior to the development of PNMs, the bundle-of-tubes model (which represents the porous media as a bundle of parallel capillary tubes) and the sphere pack model (which represents porous media as a collection of unconsolidated spheres) were used to model flow in porous media (Fatt, 1956). While the bundle-of-tubes model is conceptually simple and can be used to obtain several macroscopic properties, such as permeability and porosity, the lack of connections between tubes makes it perfectly anisotropic. This perfect anisotropy makes the bundle-of-tubes model dissimilar to most porous media, which tend to be mostly isotropic. Although the sphere pack model allowed for the derivation of equations for rock properties, such as the Carman-Kozeny equation (Kozeny, 1927) which relates porosity to permeability, its simplicity resulted in calculated values for rock properties that poorly matched many experimentally observed results (Fatt, 1956). Furthermore, the sphere pack model retained complications that made it unsuitable for theoretical study at the time (Fatt, 1956).

Fatt (1956) proposed the first PNM as a model for porous media that was isotropic and computationally tractable. The PNMs used by Fatt (1965) modeled the void space of porous media using two-dimensional networks of tubes arranged in regular hexagonal and square lattices (shown in Figure 3). The tubes were designed to define individual pores, with radii randomly assigned from a pore-size distribution representative of a real porous media. The network structure of PNMs allowed for cross-directional flow to be modeled, which was a significantly more realistic representation of porous media compared to the bundle-of-tubes model. These simple PNMs were used by Fatt (1965) to study the flow of two immiscible fluids and derive capillary pressure curves as well as permeability estimates. The effects of pore-size distribution and number of connections per pore, also known as coordination number (Mehmani and Balhoff, 2015a), were also investigated. Capillary pressure curves were found to be more sensitive to changes in pore-size distribution than coordination number.

Following Fatt (1956), several studies, using modifications and improvements of the originally proposed PNM, were undertaken to investigate fluid flow in porous media. Most of these early PNMs, including those of Fatt (1956), belonged to a category known as statistically mapped PNMs. Statistically mapped PNMs randomly distribute network properties, such as pore throat radii or coordination number, from a probability distribution representative of a given porous media (Mehmani and Balhoff, 2015a). Statistical distributions, such as the beta distribution (useful for its fixed upper and lower bounds), can be used as the probability distributions of network properties (Reeves and Celia, 1996).

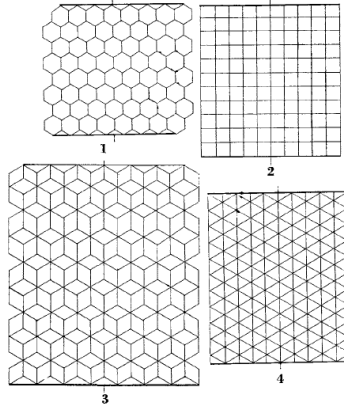


Figure 3. Lattice networks used by Fatt (1956): 1) single hexagonal 2) square 3) double hexagonal 4) triple hexagonal.

Dodd and Kiel (1959) noted that the immiscible displacement processes used by Fatt (1956) did not allow for the wetting phase to be trapped in the desaturation process. Their work extended that of Fatt (1956) by including parameters capable of modeling wetting phase trapping during desaturation. Wettability was also incorporated in displacement calculations by treating the probability of entrance of a displacing fluid into a wetting-fluid filled pore as a stochastic process. Furthermore, the number of pores in the PNMs used by Fatt (1956) ranged from 200 to 400, while the number of pores used by Dodd and Kiel (1959) ranged from 310 to 480. The modified PNM developed by Dodd and Kiel (1959) was accurate enough to simulate capillary pressure curves of sandstones.

Harris (1965) used a two-dimensional regular square PNM to simulate two-phase drainage in a column. A gravitational field was implemented by applying a pressure gradient to the PNM before simulating the drainage process. During drainage, the wetting phase exited at the bottom edge of the PNM, while the displacing non-wetting phase entered the top edge of the PNM. Shopper (1966) derived formulas for the relationships between electrical resistivity, porosity, and permeability using a PNM approach. The formulas contain a characteristic constant,  $\varepsilon$ , that is dependent on the structure and size of a given mesh. Shopper (1966) determined the limits of  $\varepsilon$  to be 0 and 1, but did not provide a means for explicitly determining the value of  $\varepsilon$ . Rink and Schopper (1968) continued the work of Shopper (1966) and developed a numerical method to calculate  $\varepsilon$ , which they demonstrated for triangular, square, and hexagonal two-dimensional networks.

Nicholson and Petropoulos (1971, 1975) studied gas phase flow using three-dimensional cubic lattice PNMs. In their work, they looked at the impact of tube radius distribution and coordination number on gas phase diffusion. Payatakes et al. (1980) used a square two-dimensional PNM to study the dynamics of discontinuous oil droplets during immiscible displacement in water wet unconsolidated sandpacks. Instead of using cylindrical tubes, their PNM used sinusoidal-contoured constricted tubes to more accurately model pore geometry. Mohanty et al. (1987) used a square two-dimensional PNM to model the displacement of a non-wetting oil phase from an initially oil-saturated porous media by a wetting phase. Their PNM was used to identify the locations and sizes of trapped oil blobs during the displacement process, and thus provide insight into the dependence of residual oil saturation on pore geometry and capillary number.

It is also possible to adjust the probability distributions, used to randomly assign network properties in statistically mapped PNMs, until a match with an experimental measurement, such as a capillary pressure curve, is achieved. The PNM can subsequently be used to predict more complex properties (Mehmani and Balhoff, 2015a). For example, Fischer and Celia (1999) adjusted the lattice topology of a cubic PNM to match experimentally obtained capillary pressure data, and then used the PNM to predict relative and absolute permeabilities for gas and water systems. The PNM was shown to predict water relative permeabilities that were effectively equivalent to available analytic models and outperformed analytic models for gas relative permeability predictions.

As demonstrated by the aforementioned studies, statistically mapped PNMs can serve as useful tools for making predictions of rock parameters. However, the random assignment of pore properties and regular lattice structures commonly used result in PNMs that may poorly represent porous materials (Bryant et al., 1993b). Additionally, the random assignment of network properties results in PNMs that are not unique, which compromises the predictive reliability of statistically mapped PNMs (Mehmani and Balhoff, 2015a). Bryant and coworkers (Bryant and Blunt, 1992; Bryant et al., 1993a, 1993b, 1993c) sought to overcome the limitations of statistically mapped PNMs by introducing the concept of physically representative PNMs. Unlike statistically mapped PNMs, physically representative PNMs are generated using details of the actual topology of a porous medium, without assumptions about its microstructure.

Bryant and Blunt (1992) used the coordinates of spherical ball bearings in a random close pack, as measured by Finney (1968), to generate a physically representative PNM. More specifically, a Delaunay construction, which connects nearest-neighbor points, was performed on the sphere centers. This resulted in tetrahedral Delaunay cells whose centers represented pores and faces represented throats, as depicted in Figure 4. Using the geometry of each tetrahedral cell, the assignment of pore and throat radii could be achieved without using statistical mapping. Each tetrahedral Delaunay cell had four faces, and thus the PNMs used had a constant coordination number of four. Bryant and coworkers (Bryant and Blunt, 1992; Bryant et al., 1993a, 1993b, 1993c) accurately calculated permeability, relative permeability, and capillary pressure for sand packs, bead packs, and a simple sandstone over a wide range of porosity. All calculations were made without using adjustable parameters or supplementary measurements of pore structure, such as capillary pressure or pore-size distribution. Additionally, because the Delaunay construction process resulted in a unique set of tetrahedral cells, the physically representative PNM could be replicated given the original sphere locations.

Modern imaging techniques have allowed for physically representative PNMs to be generated from voxel images of more complex porous materials, such as reservoir rock (Blunt et al., 2013). However, network extraction from digital images is a non-trivial process with several proposed approaches. Grain-based approaches, such as that used by Bryant and Blunt (1992), identify pores as areas farthest from grain centers (Øren and Bakke, 2002). Although grain-based approaches work well for sphere packings and other granular media, they are less effective for more complicated systems in which grain identification is difficult, such as carbonates (Blunt et al., 2013).

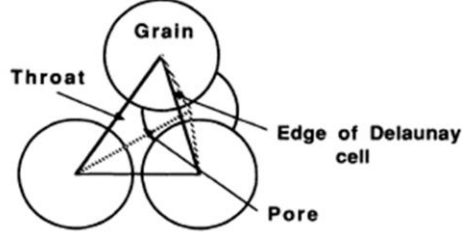


Figure 4. Delaunay cell in random close packing of spheres (Bryant and Blunt, 1992).

Void-based methods, such as the medial-axis method and maximal ball method, offer alternative approaches to grain-based network generation. In medial-axis methods, (e.g., Thovet et al., 1993; Lindquist and Venkatarangan, 1999) a skeleton of the void space is created by identifying points of maximum distance from the solid matrix. The skeleton is then used to define pores and throats. However, defining a unique set of pores and throats from the skeleton remains a limitation associated with the medial-axis method (Blunt et al., 2013). The maximal ball method (e.g., Silin and Patzek, 2006; Dong and Blunt, 2009) identifies pores and throats by analyzing the image for maximal inscribed void spheres. The largest spheres are modeled as pores, while smaller spheres represent throats. The ranges in size parameters used to differentiate pores and throats may however lead to discrepancies in PNMs generated using the maximal ball approach (Blunt et al., 2013).

Image-based physically representative PNMs have been used to model and characterize fluid flow in a variety of geologic materials. Thompson et al. (2008) used a grain-based algorithm to create a physically representative PNM from an image of a sandstone sample from the Frontier Formation in Wyoming, USA. The PNM was used to model single-phase creeping flow of a Newtonian fluid and calculate the permeability of the sample. Arns et al. (2005) generated a physically representative PNM from an X-ray microtomography image of a carbonate reservoir core plug. Using the PNM, permeability, capillary pressure, and electrical resistivity were calculated for the core plug, and were found to be in good agreement with experimentally measured values on the same sample. Image-based physically representative PNMs have also been used to compute two-phase relative permeability (e.g., Sheng et al., 2011).

Regardless of the approach used to generate a PNM, any simulation of flow in a PNM first requires the determination of bulk velocities within throats. The common approach (e.g., Mehmani et al., 2012) is to first apply a mass conservation at each pore in the PNM

$$\sum_j q_{ij} = 0 \quad (8)$$

where  $q_{ij}$  represents the volumetric flow rate in a throat connecting pores  $i$  and  $j$ . For an incompressible Newtonian fluid flowing at a low Reynolds number at steady state, the flow equations are given by

$$\sum_j q_{ij} = \sum_j \frac{g_{ij}}{\mu} (p_j - p_i) \quad (9)$$

where  $g_{ij}$  represents hydraulic conductance in the throat connecting pores  $i$  and  $j$ ,  $\mu$  represents fluid viscosity, and  $p_i$  represents pore pressure. Equations 8 and 9 create a system of linear equations that can be solved by imposing either constant pressure or constant flow rate boundary conditions. In the case of a constant flow rate boundary condition, the following constraining equation may be added to the matrix

$$Q = \sum_j [(p_{inlet} - p_i)g_{i,j}] \quad (10)$$

where  $Q$  is the constant rate boundary condition (represented by the sum of flow over all inlet pores) and  $p_i$  represents the pressure in each pore. Solving this system of equations yields the pressure in each pore, which can be used to calculate the bulk flow rate throughout the PNM.

Both statistically mapped and physically representative PNMs have been used to study solute transport in porous media, as well as the transport and retention of larger particles, such as colloids. In general, PNMs for solute or particle transport typically use either a Eulerian or Lagrangian approach (Mehmani and Balhoff, 2015a). Eulerian approaches treat pores as control volumes over which a particle balance is imposed (Mehmani and Balhoff, 2015b), while Lagrangian approaches track the pore to pore movement of individual particles (Mehmani and Balhoff, 2015a). Eulerian approaches are advantageous because they are known to be computationally efficient (Mehmani and Balhoff, 2015b). The mixed-cell method (MCM) (Bryntesson, 2002) is a commonly used Eulerian approach for solute transport (Mehmani et al., 2014). In MCM, bulk flow rates are first calculated in all throats of the PNM. Subsequently, solute balance equations are written for each pore and solved to calculate solute concentration. Solute in all pores is implicitly assumed to be perfectly mixed as each pore takes a single value for solute concentration. MCM has been used to study a wide range of solute transport systems, including solute precipitation and dissolution relevant to CO<sub>2</sub> sequestration (Li et al., 2006; Kim et al., 2011), and non-linearly adsorbing solute transport (Acharya et al., 2005).

The perfect mixing assumption used by MCM, while valid for low velocity diffusion dominant systems, leads to significant errors for higher velocity systems that may contain solute concentration gradients within individual pores (Mehmani and Balhoff, 2015a). This deficiency has led to several modified versions of MCM capable of modeling partial mixing of solute inside of pores. One such modified version, the streamline splitting method (SSM) (Mehmani et al., 2014), divides pore volumes into smaller sub-volumes that may each take differing solute concentration values. The number of sub-volumes in any given pore is equivalent to the number of inlet throats to that pore. Solute concentration values are calculated by applying conservation equations to all sub-volumes. Additionally, mass transfer via diffusion can occur between sub-volumes within a pore. Although computational costs were slightly higher for SSM compared to MCM, solute concentration predictions from SSM were shown to agree well with both CFD simulations and micromodel experiments (Mehmani and Balhoff, 2015a).

Lagrangian approaches, although typically more computationally demanding than Eulerian approaches, provide a more detailed description of particle transport (Mehmani and Balhoff, 2015a). The most commonly used Lagrangian approach is particle tracking, in which particle movement is individually tracked in the PNM in a series of advective and diffusive steps (Mehmani

and Balhoff, 2015a). Throats may have individually assigned velocity profiles that can be used to track particle movement within throats with enhanced detail (e.g., Bruderer and Bernabé, 2001; Bijeljic et al., 2004). Particle tracking PNMs utilizing detailed tracking within pores and throats have successfully predicted dispersion coefficients in unconsolidated porous media (Mehmani and Balhoff, 2015a). A less detailed, and less computationally expensive approach has also been implemented that does not track particle movement within pores. These methods rely on throat transit-time distributions to probabilistically determine particle duration in each throat (e.g., Rhodes and Blunt, 2006). The lack of flexibility associated with these transit-time distributions and limited information on particle location within a pore or throat however, may lead to model inaccuracy (Mehmani and Balhoff, 2015a).

PNMs have also been used extensively to model the transport and retention of micron-sized particles in porous media. Donaldson et al. (1977) used a network of parallel capillary tubes model to simulate the transport and retention of sand particles in sandstone cores. Experiments were first performed to identify permeability loss due to particle retention, effluent particle distributions, and pore-size distribution of the cores. The pore-size distributions and a random number generator were used to assign diameters to the capillary tube model. Influent particle sizes were randomly chosen from the same particle-size distribution used in the experiments. The probability of a particle entering a given capillary was proportional to the volumetric flow rate into the capillary tube. Each tube was divided into segments along its length with the segments connected in series. Once inside a tube, a particle could be retained in any segment along the tube. If retained, the tube diameter in that segment would be reduced by an amount proportional to the particle size, and the flow field for the entire system would be recalculated. Even with their simplistic model, calculated pressures and distributions of effluent particles from the capillary tube model were found to be in good agreement with the experimental data.

Todd et al. (1984) used a three-dimensional cubic PNM to investigate the effect of particle retention on permeability reduction. An experimentally obtained capillary pressure curve was used to assign throat-sizes to the PNM. The statistically mapped PNM was then scaled such that model porosity matched that of the rock sample used to supply the capillary pressure curve. A random walk technique was used to simulate the movement of particles through the PNM. In the technique, particle path selection was unbiased (particles were equally likely to travel in any direction), and thus the model simulated a purely diffusive process. Particle retention was modeled using several criteria and resulted in a reduction of pore throat diameter proportional to the size of the particle retained. The retention criteria included random capture (determined by a simple statistical function), size exclusion (where particles are retained due to being too large to enter a pore throat), and gravity settling. Model predictions of permeability reduction were observed to overpredict experimental values. Although attributed by the authors to deficiencies in the particle retention mechanisms used, the inaccuracies may also have been caused by the purely diffusive nature of the model (Sahimi et al., 1990). The transport of micron-sized particles is significantly impacted by fluid flow, and thus a purely diffusive model may not accurately represent actual systems (Molnar et al., 2015).

Rege and Fogler (1987) utilized a flow-biased probability model for particle transport as an improvement to the unbiased particle path selection used by Todd et al. (1984). In a flow-biased probability model for particle transport, the probability of a particle flowing into a given throat is

assumed to be stochastic, but proportional to the fluid flow rate in that throat. Thus, particles are more likely to enter throats with higher flow rates. Rege and Fogler (1987) used a triangular two-dimensional statistically mapped PNM to model formation damage caused by particle retention. Size exclusion was the only retention mechanism considered. Various influent particle size distributions, including uniform size distributions, were analyzed in the study. Uniform particle size distributions were observed to cause significant and rapid permeability reduction in the PNM. This permeability reduction eventually plateaued as all pore throats of diameter less than the influent particles became plugged. The results from the PNM were found to agree well with experimental data.

Rege and Fogler (1988) improved their previous PNM by considering direct interception, in addition to size exclusion, as a retention mechanism. Direct interception occurs when particles are retained on pore or throat surfaces because of forces, such as gravitational and hydrodynamic forces, acting on the particle. A probability-based approach was used to determine if particle retention due to direct interception would occur. The formula used to predict the probability of direct interception was a function of particle and throat radii, and a grouped parameter  $\theta$  that accounted for various fluid and particle properties, such as fluid velocity, pH, and particle density. The PNM was used to model permeability response and effluent concentration profiles. Model results were found to reasonably match the experimental data of Baghdikian et al. (1987) and Soo and Radke (1984, 1985). However, the predictive usefulness of the PNM used by Rege and Fogler (1988) was undermined because the derivation of the parameter  $\theta$  required fitting simulated data to experimental data (Feng et al., 2015).

In a manner similar to that of Rege and Fogler (1988), Wenrong et al. (1996) used a statistically mapped PNM that considered size exclusion and direct interception as retention mechanisms. Their model was used to investigate temporary plugging techniques (TPT), in which acid-soluble particles could enter a formation and form a low permeability mudcake. The removable mudcake prevents small particles from penetrating deep into the formation during activities, such as drilling, and thus prevents damage to the formation. Model results were compared with experimental core flooding data and found to be in good agreement. The use of a PNM was thus determined to be beneficial for optimizing the particle sizes used in TPT applications. Like Rege and Fogler (1988) however, the model's use of an aggregated parameter  $\theta$  in predicting direct interception weakened its practical usefulness.

Sharma (1985) and Sharma and Yortsos (1987a, 1987b) created a PNM that used an effective medium approach (EMA) to represent the flow field and calculate changes in the flow field caused by retained particles. In the EMA, effective properties for a porous media were obtained by representing a disordered media as a homogenous media with unknown physical constants (Sahimi et al., 1990). The model accounted for size exclusion and direct interception as retention mechanisms. The rate of particle retention by direct interception was determined using population balance equations that accounted for parameters such as particle size, throat size, and electrostatic potential of solid surfaces. In the model, retained particles could detach from matrix surfaces and re-enter the flow field. The model was capable of successfully predicting effluent concentration profiles, permeability reduction profiles, and filter coefficients used in continuum-scale models. Filter coefficients of porous media were found to change temporally and spatially, depending on the local degree of particle retention.



Imdakm and Sahimi (1987, 1991) developed a Monte Carlo method to study the transport of fine particles in porous media, and their effect on permeability when retained. The model consisted of a statistically mapped cubic PNM that rigorously tracked particle trajectories using a force balance approach, as proposed by Payatakes et al. (1973). The force balance involved in the trajectory analysis incorporated hydrodynamic and London forces, as well as the effect of the carrying fluid's ionic strength. Particle path selection was performed using a flow rate biased methodology like that of Donaldson et al. (1977) and Rege and Fogler (1987, 1988). Additionally, surface roughness was incorporated into the model using uniformly distributed rectangular surface protrusions. Particle retention was determined by applying a torque balance between a particle and a protrusion. Retained particles, unable to roll over the protrusion, could detach from the solid phase and return to the fluid phase provided hydrodynamic forces became sufficient. Size exclusion as a retention mechanism was also considered. Results for a given set of parameters were typically averaged from simulations conducted on ten different network realizations, each obtained by re-mapping the PNM from the same pore-size distribution. Results of permeability reduction showed good agreement with experimental results of Baghdikian et al. (1984). The ability to match experimental data without using any adjustable parameters was a considerable strength of the model developed by Imdakm and Sahimi (1987, 1991).

Siqueira et al. (2003) developed a three-dimensional statistically mapped PNM constructed using data obtained from digitized two-dimensional images of rock thin sections. The images were analyzed to determine pore and pore throat size distributions, porosity, and average coordination numbers. Incorporating these morphologic and topologic data into their PNM allowed for the calculation of realistic pore-scale interstitial velocities. Initially, the three-dimensional PNM consisted of a regular cubic lattice of cubic throats connected by throats with rectangular cross sections. Throats were then removed from the lattice until the average coordination number of the PNM matched the value obtained from image analysis. Like Rege and Fogler (1988), their model used an adjustable aggregated parameter to predict the probability of particle retention by direct interception. The parameter required a core flooding experiment for calibration, which detracted from the predictive utility of the PNM.

Yang and Balhoff (2017) developed a physically representative three-dimensional PNM that considered direct interception, particle bridging, and size exclusion as retention mechanisms, and utilized a trajectory analysis methodology to track particle movement. The force balance used in the particle tracking included the effects of Brownian motion, hydraulic drag, gravity, and electrostatic and van der Waals forces. Pore throats were given a converging-diverging geometry, and surface roughness was modeled using rectangular protrusions in a manner similar to that of Imdakm and Sahimi (1991). An analytical solution for fluid velocity was calculated within each throat, which enabled particle trajectories to be explicitly calculated. Rather than being statistically mapped onto regular lattices, irregular PNMs were mapped from computer-generated images, such as a sphere pack. Although computer-generated images were used, in principle the networks could have been constructed from three-dimensional images of rock samples. Model validation was provided by predictions of effluent particle concentrations, which compared well with experimental data obtained by Yoon et al. (2006). The model was then used to investigate how particle retention was affected by various parameters, such as Brownian diffusion, particle to grain size ratio, particle size distribution, and electrostatic forces.

## 1.6. Coupled Modeling

As discussed in the previous section, significant advancements in pore-scale modeling have enabled accurate predictions of continuum-scale parameters such as permeability, relative permeability, and filtration coefficient. These parameters are typically used as inputs to continuum-scale models, which lack the pore-scale resolution needed for direct determination. In theory, the most straightforward way to accurately incorporate pore-scale processes at the continuum-scale would be to define the entire continuum-scale domain with a single pore-scale model. This approach is however prohibited by current computational limitations, which are unlikely to be overcome in the near future (Tartakovsky et al., 2007). Even if a pore-scale model could incorporate every pore contained in a continuum-scale system, an upscaling scheme that coupled pore- and continuum-scale models would be more efficient and achieve acceptable accuracy. Significant efforts have been dedicated to developing approaches capable of coupling pore- and continuum-scale models. These approaches can be divided into two general categories: boundary coupling and hierarchical coupling. Hierarchical coupling methods can be further classified into sequential and concurrent coupling methods.

### 1.6.1. Boundary Coupling

Boundary coupling methods couple flow at an interface between two adjacent models (Sheng and Thompson, 2013). Balhoff et al. (2007) used a boundary coupling method that matched the fluid flux at an interface between a pore network model (PNM) (which represented a sphere packing) and a low permeability continuum region. The model was chosen primarily because it served as a prototype for an oilfield propped fracture application and could be modeled without changing the characteristic length scale (Balhoff et al., 2007). The PNM used was created from a computer-generated random sphere packing using a modified Delaunay tessellation algorithm, as demonstrated by Al-Raoush et al. (2003). Pore-scale heterogeneity was shown to impact the flow rate of the system, as well as the flow resistance caused by the low permeability continuum region. Thus, the accurate modeling of certain systems was shown to rely on the use of an effective coupling methodology.

A more general approach to boundary coupling utilizing mortars was presented by Balhoff et al. (2008). Mortars are two-dimensional finite-element spaces that couple independent subdomains by enforcing pressure and flux continuity at shared boundary interfaces (Balhoff et al., 2008). The use of mortars allows for the coupling of subdomains that can have non-matching dimensions. It also allows for the coupling of subdomains that are based on different physical principles or implement different finite-difference or finite element meshes (Sun et al., 2012). Balhoff et al. (2008) verified their model by coupling two identical periodic PNMs and comparing the resultant pressure field to a single equivalent PNM. The utility of this model was then demonstrated by coupling a variety of different pore-scale systems, and by coupling a pore-scale model to a continuum-scale model. The ability of mortar coupling to couple subdomains with different properties makes it applicable to a wide range of systems.

Sun et al. (2012) used mortar coupling to create a reservoir simulator that directly substituted PNMs for fine continuum-scale finite-difference grids. Over 7500 PNMs were inserted in an approximately one square meter area around a production well. The outer region consisted of a

finite-difference continuum-scale model. Mortar coupling was used to couple the PNM to each other as well as to couple the PNM to the outer continuum-scale model. Single-phase steady-state flow was modeled, although in principle the model could be used to investigate nonlinear and dynamic near-well phenomena, such as non-Darcy flow, acid transport, or formation damage (Sun et al., 2012). Although boundary coupling methods allow for dissimilar systems to be modeled together, they do not upscale information from the pore-scale to the continuum-scale.

### 1.6.2. Sequential Coupling

Sequential coupling can be classified as a hierarchical coupling technique. Unlike boundary coupled models, in which two models occupy distinct volumes and share an interface, hierarchically coupled pore- and continuum-scale models exist in the same volumetric space (e.g., a PNM inside a continuum-scale finite-difference grid (Sheng and Thompson, 2013)). In sequential coupling, pore-scale models are used to obtain continuum-scale parameters, such as permeability or relative permeability, and these parameters are then used as inputs to continuum-scale models (Sheng and Thompson, 2013). The objective of sequential coupling is to validate or replace the more costly and time-consuming results obtained from traditional laboratory experiments (Dakshinamurthy et al., 2014).

Blunt et al. (2002) sequentially coupled a PNM to a conventional finite-difference reservoir simulator. After presenting a conceptual framework for modeling two- and three-phase flow in PNM, this framework was used to accurately predict relative permeability for a water-wet sandstone. The relative permeability data obtained from the PNM was then utilized as an input to a simple waterflooding simulation in a large-scale reservoir model. Macroscopic predictions of oil recovery were found to significantly differ when compared to results obtained from conventional empirical relative permeability models. The significant difference observed in model predictions demonstrated the potential benefits of using input data obtained from sequentially coupled PNM, rather than empirical correlations, in continuum-scale modeling.

Rhodes et al. (2008) used sequential coupling to study solute transport in single-phase flow systems at the continuum-scale. Solute transport was first simulated at the pore-scale using a PNM developed by Rhodes and Blunt (2006) that incorporated a continuous time random walk particle tracking method. The pore-scale solute transport simulation yielded a distribution of transition times between pores that was derived using a truncated power law function. The transition time distribution was then used as an input to simulate solute transport at the core-scale, which yielded a new transition time distribution. The procedure was repeated to simulate solute transport at the grid-block-scale and finally the field-scale. Model validation was performed by predicting breakthrough curves in various sand packs and comparing them to experimental data. The study concluded that macroscopic behavior is impacted by pore-scale transport, even if the macroscopic system contains a high degree of heterogeneity. Thus, the assumption that particle transport is dominated by continuum-scale geology (thereby neglecting pore-scale dynamics) can lead to significant errors (Rhodes et al., 2008).

Hierarchical coupling is not limited to the use of network modeling to simulate pore-scale phenomena, or finite-difference methods to the modeling of continuum-scale behavior. In principle, any pore-scale model may be coupled to any continuum-scale model. Chen et al. (2010)

sequentially coupled a pore-scale Lattice Boltzmann Method (LBM) simulator to a continuum-scale LBM simulator. The study investigated how the deposition of micron-scale colloidal particles effects continuum-scale structural heterogeneity in sediment beds. Pore-scale LBM flow simulations were conducted to define a constitutive relationship between porosity and permeability for the glass bead system under investigation. This relationship was then utilized by a continuum-scale LBM model to predict the effect of particle deposition on bed structure.

### 1.6.3. Concurrent Coupling

Concurrently coupled models allow information to pass from both pore- to continuum-scale and continuum- to pore-scale models (Sheng and Thompson, 2013). This two-way exchange of information can occur periodically during a simulation and thereby provide a means of dynamically incorporating pore-scale phenomena into a continuum-scale model, while at the same time passing continuum-scale information to the pore-scale via updated boundary conditions. Thus, concurrent coupling has the potential to model a wide variety of systems in which pore-scale processes evolve temporally and effect continuum-scale behavior. Few published studies have successfully developed and implemented a concurrently coupled model. Celia et al. (1993) proposed a concurrently coupled model consisting of PNMs embedded in the centers of selected grid blocks of a continuum-scale model. The model was proposed as a method to incorporate material heterogeneities in multiphase flow simulations but was not developed due to computational limitations. Computational limitations also prevented the development of the concurrently coupled model of Van den Akker (2010), which proposed the use of LBM models to simulate turbulent two-phase flow processes.

Heiba et al. (1986) concurrently coupled a statistically mapped PNM to a one-dimensional continuum-scale finite-element simulator. The PNM simulated multi-phase flow and was used to obtain relative-permeability and capillary pressure data. This data was then used by the continuum-scale model to simulate multi-phase displacement. Local continuum-scale changes in water saturation were periodically passed to the PNM to update the continuum-scale data. The model was used to analyze continuum-scale displacements under varying conditions of wettability and flooding sequences. The model demonstrated the potential for concurrently coupled models to improve simulation accuracy compared to conventional models, which derive continuum-scale input parameters from empirical correlations. The concurrently coupled model however, had computational costs that were up to 100 times that of conventional models. More recently, Battiatto et al. (2011) developed a concurrently coupled model that used pore-scale models to overcome situations in which continuum-scale transport assumptions were violated. Concurrently coupled models have also been used to investigate non-Darcy flow at the continuum-scale (Chu et al., 2012), and to model immiscible displacement at the continuum-scale (Chu et al., 2013).

Sheng and Thompson (2013) concurrently coupled PNMs with a traditional continuum-scale simulator to investigate multiphase flow. The PNMs were located at the centers of selected continuum-scale grid blocks and provided relative permeability information to the continuum-scale grid blocks. The continuum-scale blocks then provided saturation and boundary pressure information to the PNMs. This two-way exchange of information was iterated so that the continuum-scale grid blocks could receive periodically updated relative permeability information. The model was tested by simulating variable-rate immiscible displacements under conditions in

which relative permeability depended on flow rate. Traditional continuum-scale models would not have been able to model such a rate-dependent scenario. Thus, the model of Sheng and Thompson (2013) demonstrated the ability of concurrently coupled models to effectively incorporate dynamic pore-scale phenomena in a continuum-scale model. Despite its success, their model used a steady-state value from the pore-scale simulation to communicate back to a transient continuum-scale model, which allowed for a discrepancy in saturation between the two models over time. Additionally, unlike this work, the impact of the size of the embedded pore-scale model relative to the continuum-scale grid block was not studied.

French (2015) created a concurrently coupled PNM and continuum-scale reservoir simulator that effectively captured changes in permeability caused by particle retention. However, the model was not capable of simulating truly continuum-scale systems. The system tested was one-dimensional and consisted of five continuum-scale grid blocks each embedded with a single PNM of the same size as the grid block. Thus, although the continuum-scale was modeled using continuum-scale transport equations, the continuum-scale grid blocks had pore-scale dimensions. Considering that most practical continuum-scale applications involve upwards of hundreds of continuum-scale grid blocks simulated in three dimensions, significant challenges remained in configuring the model for practical applications.

### 1.7. Objectives

The primary objective of this work was to develop a concurrently coupled model that can be used to accurately predict the effects of particle transport and retention on continuum-scale filtration behavior. Physically representative pore-network models (PNMs) were embedded at the centers of traditional finite-difference continuum-scale grid blocks. Using boundary conditions derived from the continuum-scale grid blocks, the PNMs obtained continuum-scale parameters. The continuum-scale parameters were then assigned to the continuum-scale grid blocks, which represented homogenous volumes. By iterating the process periodically, the model could dynamically capture pore-scale effects on continuum-scale processes.

As an advancement upon previous works involving concurrently coupled models, this work performed accurate simulations in which greater than an order-of-magnitude size difference existed between embedded pore-scale models and finite difference grid blocks. By gradually increasing the size discrepancy between embedded pore-scale models and finite difference grid blocks, challenges associated with overcoming the spatial and temporal discrepancies of these scales were identified and quantified. The model was also extended to three dimensions to simulate a realistic field-scale scenario of water injection with particles being retained. The final three-dimensional simulations involved hundreds of continuum-scale grid blocks, each with embedded PNMs. Furthermore, the model was shown to capture dynamic pore-scale effects at the continuum-scale in a flexible framework. The work demonstrates the significant potential for concurrently coupled models not only for continuum-scale systems involving particle transport and retention, but for many systems involving dynamic pore-scale effects.

## Chapter 2. Technical Approach

### 2.1. Resources Available

#### 2.1.1. Pore Network Models

The pore network models (PNMs) used in this work were generated using internally developed algorithms. The first algorithm, Vox2Net, uses a maximal ball approach to create physically representative PNMs from segmented three-dimensional voxel images (Bhattad et al., 2011). The segmented images can be of actual rock samples or computer-generated geometric packings. Maximal ball approaches identify pores and throats by analyzing the image for maximal inscribed void spheres. The largest spheres are modeled as pores, while throats are identified as spheres below a cutoff threshold size value. The PNMs created by Vox2Net characterize porous media using a body and throat framework. In this framework, throats are defined as two-dimensional surfaces connecting two pores, and thus occupy no volume. Optional input parameters to Vox2Net allow for pores to be merged based on their degree of overlap.

Two physically representative PNMs generated with the Vox2Net algorithm were used in this work. One, referred to hereafter as the Berea PNM, was generated from microtomographic images of a Berea sandstone core sample (Figure 5).

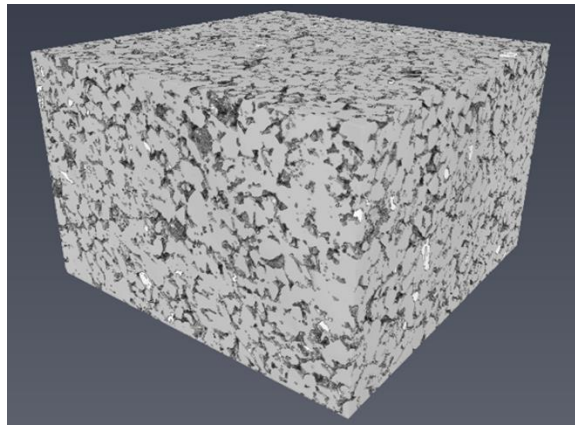


Figure 5. Microtomographic image of a Berea sandstone core sample.

The Berea PNM is depicted in Figure 6 as a simplified ball-and-stick model. This ball-and-stick depiction is for illustrative purposes only. As previously described, throats are represented as two-dimensional surfaces in the model and occupy no volume, unlike the stick representation of throats in Figure 6. The Berea PNM was the same as that used by French (2015), having dimensions of  $0.3502 \times 0.3502 \times 0.2270 \text{ cm}^3$  and containing 31,400 pores and 137,215 throats. Prior to all PNM simulations in this work, no-flow boundaries were implemented on boundaries orthogonal to the flow direction by removing all boundary throats not lying on the inlet or outlet face of the PNM. Pores with no throat connections, also known as dead pores, were also removed from all PNMs before simulating particle transport because these pores do not contribute to flow and can cause

singularities in the pore pressure solution matrix. Removal of boundary throats and dead pores for the Berea PNM resulted in the PNM containing 30,042 pores and 134,294 throats. Permeability and bulk porosity were found to be 521 mD and 15.24% respectively, which were in good agreement with experimentally determined values obtained from the sample on which the PNM was generated. When running particle filtration simulations on any of the PNMs, flow was selected in a principal direction. In the one-dimensional work of this study, that flow direction was selected to ensure particles flowed in one of the directions of the sample with the longest length. Table 1 summarizes the properties of the Berea sandstone PNM.

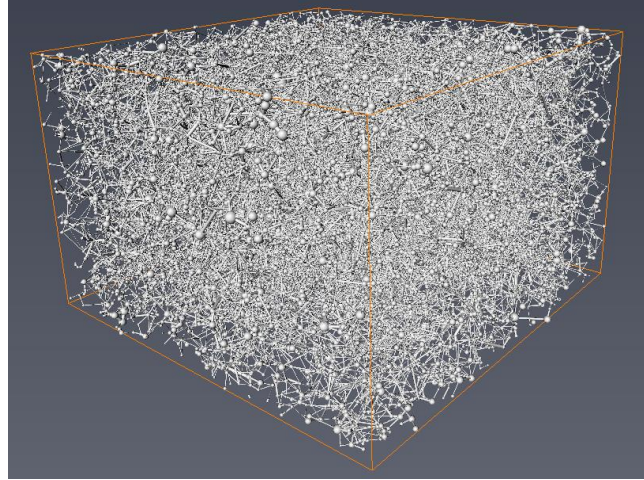


Figure 6. Berea sandstone PNM (ball-and-stick representation).

Table 1. Properties of Berea sandstone pore network model.

Dimensions (x,y,z):	(0.3502, 0.3502, 0.2270) cm <sup>3</sup>
Number of Pores:	30,042
Number of Throats:	134,294
Permeability:	521 mD
Porosity:	15.24%

The second physically representative PNM was created using a computer-generated random packing of 10,000 uniform-size spheres (Figure 7). This PNM will hereafter be referred to as the random uniform PNM or RU PNM. A sphere radius of  $2.1918 \times 10^{-4}$  m was chosen for the RU PNM. This radius was selected to enable comparisons with the work of Jha et al. (2011), who also analyzed a random packing of 10,000 spheres with radii of  $2.1918 \times 10^{-4}$  m. The calculated permeability and porosity of the RU PNM were 221.3 Darcy and 39.08% respectively. The calculated permeability for the RU PNM was within 5% of the value calculated using the modified Carman-Kozeny equation proposed by Ergun (1952) for packed beds of spheres

$$k = \frac{D_p^2 \phi^3}{150(1 - \phi)^2} \quad (11)$$



where  $D_p$  represents grain diameter and  $\emptyset$  represents porosity of the random uniform sphere packing. The number of pores and throats after removal of dead pores and boundary throats was 18,495 and 120,529 respectively.

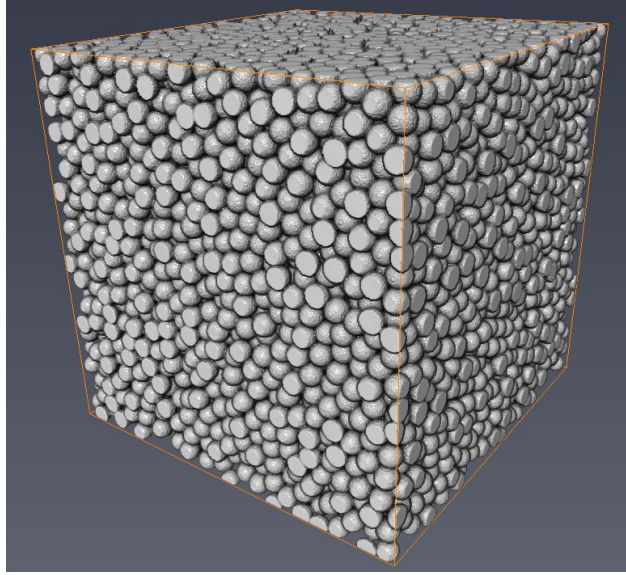


Figure 7. Random packing of 10,000 uniform-size spheres.

Table 2 summarizes the properties of the RU PNM. A ball-and-stick depiction of the RU PNM is provided in Figure 8.

Table 2. Properties of random uniform packing PNM.

Dimensions (x,y,z):	(0.8927, 0.8927, 0.8927) cm <sup>3</sup>
Number of Pores	18,495
Number of Throats	120,529
Permeability	221.3 Darcy
Porosity	39.12%

A separate program was written which enabled the generation of three-dimensional lattice PNMs. The lattice models used in this work had pores arranged in a regular cubic structure (pore centers equidistant and orthogonal to 6 neighbors). An example 10x10x10 lattice PNM is depicted in Figure 9.

Pore diameters in the lattice structures were randomly distributed between a minimum and maximum value, and all other geometric properties of the lattice were derived from these randomly selected pore diameters. Although structurally simple, lattice networks were found useful for investigating complex phenomena seen in physically representative PNMs. A 40x40x20 lattice



PNM similar in size and number of pores to the Berea PNM was created, which is hereafter referred to simply as the Lattice PNM. Table 3 summarizes the properties of the Lattice PNM.

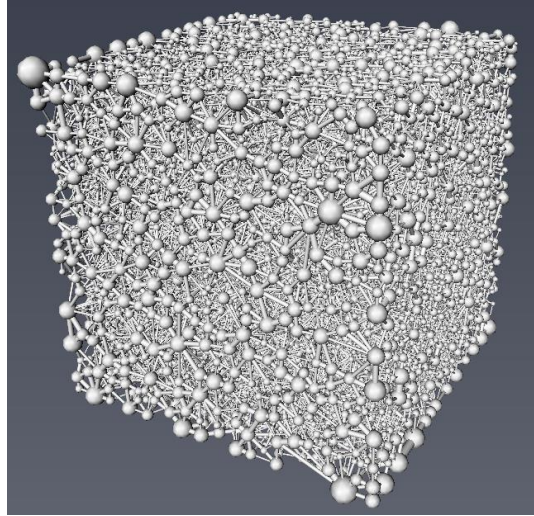


Figure 8. Random uniform sphere packing PNM (ball-and-stick representation).

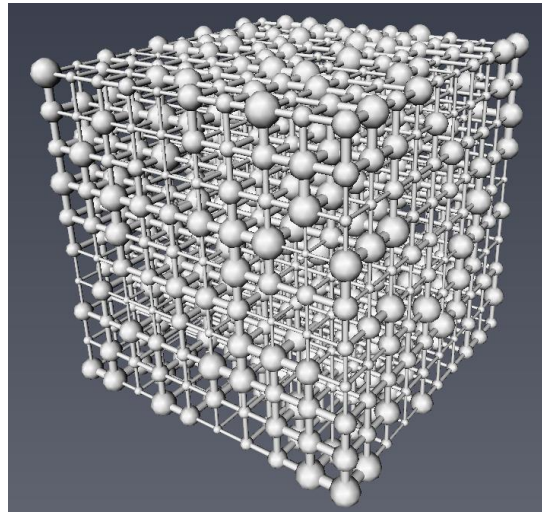


Figure 9. Lattice PNM (ball-and-stick representation).

Table 3. Properties of the Lattice PNM.

Dimensions (x,y,z):	(0.4, 0.4, 0.2) cm <sup>3</sup>
Number of Pores	32,000
Number of Throats	192,000
Permeability	19.57 md
Porosity	8.90%

### 2.1.2. Pore Network Particle Filtration Model

The algorithm used to simulate particle transport and retention in PNMs for this work was based on the algorithm developed by French (2015). The algorithm can be used to simulate single-phase fluid flow and particle transport in physically representative systems. Size exclusion, where particles are retained due to being too large to enter a pore throat (Sharma and Yortsos, 1987a), is the only retention mechanism considered by the model. Size exclusion is known to be a dominant retention mechanism for many systems containing micron-sized particles (Rege and Fogler, 1987). Considering size exclusion as the only retention mechanism was considered valid because micron-sized particles were the focus of this work. In principle, additional retention mechanisms and other complexities could be added to the PNM filtration mode to expand its capabilities. Using a relatively simple PNM was acceptable for this work as it reduced potential sources of error and was more computationally efficient. The PNM filtration model could also be replaced with a different type of pore-scale model, such a direct finite-element model for fluid flow and particle tracking.

Before a particle transport simulation began, the pressure in each pore of the PNM was calculated. As previously stated in section 1.5.2. (see Equations 8 and 9), mass conservation was first applied to each pore in the PNM. The fluid was assumed to be Newtonian and flowing at a low Reynolds number at steady state. This assumption allowed for the flow rate between two pores to be calculated as a function of the pressure difference between the two pores. Thus, a system of linear equations was created which could be solved by imposing either constant pressure or flow rate boundary conditions. Fluid flow could be prevented in any of the three principal directions by imposing no flow boundary conditions. The system of linear equations was represented as a sparse matrix and solved using the Gauss-Seidel method (French, 2015). Solving this system of equations yielded the pressure in each pore, which could be used to calculate the bulk flow rate throughout the PNM. The Gauss-Seidel method, although relatively simple and time consuming for solving a large system of equations, was found to be faster than more complex matrix solvers for cases with many particles trapping. This was due to the fact that a single particle trapping had a small impact on the pressure field of the PNM. Thus, although the first pressure solution was more time consuming to compute, subsequent pressure solutions were obtained more rapidly because the Gauss-Seidel method uses the previous solution as a starting point.

Permeability and porosity values of the model could be identified at any point in the particle filtration simulation. Permeability for a given flow direction was calculated using Darcy's law (Darcy, 1856)

$$k = \frac{Q\mu L}{A(P_i - P_o)} \quad (12)$$

where  $Q$  represents total inlet flowrate,  $\mu$  represents fluid viscosity,  $L$  represents the domain length in the direction of flow,  $A$  represents cross sectional area of the inlet face, and  $P_i$  and  $P_o$  represent inlet and outlet pressure respectively. Total inlet flowrate was calculated by identifying all pores residing on the inlet face of a given flow direction and summing the volumetric flow rates into those pores. Porosity was determined by dividing the sum of the void volume occupied by all pores by the bulk volume of the system. In practice, it was also important to identify pores which do not

contribute to flow in the PNM and remove the volume of these pores when calculating interstitial velocity.

With the velocity field, permeability, and porosity initialized, the simulation of particle transport and retention could begin. The number of injected particles, their size distribution, and time of injection were all inputs to the PNM simulations. Once injection began, particles entered the PNM in series. The PNM used in this study incorporated a flow-biased particle path selection methodology, analogous to that of Rege and Fogler (1987). In a flow-biased probability model for particle transport, the probability of a particle flowing into a given throat is assumed to be stochastic, but proportional to the fluid flow rate in that throat. Thus, particles were more likely to enter throats with higher flow rates. Initial particle location in the PNM was determined using a flow-biased probability calculation that considered the flow rates of all pores and throats on the injection face.

For any particle determined to have entered a throat with a radius smaller than that of the particle, the particle was deemed to be irreversibly retained. For any retained particle, key network properties were recalculated. The cross-sectional area of the throat in which the particle was retained was reduced by the cross-sectional area of the particle. Additionally, the void volume of the most recent pore in which the particle was traveling was reduced by the volume of the retained particle. This reduced the porosity of the system, which was recalculated accordingly. The volume reduction had to occur in a pore, as throats were characterized as two-dimensional surfaces and thus occupied no volume in the PNM. Furthermore, because particle retention altered network properties, the pressure field was recalculated each time a particle was retained. The location at which a particle was retained was also recorded so that a spatial distribution of retained particle penetration could be calculated.

The methodology used to adjust the hydraulic conductivity of a throat in which a particle has been retained can have a significant impact on subsequent particle retention behavior. As demonstrated by (Thibodeaux, 2018) the change in hydraulic conductance due to a trapping particle is a complex function of pore and throat geometries, particle size, and pore coordination numbers. Simple rules that reduce hydraulic conductance by a fixed percentage or as linear functions of throat and particle properties poorly predict true the reductions of hydraulic conductance. For this reason, a probabilistic approach was used to reduce hydraulic conductance in the simulations used in this work. In this approach, hydraulic conductivity of a throat containing a trapped particle,  $g_{ij}^{TP}$ , was evaluated as

$$g_{ij}^{TP} = \gamma_{ij} g_{ij} \quad (12)$$

where  $g_{ij}$  is the pre-particle trapping hydraulic conductance value and  $\gamma_{ij}$  is a conductivity reduction parameter. In this work, the conductivity reduction parameter was obtained using a cumulative density function derived from the histogram of Thibodeaux (2018) shown in Figure 10.

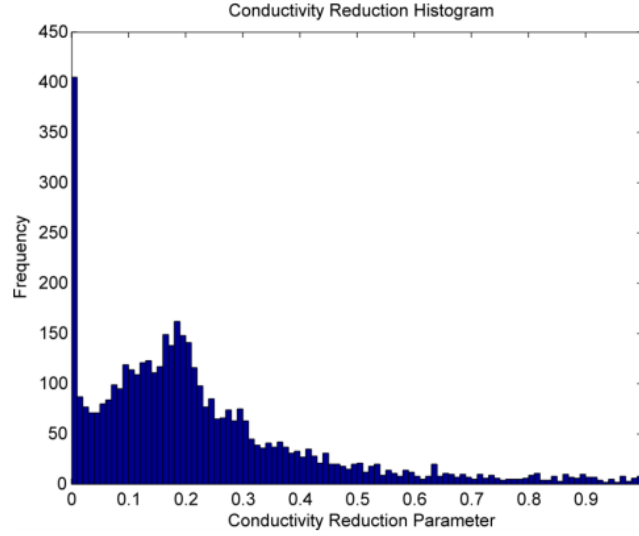


Figure 10. Histogram of conductivity reduction parameter for glass bead pack data (Thibodeaux, 2018).

Thibodeaux (2018) obtained the histogram in Figure 10 by running FEM simulations to evaluate hydraulic conductance values before and after spherical particles were trapped in a glass bead pack model. To generate the data approximately 500 throats were tested with 8 particle sizes across 16 subdomains of the glass bead pack model. Error was likely introduced in this work because the probabilistic model used to determine hydraulic conductivity reduction in Figure 10 originates from glass bead pack data while the PNM systems used in this work were primarily physically representative of Berea sandstone samples. This method was considered acceptable and was used because it is more physically realistic than using a single reduction coefficient or linear model. In principle a more rigorous methodology for determining  $g_{ij}^{TP}$  could be implemented. However, this was outside the scope of this research.

To extend the effective size of PNM domains, the particle filtration model was capable of running boundary coupled simulations. In these boundary coupled simulations, multiple copies of a single PNM were appended to each other. Particle transit times were recorded for all particles in a given PNM before continuing the simulation in the subsequent downstream PNM. Initial particle locations at each PNM inlet were determined from a random flowrate bias approach across all inlet pores. Thus a particle could “jump” instantaneously from one effluent location to the next influent location. French (2015) used the same approach for boundary coupled simulations and found that dispersion and retention coefficients were not significantly impacted by this boundary coupled method.

### 2.1.3. Determination of Retention and Dispersion Coefficients

A retention coefficient ( $k_r$ ) and dispersion coefficient tensor are required to solve species transport at the continuum-scale, as described by Equation 3. The retention coefficient quantifies the degree to which particles are retained in the porous media.

As demonstrated by McDowell-Boyer et al. (1986), the retention coefficient can be evaluated by analyzing the effluent concentration curve produced by a constant injection of particles and using the relationship

$$k_r = -\frac{u}{L} \ln \left( \frac{C_p}{C_0} \right) \quad (12)$$

where  $u$ ,  $L$ ,  $C_0$ , and  $C_p$  represent interstitial velocity, system length, influent particle concentration, and effluent concentration curve plateau concentration respectively. In this work, the ratio of  $C_p$  to  $C_0$  was determined by injecting particles into a single PNM system of interest and determining the fraction of particles that would have been retained by size exclusion. The number of particles injected was pre-determined from a sensitivity analysis to ensure that sufficient particles were used for the retention coefficient value to be accurate. When running the simulation, if a particle was considered to have been retained, it was counted as such, but the PNM was left unchanged. Throat conductivity was not reduced because retention coefficient is a strong function of system damage. If throat conductivity values were reduced, subsequent particles would be less likely to flow into them and thus less likely to be retained within the PNM. This could result in the calculation of artificially low values of the retention coefficient.

The dispersion coefficient tensor quantifies the degree to which particles spread spatially because of the variable flow velocities and flow paths present in a porous media. The longitudinal dispersion coefficient quantifies spreading in the direction of fluid flow, while the transverse dispersion coefficient quantifies spreading orthogonal to the flow direction. As demonstrated by Jha et al. (2011), longitudinal dispersion coefficients can be determined via spatial statistics using the relationship

$$D_L = \frac{\sigma^2}{2t} \quad (13)$$

Where  $\sigma^2$  is the variance of particle positions in the flow direction at time  $t$ . In this work, a sensitivity analysis for each PNM was used to determine the number of particles needed to be used to obtain accurate dispersion coefficient values. Jha et al. (2011) demonstrated that dispersion coefficients only reach a constant value when the system length is sufficiently large to ensure that particles have sampled a statistically significant number of flow velocities within a system. Thus, using a single PNM may not be sufficient to obtain accurate dispersion coefficient values. The number of PNMs needed to obtain a convergent dispersion coefficient depends on the size of the PNM as well as the distribution of velocities within the PNM. Complex PNMs with relatively wide velocity distributions, such as those representing real rocks, require larger systems than those with narrow velocity distributions. In this work, the number of boundary coupled PNMs needed to obtain an accurate dispersion coefficient was determined by running a series of simulations for each PNM and then analyzing at which system length convergence occurred. Results of these simulations are shown in Figure 11.

Due to its relatively narrow velocity distribution, the length of a single PNM is sufficient to achieve convergence of the dispersion coefficient for the Lattice PNM. For the random uniform (RU) sphere packing PNM, convergence was reached after approximately 4 PNMs. The Berea PNM, having the widest throat velocity distribution of the three PNMs, had the longest length required for dispersion coefficient convergence at about 10 PNMs. Although convergence did not occur

until 10 PNMs, the value at 5 PNMs was within 10 percent of the converged value, so 5 PNMs were used to determine longitudinal dispersion coefficients for all simulations involving the Berea PNM.

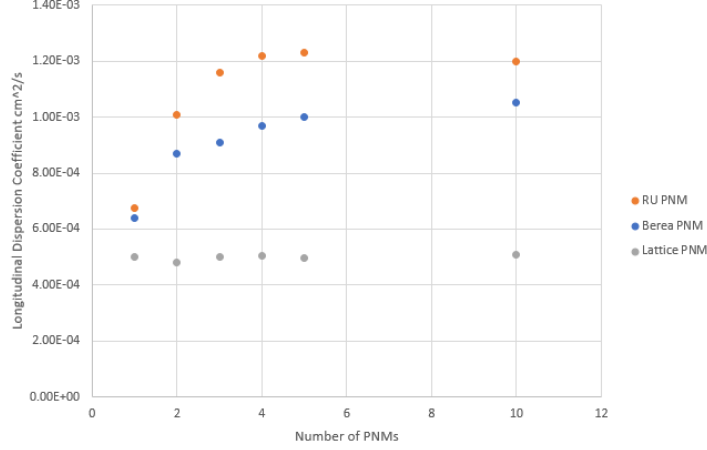


Figure 11. Longitudinal dispersion coefficient convergence.

An analysis was performed to identify the impact of number of particles simulated on dispersion and retention coefficients values. Simulations were run with increasing numbers of particles injected from 100 to 100,000. The results from Figure 11 were used to determine the number of boundary coupled networks required for each system. 1, 4, and 5 boundary coupled PNMs were used for each simulation for the Lattice PNM, RU PNM, and Berea PNM respectively. Figure 12 shows the results of these simulations for longitudinal dispersion coefficient.

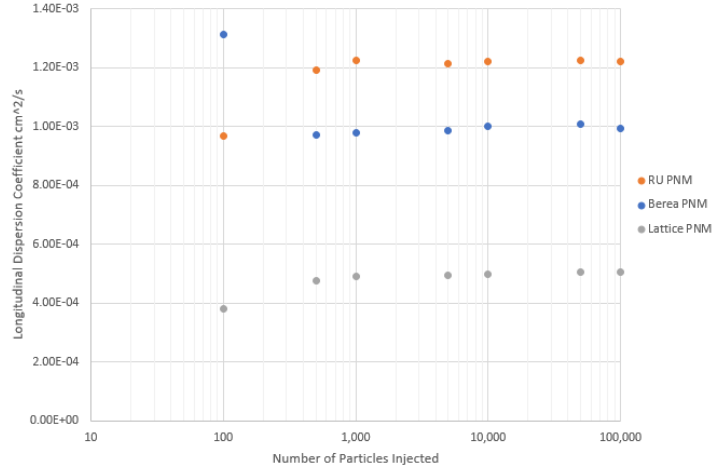


Figure 12. Longitudinal dispersion coefficient vs number of particles injected.

A relatively small number of particles can be simulated to obtain the converged dispersion coefficient values. The difference between longitudinal dispersion coefficient calculated using

1,000 particles and 100,000 particles was 1.4% for the Berea PNM, 2.8% for the RU PNM and 3.3% for the Lattice PNM.

Similar results were observed for retention coefficient. Simulations were performed on the Berea PNM for 13- and 10-micron-diameter particle sizes, which corresponded to average ratios of retained particles to injected particles of 0.96 and 0.39 respectively. Results of the simulations are shown in Figure 13.

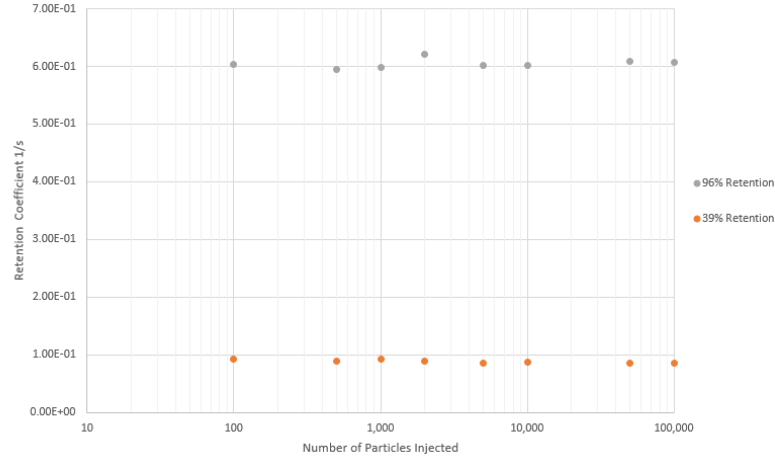


Figure 13. Retention coefficient vs number of particles injected.

The difference between retention coefficient calculated using 1,000 particles and 100,000 particles was 1.5% for the high retention scenario and 5.8% for the moderate retention case. Based on these results it was considered that use of 1,000 particles would be acceptable for simulations to calculate dispersion or retention coefficients. To ensure converged coefficient values, 2,000 particles were used for retention and dispersion coefficient determinations in this work.

A comparison with experimental and simulated data was performed to analyze the reliability of dispersion coefficient values calculated in this work. Numerous experimental studies have analyzed dispersion in random packings of uniform sized spheres. Jha et al. (2011) developed a PNM capable of calculating dispersion coefficients and compared their simulated results to multiple experimental works (Figure 14). Dispersion coefficients calculated by this study at a variety of inlet flow rates for the previously described RU PNM are superimposed in red. In Figure 14,  $D_L$  is the longitudinal dispersion coefficient,  $D_o$  is the molecular diffusion coefficient,  $v$  is the interstitial fluid velocity, and  $D_p$  is the diameter of the spheres which make up the sphere packing.

The plug flow model used by Jha et al. (2011) assumed that particles in a given throat flowed at a fixed velocity equal to the average velocity of that throat. The plug flow model did not consider diffusion and was therefore similar to the model used in this work. The dispersion coefficients produced by this work tended to be higher than experimental values and those simulated by Jha et al. (2011). This is likely due to the choice of flowrate biased path selection, which does not consider flow streamlines within pores. In a real system, the exit throat for a particle inside a pore will be influenced by the local flow field. This influence will increase with increasing flow rate

and a particle may have a very low probability of traveling into a throat that is not aligned with the local flow field, even if that outlet throat has a significant flow rate. The model used in this work assigns a probability of path selection purely based on exit flow rates in a given pore, which leads to artificial dispersion.

The models used by Jha et al. (2011) tracked particle locations within pores and throats and used deterministic rules based on particle position and local flow streamlines to determine a particle's exit throat. Additionally, that model was generated using Delaunay tessellation and had a fixed coordination number (number of throats per pore). Having a fixed coordination number made the number of possible flow scenarios tractable and thus enabled deterministic path selection criteria. It is thought that such deterministic path selection rules do not exist for physically representative PNM systems with complex structures. Thus, the artificial dispersion caused by flow rate biased path selection would be present for any complex physically representative PNM system, such as a reservoir rock. Despite the inherent tendency for overprediction of dispersion of the PNM used in this study, simulated dispersion coefficient values are reasonably and acceptably accurate given that the main objective of this work is to investigate concurrent coupling of PNMs and larger continuum-scale models.

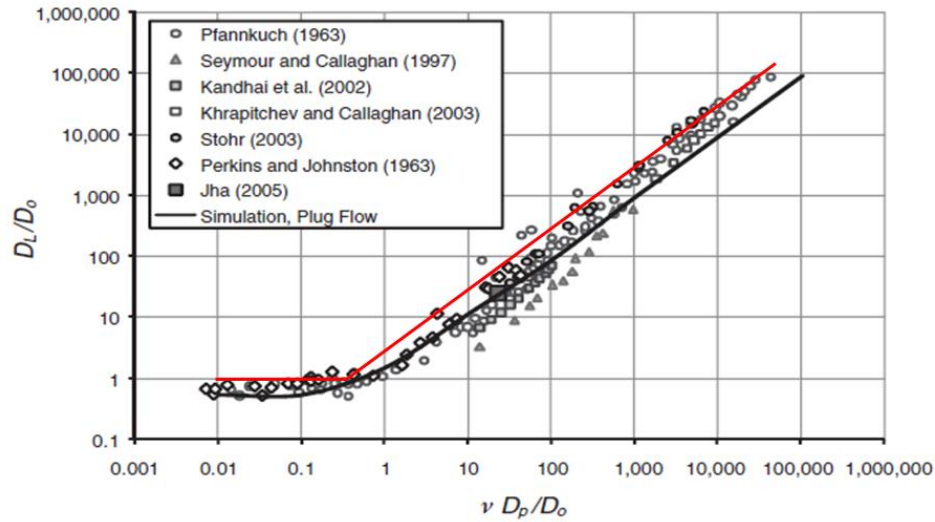


Figure 14. Dispersion coefficient comparison from Jha et al. (2011) (simulated values from this work in red).

The plug flow model of Jha et al. (2011) tended to underestimate values for dispersion coefficient. When the authors altered the model to include parabolic velocity profiles in throats as well as diffusion, the simulated dispersion coefficients increased and matched experimental data more closely. The authors concluded that adding diffusion and parabolic throat velocities widened the distribution of velocities in the model, which resulted in increased dispersion. Thus, incorporating parabolic flow profiles and diffusion into the particle transport and retention model used in this work would lead to even greater dispersion, and so was not implemented. Without diffusion however, it was possible for the model used in this study to produce unreasonably low dispersion coefficients at very low flow velocities. In theory, particle spreading due to dispersion cannot be



less than that due to diffusion and so in this work the diffusion coefficient was used as a lowest possible value for dispersion coefficient. The transverse dispersion coefficient was assumed to be equal to a value one order-of-magnitude less than longitudinal dispersion coefficient. This assumption is valid for relatively large particles at moderate to high flow rates, which are the scenarios of interest in this work (Herrera, 2009).

## 2.2. Finite Difference Model

### 2.2.1. Solving the Pressure Field

A finite-difference reservoir simulator was developed and verified to enable its concurrent coupling to the PNM filtration model described in section 2.1.2.. The finite-difference simulator modeled flow of single-phase incompressible fluids. A block-centered grid system was implemented in which fluid and rock properties such as porosity, phase pressure, and fluid density were defined at block centers (Chen, 2007).

Fluid flow equations were derived from the conservation of mass equation applied to a rectangular control volume (a single grid block)

$$\{Total\ mass\ in\} - \{Total\ mass\ out\} = \{Total\ mass\ accumulation\} \quad (14)$$

Mass in or out of a given face is equivalent to the product of density ( $\rho$ ), velocity ( $u$ ) at the grid face, and cross-sectional area ( $A$ ). Mass accumulation may occur because of fluid compressibility, mass sinks, or mass sources. Applying these parameters in three dimensions gives

$$\begin{aligned} & \left[ (\rho u_1)_{\Delta x_1 - \frac{\Delta x_1}{2}, \Delta x_2, \Delta x_3} - (\rho u_1)_{\Delta x_1 + \frac{\Delta x_1}{2}, \Delta x_2, \Delta x_3} \right] \Delta x_2 \Delta x_3 + \\ & \left[ (\rho u_2)_{\Delta x_1, \Delta x_2 - \frac{\Delta x_2}{2}, \Delta x_3} - (\rho u_2)_{\Delta x_1, \Delta x_2 + \frac{\Delta x_2}{2}, \Delta x_3} \right] \Delta x_1 \Delta x_3 + \\ & \left[ (\rho u_3)_{\Delta x_1, \Delta x_2, \Delta x_3 - \frac{\Delta x_3}{2}} - (\rho u_3)_{\Delta x_1, \Delta x_2, \Delta x_3 + \frac{\Delta x_3}{2}} \right] \Delta x_1 \Delta x_2 = \left( \frac{\partial(\phi \rho)}{\partial t} - q \right) \Delta x_1 \Delta x_2 \Delta x_3 \end{aligned} \quad (15)$$

Where subscripts (1, 2, 3) denote principal directions, subscripts on the  $(\rho u_i)$  terms denote grid faces,  $\Delta x_i$  represents grid length in a given direction,  $\phi$  represents porosity, and  $q$  is a sink/source term representing cumulative mass flow rate. To apply Equation 15 to a porous medium, velocity may be substituted with fluid velocities from Darcy's law (Darcy, 1856)

$$u_i = - \frac{kA}{\mu} \frac{\partial p}{\partial x_i} \quad (16)$$

where  $k$  is permeability,  $\mu$  is fluid viscosity, and  $p$  is pressure. Substitution of Equation 16 into Equation 15 yields

$$\frac{\partial(\phi \rho)}{\partial t} = \nabla \cdot \left( \frac{\rho}{\mu} \mathbf{k}(\nabla p - \gamma \nabla z) \right) + q \quad (17)$$

where  $\mathbf{k}$  is the absolute permeability tensor and  $\gamma$  is the product of density and gravitational acceleration. Discretizing Equation 17 using a backwards difference scheme for the temporal derivative and a central difference scheme for the spatial derivatives yields

$$\begin{aligned} \left( V \phi \rho^n c_t^n \frac{p^{n+1} - p^n}{\Delta t} \right)_{i,j,k} = & T_1(p_{i+1,j,k}^{n+1} - p_{i,j,k}^{n+1}) - T_2(p_{i,j,k}^{n+1} - p_{i,j-1,k}^{n+1}) + \\ & T_3(p_{i,j+1,k}^{n+1} - p_{i,j,k}^{n+1}) - T_4(p_{i,j,k}^{n+1} - p_{i,j-1,k}^{n+1}) + \\ & T_5(p_{i,j,k+1}^{n+1} - p_{i,j,k}^{n+1}) - T_6(p_{i,j,k}^{n+1} - p_{i,j,k-1}^{n+1}) - \\ & T_1 \gamma (z_{i+1,j,k} - z_{i,j,k}) + T_2 \gamma (z_{i,j,k} - z_{i,j-1,k}) - \\ & T_3 \gamma (z_{i,j+1,k} - z_{i,j,k}) + T_4 \gamma (z_{i,j,k} - z_{i,j-1,k}) - \\ & T_5 \gamma (z_{i,j,k+1} - z_{i,j,k}) + T_6 \gamma (z_{i,j,k} - z_{i,j,k-1}) - q_{i,j,k}^{n+1} \end{aligned} \quad (18)$$

where  $V$  represents grid volume,  $c_t$  represents total compressibility, superscripts denote time step, and  $T$  represents block transmissibility. Transmissibility values are defined at grid faces.  $T_1$  and  $T_2$  are defined at the  $i+1/2$  and  $i-1/2$  faces respectively.  $T_3$  through  $T_6$  were defined similarly but for the  $j$  and  $k$  directions. Transmissibility at the  $i+1/2$  face was defined as

$$T_1 = \frac{k_1 A_1 \rho}{\Delta x_1 \mu} \quad (19)$$

$T_2$  through  $T_6$  were defined similarly. Transmissibility values were evaluated at grid faces while reservoir properties were stored at grid centers. Thus, appropriate averaging was required for all transmissibility calculations. This work used the standard method of arithmetic averaging for fluid properties and harmonic averaging for rock properties (Chen, 2007).

Before modeling fluid flow, initialization of boundary conditions and well information was required. As a default setting, all boundaries were initialized as no flow boundaries, although alternative conditions could be specified. Boundary condition options included flow rates, pressures, and pressure gradients specified at external boundaries of the system. The Peaceman well model (1977) was used to relate grid block pressure to well bottom-hole pressures. In this study, a given well could communicate with a maximum of one grid block. Thus, multi-layer well completions were excluded from this work. Wells could either be allocated constant bottom-hole flowing pressures or constant flow rates.

Equation 17 can be written as a system of equations in the form

$$\mathbf{Ax} = \mathbf{B} \quad (20)$$

where  $\mathbf{A}$  is an  $n$  by  $n$  coefficient matrix (with  $n$  equal to the total number of grid blocks),  $\mathbf{x}$  is an  $n$  by 1 matrix representing pressures evaluated at the next time step, and  $\mathbf{B}$  is an  $n$  by 1 matrix containing the known values in Equation 18. Equation 20 was solved in this work using the Intel MKL PARDISO Version 6.1.0 matrix solver (Petra et al., 2014). The Intel MKL PARDISO package is a high-performance, robust, and memory-efficient matrix solver capable of solving large sparse systems of equations.

### 2.2.2. Solving the Concentration Field

Once the pressure field had been evaluated, particle concentration values in all grid blocks of the model were calculated. Concentration values were calculated by applying a finite difference approach to the previously discussed advection-dispersion-retention equation given in Equation 3.

$$\frac{\partial C^k}{\partial t} = \frac{\partial}{\partial x_i} \left( D_{ij} \frac{\partial C^k}{\partial x_j} \right) - \frac{\partial}{\partial x_i} (u_i C^k) - k_r C^k \quad (3)$$

The single-term retention model in Equation 3 has been shown to be valid for systems that have irreversible particle retention and no significant repulsive electromagnetic forces between particles and matrix surfaces (Li et al., 2004). However, it should be recognized that the single-term retention model is inadequate for systems which do possess significant repulsive electromagnetic forces between particles and matrix surfaces. This work incorporates the full dispersion tensor ( $D_{ij}$ ), and determines values for  $D_{ij}$  using the formulation proposed by Bear (1972 and 1979), Equations 2a – 2f. A second order accurate central finite difference scheme was used to evaluate the dispersion term in Equation 3. The finite difference evaluation of a diagonal tensor term for a given grid cell  $i$  (x direction only for brevity) was determined as

$$D_{xx} \frac{\partial^2 C_i^k}{\partial x^2} = \frac{\left( D_{xx} \frac{\partial C^k}{\partial x} \right)_{i+\frac{1}{2}} - \left( D_{xx} \frac{\partial C^k}{\partial x} \right)_{i-\frac{1}{2}}}{\Delta x} = \frac{D_{xx,i+\frac{1}{2}}(C_{i+1}^k - C_i^k) - D_{xx,i-\frac{1}{2}}(C_i^k - C_{i-1}^k)}{(\Delta x)^2} \quad (21)$$

where  $\Delta x$  is the grid size in the x direction. The  $D_{xx}$  values were evaluated at grid faces by averaging values in the two relevant adjacent grid blocks.

Off-diagonal dispersion tensor values were calculated using a second order accurate symmetric scheme (Van Es et al., 2014). The symmetric scheme began by evaluating finite difference solutions for off diagonal dispersion elements at grid corners. These corner values were then averaged to obtain the off-diagonal dispersion effect at grid centers. A schematic representation of the symmetric scheme is given in Figure 15.

Calculating the off-diagonal terms at grid corners allowed for the concentration values used in the finite difference scheme to be calculated at grid centers. The finite difference scheme for the off-diagonal term evaluated at the  $i - \frac{1}{2}, j - \frac{1}{2}$  corner of grid  $i, j$  in the XY plane was determined as (other corners and planes being omitted for brevity)

$$\begin{aligned} D_{xy} \frac{\partial^2 C_{i-1/2,j-1/2}^k}{\partial x \partial y} &= \frac{\left( D_{xy} \frac{\partial C^k}{\partial y} \right)_{i,j-1/2} - \left( D_{xy} \frac{\partial C^k}{\partial y} \right)_{i-1,j-1/2}}{\Delta x} \\ &= \frac{D_{xy,i,j-1/2}(C_{i,j}^k - C_{i,j-1}^k) - D_{xy,i-1,j-1/2}(C_{i-1,j}^k - C_{i-1,j-1}^k)}{\Delta x \Delta y} \end{aligned} \quad (22)$$

The  $D_{xy}$  values were evaluated at grid faces and determined by averaging  $D_{xy}$  values in the two relevant adjacent grid blocks.

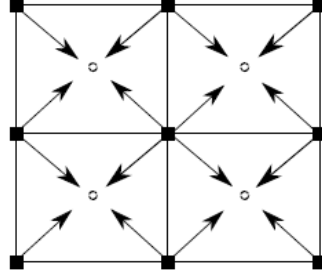


Figure 15. Symmetric scheme schematic (Van Es et al., 2014).

The advection term was evaluated using a third order accurate Quadratic Upstream Interpolation for Convective Kinematics (QUICK) scheme, as first proposed by Leonard (1979). The QUICK scheme uses a three-point stencil and quadratic interpolation at cell faces (where velocity values are stored) to evaluate the advection term at cell centers (where concentration values are stored). The QUICK scheme evaluated for grid  $i$  in the case of one-dimensional flow in the positive  $x$  direction was determined as (additional dimensions omitted for brevity)

$$\frac{\partial}{\partial x}(uC^k)_i = \frac{u_{i+1/2} \left( \frac{6}{8}C_i^k + \frac{3}{8}C_{i+1}^k - \frac{1}{8}C_{i-1}^k \right) - u_{i-1/2} \left( \frac{6}{8}C_{i-1}^k + \frac{3}{8}C_i^k - \frac{1}{8}C_{i-2}^k \right)}{\Delta x} \quad (23)$$

where  $u$  represents interstitial velocity and is evaluated at grid faces. Using the QUICK scheme ameliorates numerical diffusion in the simulator as it is a more accurate scheme than the commonly used upwind scheme (Leonard, 1993). Numerical diffusion is caused by truncation errors in finite difference approximations of the advection-diffusion equations and can result in artificial diffusion in the numerical solution (Hirsch, 2010).

The default concentration boundary condition for the finite difference simulator was that the concentration gradient across external boundaries had a value of zero. This boundary condition may be interpreted physically as allowing advection out of the system and prohibiting dispersive flux out of the system (Zheng and Wang, 1999). The simulator also allowed for fixed concentration value boundary conditions. It was also possible to prescribe concentration values to grid blocks that were not on the system's boundaries.

A first order forwards finite difference was used for the temporal derivative, which made the solution implicit. As was done for solving the pressure field, Equation 3 was written as a system of equations in the form

$$\mathbf{Ax} = \mathbf{B} \quad (20)$$

where  $\mathbf{A}$  is an  $n$  by  $n$  coefficient matrix,  $\mathbf{x}$  is an  $n$  by 1 matrix representing grid concentrations at the next time step, and  $\mathbf{B}$  is an  $n$  by 1 matrix containing the known values in Equation 3. The

resulting system of equations was solved using the Intel MKL PARDISO Version 6.1.0 matrix solver (Petra et al., 2014).

## 2.3. Finite Difference Model Verification and Validation

### 2.3.1. Pressure Solution Verification

A series of verification and validation tests were performed to investigate the validity of the finite difference simulator. The first two tests evaluated the accuracy of the simulator's pressure solution by comparing it with the analytical solution for a well producing from an infinite isotropic media. Such a system can be described mathematically as having an initial condition of

$$p(r, 0) = p_0, \quad 0 \leq r < \infty, \quad (24)$$

and boundary conditions

$$p(r, t) = p_0 \quad \text{as } r \rightarrow \infty, \quad t \geq 0 \quad (25)$$

$$r \frac{\partial p}{\partial r} = \frac{Q\mu}{2\pi kh} \quad \text{as } r \rightarrow 0, \quad t > 0 \quad (26)$$

where  $r$  is the radial distance from the well,  $Q$  is a fixed volumetric flow rate from the well, and  $h$  is the thickness of the system. The analytical solution for pressure as a function of radial distance from the well, as derived by Chen (2007), is given by

$$p(r, t) = p_0 + \frac{Q\mu}{4\pi kh} Ei \left( -\frac{r^2 \phi \mu c_t}{4tk} \right) \quad (27)$$

where  $Ei$  is the exponential integral function. A two-dimensional finite difference model with a single producing well at its center was created to mimic flow in an infinite isotropic system. Details of the parameters used in the simulation are provided in Table 4.

Pressure profiles in the system were generated for three values of simulated time (0.01, 0.02, and 0.1 days). The times were selected so that the pressure drop due to well production had not yet reached the outer boundaries of the model. Each of the three simulations used 10 time steps. Simulation results and their corresponding analytical solutions are shown in Figure 16.

The pressure solution given by the finite difference simulator had a maximum difference compared to the analytical solution of .036 percent, and an average difference less than .01 percent. Thus, in this case the pressure solution given by the finite difference simulator matched the analytical solution with a high degree of accuracy.

Table 4. Parameters for first pressure validation case.

Property	Value	Unit
Length in X direction	8000	ft
Length in Y direction	8000	ft
Number of gridblocks in X direction	101	
Number of gridblocks in Y direction	101	
Well flow rate	5000	bbl/day
Initial system pressure	1500	psi
Wellbore radius	0.25	ft
Porosity	0.2	
Permeability	100	md
Total compressibility	1E-06	1/psi
System height	250	ft
Fluid viscosity	1	cp

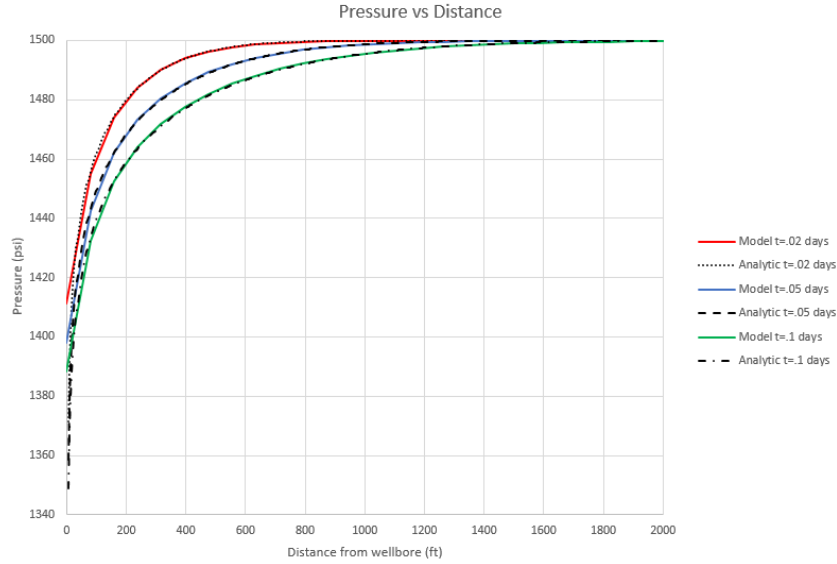


Figure 16. Pressure profiles for first pressure verification case.

A second verification test for the pressure solution was performed using the analytical pseudosteady-state solution for a well flowing at the center of a finite cylindrical system with a constant bottom-hole pressure. If such a system has an initial condition of

$$p(r, 0) = p_0, \quad 0 \leq r \leq r_e, \quad (28)$$

where  $r_e$  represents the distance from the center of the system to the external boundary, and the pseudosteady-state boundary condition of

$$\frac{\partial p}{\partial r} = 0 \text{ at } r = r_e, \quad t > 0, \quad (29)$$

then, as demonstrated by Craft and Hawkins (1959), the production rate from the well,  $q$ , may be given by

$$q = \frac{2\pi kh(\bar{p} - p_{wf})}{\mu B \left[ \ln\left(\frac{r_e}{r_w}\right) - \frac{3}{4} \right]} \quad (30)$$

where  $\bar{p}$ ,  $p_{wf}$ ,  $B$ , and  $r_w$ , represent volumetrically averaged reservoir pressure, well bottom-hole pressure, fluid formation volume factor, and wellbore radius, respectively. For comparison with the pseudosteady-state analytical solution, a two-dimensional finite difference model was created. The finite difference model had a single well at its center producing at a constant bottom-hole pressure. Detailed parameters for the finite difference system are listed in Table 5.

Table 5. Parameters for second pressure validation case.

Property	Value	Unit
Length in X direction	1100	ft
Length in Y direction	1100	ft
Number of gridblocks in X direction	51	
Number of gridblocks in Y direction	51	
Well bottom-hole pressure	1000	psi
Initial system pressure	1500	psi
Wellbore radius	0.25	ft
Porosity	0.2	
Permeability	100	md
Total compressibility	1E-06	1/psi
System height	250	ft
Fluid viscosity	1	cp
Formation volume factor	1	RB/STB

The value for  $r_e$  used when computing flow rates via Equation 29 was calculated by equating the surface area of the finite difference model to the area of a circle with radius  $r_e$ . For this system,  $r_e$  was calculated to be 620.61 ft. Figure 17 provides a comparison of the flow rates given by Equation 28 and the finite difference simulator.

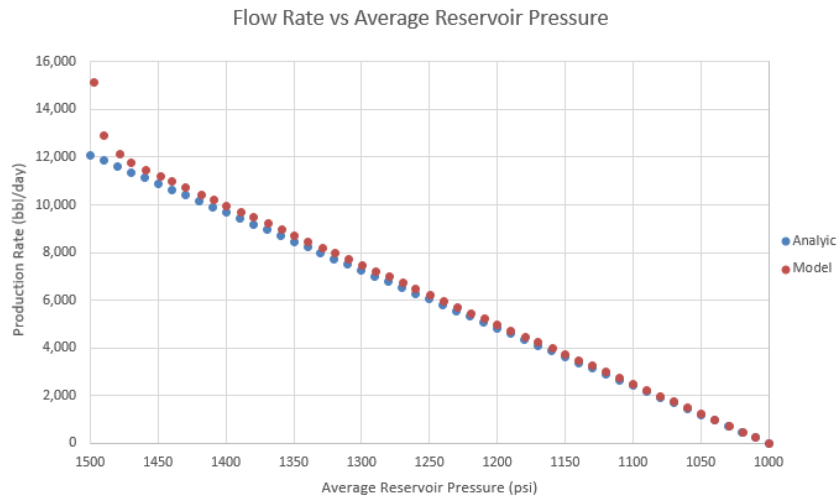


Figure 17. Flow rate vs average reservoir pressure for second pressure validation case.

The higher flow rates given by the finite difference model can be attributed to transient flow in the model. Transient flow occurs when the pressure decrease due to well production has not reached the outer boundary of the system. Once the pressure at the outer boundary begins to decrease at a constant rate, the system enters pseudosteady-state flow. After the transient flow period, the flow rates given by the finite difference model are consistent with the analytical pseudosteady-state flow solution. Given that the simulated flow rates were a function of the system's pressures, it can be inferred that the pressure solution given by the finite difference model was accurate.

### 2.3.2. Well Model and Boundary Condition Verification

To verify the well model and boundary condition implementation a comprehensive hypothetical case was solved. Problem 7.7 from Abou-Kassem et al. (2006) was used as the verification problem. This case incorporates many features of the simulator and requires implementation of pressure, flow rate, and pressure gradient boundary conditions, as well as bottom-hole pressure and flow rate well constraints. The example system consists of a two by two grid system, with boundary conditions as depicted in Figure 18.

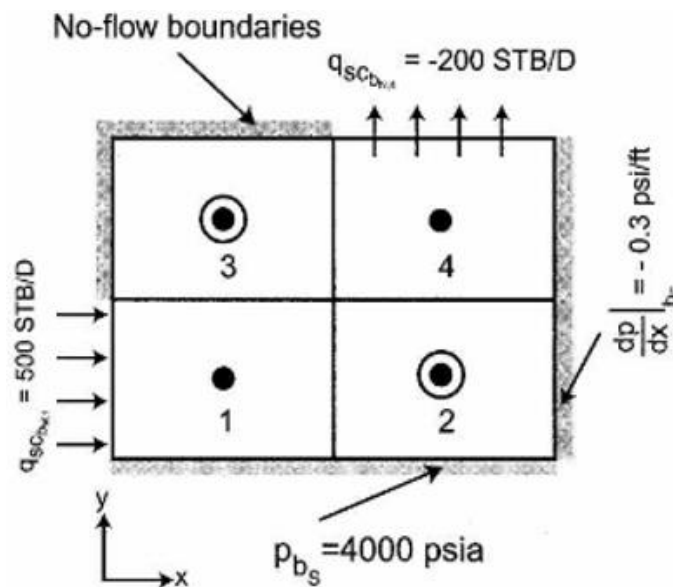


Figure 18. System and boundary conditions for example 7.7 of Abou-Kassem et al. (2006).

Other simulation parameters are summarized in Tables 6 and 7.



Table 6. System parameters for example 7.7 of Abou-Kassem et al. (2006).

Property	Value	Unit
Permeability in X direction	150	md
Permeability in Y direction	100	md
Porosity	0.27	
Gridblock length in X direction	350	ft
Gridblock length in Y direction	250	ft
System height	30	ft
Formation volume factor	1	RB/STB
Fluid viscosity	3.5	cp

Table 7. Well parameters for example 7.7 of Abou-Kassem et al. (2006).

Production well in gridblock 2		
Property	Value	Unit
Wellbore radius	0.25	ft
Well bottom-hole pressure	2000	psi
Production well in gridblock 3		
Property	Value	Unit
Wellbore radius	0.25	ft
Well flow rate	600	STB/day

After three time step iterations, the finite difference model pressure solution converged to the solution provided by Abou-Kassem et al. (2006). A comparison of output pressure data from the simulator to the data provided in the text is shown in Table 8.

Table 8. Result comparison for problem 7.7 of Abou-Kassem et al. (2006).

Grid Block	Text Pressure (psi)	Model Pressure (psi)	Percent difference
1	3772.36	3772.3602	5.30E-06
2	3354.20	3354.1978	6.56E-05
3	3267.39	3267.3900	0.00E+00
4	3187.27	3187.2713	4.08E-05

The difference between the simulated pressures and those given by Abou-Kassem et al. (2006) was negligible for all four grid blocks. This agreement provides strong evidence that well and boundary conditions used in the finite difference simulator were correctly implemented.

### 2.3.3. Pure Advection

The finite difference solution for transport in the case of pure advection (no diffusion or retention) was validated using the analytical solution for transport in a semi-infinite one-dimensional

medium. For this test, the inlet boundary was held at a constant concentration value of  $C_0$ . The initial and boundary conditions for this case may be written as

$$C(x, t) = 0, \quad x > 0, \quad t = 0 \quad (31)$$

$$C(x, t) = C_0, \quad x = 0, \quad t > 0 \quad (32)$$

With no dispersion or retention, the analytic concentration profile is equivalent to a step function from  $C_0$  to zero. All concentration values upstream of the front are  $C_0$ , while all values downstream of the front are zero. The location of the vertical front can be calculated by multiplying interstitial fluid velocity by time elapsed after the initiation of the constant concentration boundary condition. The finite difference simulator was used to model this case by imposing an interstitial velocity of 0.5 feet per second in a 1-foot long system, for a total simulation time of one second. Under these conditions, at a time of one second, the analytic concentration front is located 0.5 feet from the origin. Three simulations were performed with the number of time steps increasing from 100 to 250 to 500 to investigate the effect of numerical dispersion. The results of these three simulations and their comparison to the analytic solution is depicted in Figure 19.

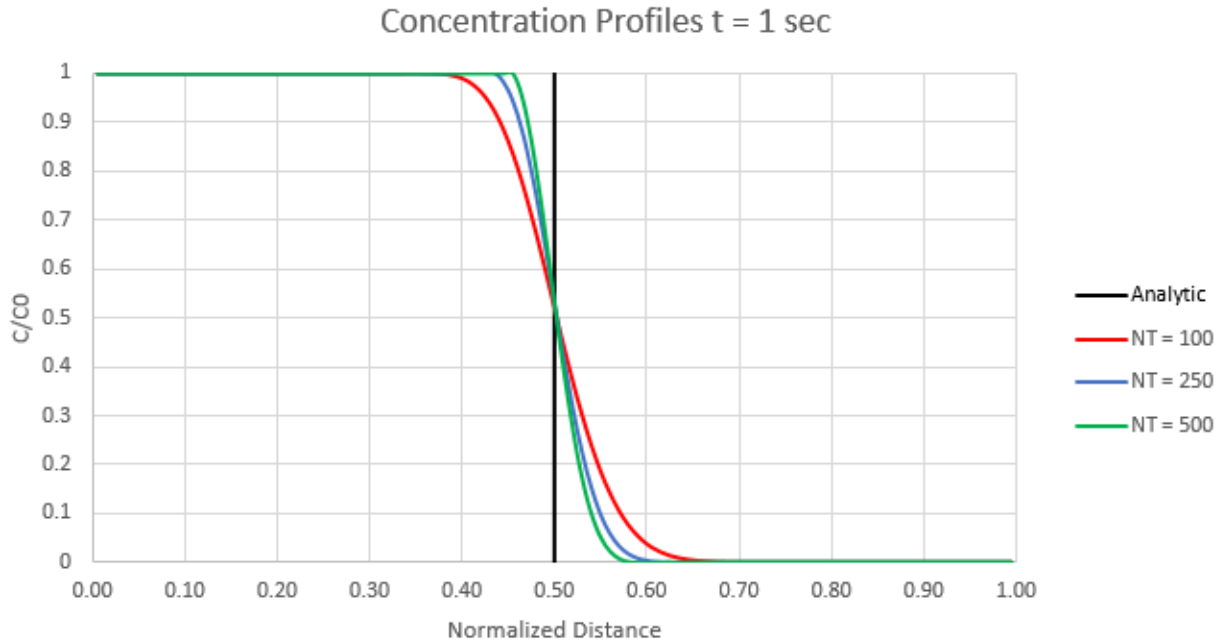


Figure 19. Concentration profiles for pure advection verification case.

As the number of time steps in the simulation increases numerical dispersion decreases, and the finite difference solution converges towards the analytical solution. In practice, the effects of numerical dispersion become insignificant when physical dispersion is dominant. The conditions encountered in this work all had a dispersive component and thus were never purely advective. The results of this verification study demonstrate that, if necessary, numerical diffusion can be reduced by increasing the number of time steps simulated.

### 2.3.4. Pure Diffusion

A second verification test was performed to model transport in the case of pure diffusion (no advection or retention) in a semi-infinite one-dimensional medium. With no advection, dispersion reduces to molecular diffusion. The same boundary conditions of constant inlet concentration as used in the pure advection verification case (Equations 30 and 31) were used. The analytic solution for this situation, as given by Ogata and Banks (1961), simplifies to

$$C(x, t) = C_0 \left[ \operatorname{erfc} \left( \frac{x}{2\sqrt{Dt}} \right) \right] \quad (33)$$

where  $\operatorname{erfc}$  is the error-function complement. Two simulations were performed with values of molecular diffusion coefficient equal to  $1 \times 10^{-5}$  and  $5 \times 10^{-5} \text{ cm}^2/\text{s}$ . These values are representative of many common solute species in water (Cussler, 1997). For each value of molecular diffusion coefficient, concentration profiles were compared to the analytical solution at times of 1, 5, and 10 days. The total length of the simulated system was 1 foot. For all simulations, the number of grid blocks used was 100 and the number of timesteps was 100. Results of the two simulations and their comparison to the analytic solution is depicted in Figure 20.

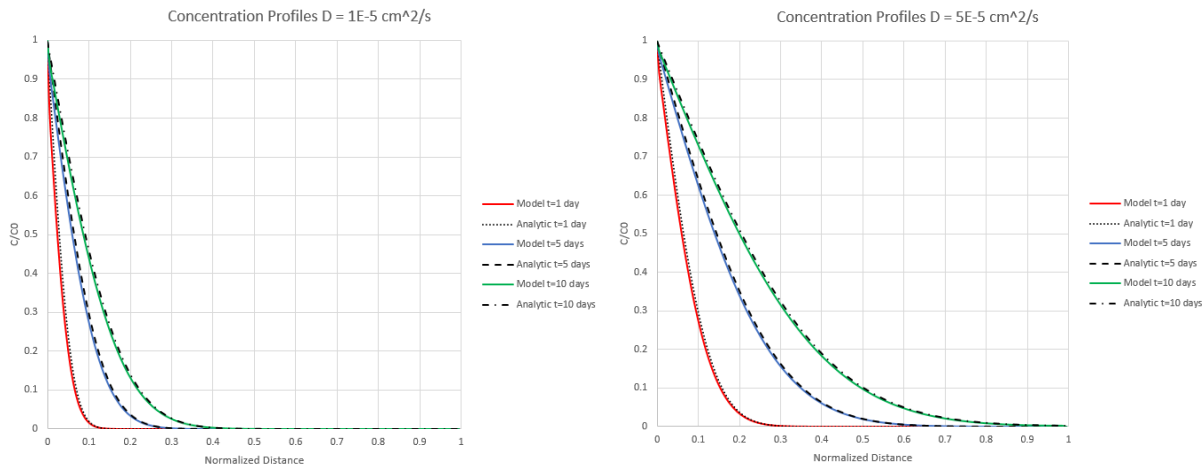


Figure 20. Concentration profiles for pure diffusion verification case.

The finite difference simulator accurately predicted concentration profiles for both low and high values of molecular diffusion, across a wide range of simulated times. Given the strong correlation between the model and the analytical solution, diffusion and physical dispersion were considered to be correctly implemented by the finite difference simulator.

### 2.3.5. Advection with Dispersion and Retention

A verification test was performed to investigate the ability of the finite difference model to simulate transport in the case of simultaneous advection, dispersion, and retention. The modeled system used was semi-infinite, one-dimensional, and had boundary conditions as defined by

Equations 30 and 31. The analytical solution for this case given by Van Genuchten and Alves (1982) may be written as

$$C(x, t) = \frac{C_0}{2} \left\{ \exp \left[ \frac{x(u - G)}{2D} \right] \operatorname{erfc} \left[ \frac{x - Gt}{2\sqrt{Dt}} \right] + \exp \left[ \frac{x(u + G)}{2D} \right] \operatorname{erfc} \left[ \frac{x + Gt}{2\sqrt{Dt}} \right] \right\} \quad (34)$$

where  $G = u \sqrt{1 + \frac{4k_r D}{u^2}}$  (35)

Four simulations with retention coefficients ( $k_r$ ) of 0.0, 0.01, 0.025, and 0.05  $\text{s}^{-1}$  were performed to model a range of low to moderate degrees of particle retention. The dispersion coefficient was fixed at a constant value for all simulations, as the analytical solution does not provide for a velocity dependent dispersion coefficient. Detailed simulation parameters are provided in Table 9.

Table 9. Parameters for advection, dispersion, retention verification.

Property	Value	Unit
System Length	1	ft
Interstitial Velocity	0.05	ft/s
Dispersion Coefficient	1	$\text{cm}^2/\text{s}$
Total Simulation Time	1.0E-04	days
Number of Gridblocks	100	
Number of Time Steps	500	

Concentration profiles from the four simulations and the corresponding analytical solutions are plotted in Figure 21.

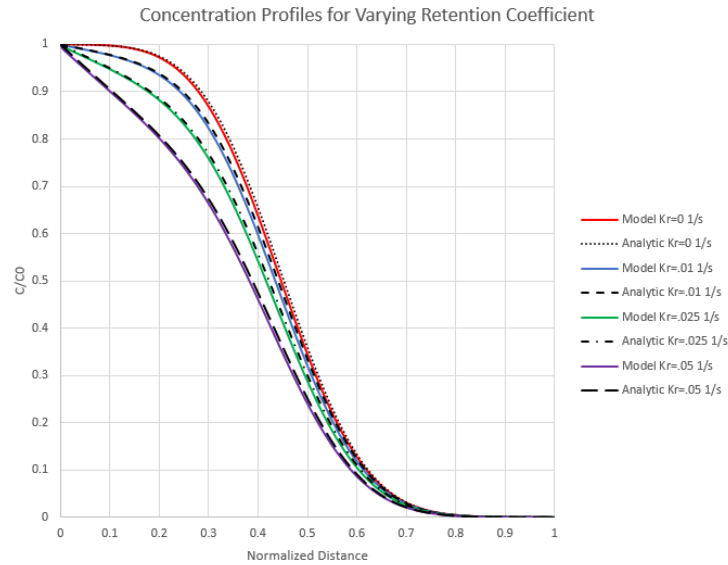


Figure 21. Concentration profiles for advection, dispersion, retention verification.

Simulations for all four levels of retention coefficient were in close agreement with the analytical solutions, providing confirmation that retention had been implemented accurately in the finite difference simulator.

### 2.3.6. Radial Diffusion

To verify that the finite difference simulator was functional in multiple dimensions, a radial diffusion case was modeled. If a cylindrical system is internally bound by a cylinder with radius  $r = a$  and has the initial condition

$$C(r, t) = 0, \quad 0 \leq r < \infty, \quad t > 0, \quad (36)$$

and a boundary condition of

$$C(r, t) = C_0, \quad r = a, \quad t > 0, \quad (37)$$

then, as illustrated by Crank (1975), the analytical solution for concentration as a function of radial distance and time may be written as

$$C(r, t) = C_0 + \frac{2C_0}{\pi} \int_0^\infty \exp(-Dw^2t) \frac{J_0(wr)Y_0(wa) - J_0(wa)Y_0(wr)}{J_0^2(wa) + Y_0^2(wa)} \frac{dw}{w} \quad (38)$$

where  $J_0$  and  $Y_0$  are Bessel functions of the first and second kind respectively. As further illustrated by Crank (1975), Equation 38 may be approximated for small time values as

$$C(r, t) = C_0 \left[ \left( \frac{a}{r} \right)^{1/2} \operatorname{erfc} \left( \frac{r-a}{2\sqrt{Dt}} \right) + \frac{(r-a)(Dt)^{1/2}}{4a^{1/2}r^{3/2}} \operatorname{ierfc} \left( \frac{r-a}{2\sqrt{Dt}} \right) + \frac{Dt(9a^2 - 2ar - 7r^2)}{32a^{3/2}r^{5/2}} \operatorname{i^2erfc} \left( \frac{r-a}{2\sqrt{Dt}} \right) + \dots \right] \quad (39)$$

where

$$\operatorname{ierfc}(x) = \frac{1}{\pi^{1/2}} e^{-x^2} - x \operatorname{erfc}(x) \quad (40)$$

$$\operatorname{i^2erfc}(x) = \frac{1}{4} [\operatorname{erfc}(x) - 2x \operatorname{ierfc}(x)] \quad (41)$$

A finite difference system was created to match the boundary condition of Equation 36 as closely as possible. The system created was two-dimensional, contained 25 grid blocks in both the X and Y directions, and had grid block side lengths of .01 feet in all directions. Due to the Cartesian basis of the finite difference model, the radial boundary condition was approximated using a “stair step” approach. Figure 22 depicts the lower 6 by 6 region of the 25 by 25 grid system, and illustrates how the “stair step” approach was implemented.

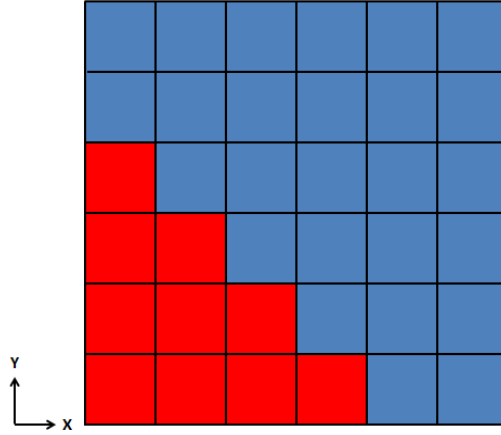


Figure 22. “Stair step” boundary implementation.

A total of 10 grid blocks (red blocks in Figure 22) were kept at a concentration value of  $C_0$  during the entire simulation. The radius of the internally bound cylinder,  $a$ , was calculated to be 0.357 ft. This value was obtained by equating the area of a quarter circle with radius  $a$  to the area of the 10 grid blocks held at  $C_0$ . Results for simulations using values of  $Dt/a^2$  of 0.25 and 1.0 are shown in Figure 23.

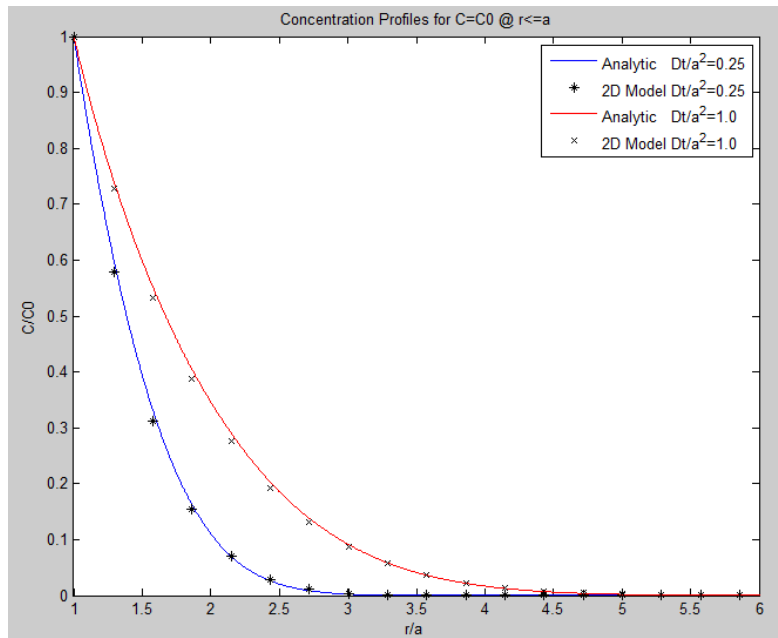


Figure 23. Radial diffusion concentration profiles.

Given that the grid blocks of the finite difference simulator were defined in a Cartesian grid, it was not possible to replicate a radial system exactly. Despite this limitation, the maximum percent error between any concentration value given by the finite difference model and the corresponding value given by the approximate analytical solution (Equations 39-41) was 7.06 percent. Due to this

favorable agreement with the approximate analytical solution, the finite difference simulator was shown to be capable of accurately solving concentration fields in multi-dimensional systems.

### 2.3.7. Full Dispersion Tensor

A qualitative and quantitative analysis was performed to investigate the incorporation of the full dispersion tensor into the finite difference simulator. In principle, it was necessary to incorporate the full dispersion tensor as particle dispersion could occur in directions that were not aligned with the principal directions of the Cartesian continuum-scale model. A series of simulations were performed in which a single grid block at the center of a square two-dimensional system was held at constant concentration  $C_0$ . For all simulations, the system dimensions were 10ft by 10ft by 1 ft, total simulated time was 1.0E-3 days and simulation time steps were 5.0E-5 days. Additionally, all simulations were purely diffusive (no advection); however, the full dispersion tensor was modified to cause anisotropic diffusion. As a base case, the first simulation modeled equivalent dispersion in all directions. Thus, the dispersion coefficient aligned with the x direction,  $D_{xx}$ , was set equal to that in the y direction,  $D_{yy}$ , and diagonal dispersion coefficients were set to zero. The concentration field for the control simulation, which used  $D_{xx} = D_{yy} = 25.0 \text{ cm}^2/\text{s}$  and 51 grids in the X and Y directions, is shown in Figure 24.

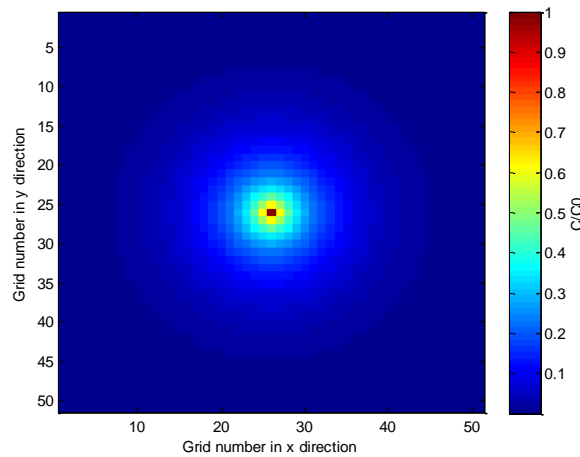


Figure 24. Concentration field for equivalent dispersion in all directions.

The radially symmetric concentration field indicates that dispersion was equivalent in all directions, which shows that the base case model was implemented correctly. The second simulation reduced  $D_{yy}$  to  $2.5 \text{ cm}^2/\text{s}$  (one order-of-magnitude) and kept  $D_{xx}$  at  $25.0 \text{ cm}^2/\text{s}$ . Such a dispersion tensor could occur when a high velocity flow field is aligned with the x direction. The final concentration field for this simulation, performed on a 51 by 51 grid system, is shown in Figure 25.

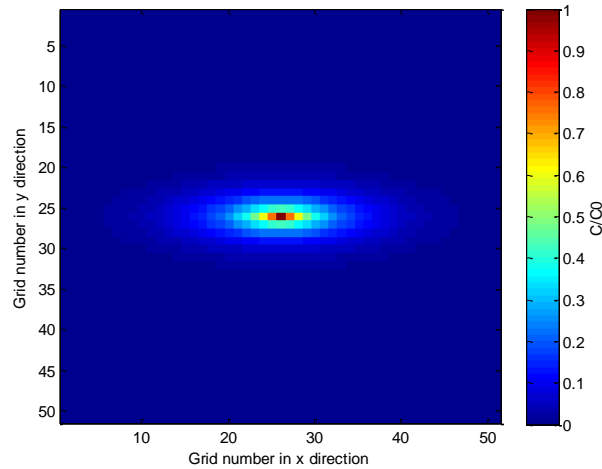


Figure 25. Concentration field for dominant dispersion in x direction.

The elongated concentration profile in the x direction indicates that dispersion in the x direction is indeed much larger than the y direction. The previous two simulations had dispersion tensors with all off diagonal elements equal to zero, which served as a basis for comparison. If the velocity vector of fluid flow in a grid cell is not aligned with one of the principal Cartesian directions, the dispersion tensor effectively undergoes a rotation transformation. This transformation results in non-zero off-diagonal elements of the dispersion tensor. To represent such a situation, two additional simulations were performed in which the dispersion tensor of the second simulation (dominant dispersion in X direction) was rotated. The two rotation transformations used were 20- and 45-degree clockwise rotations. Dispersion tensors for all four simulations are summarized in Table 10 (all dispersion values in  $\text{cm}^2/\text{s}$ ).

Table 10. Dispersion tensor values.

Simulation	Dxx	Dyy	Dxy	Dyx	Rotation (Degrees)
1	25	25	0	0	0
2	25	2.5	0	0	0
3	22.37	5.13	-7.23	-7.23	20
4	13.75	13.75	-11.25	-11.25	45

The final concentration fields for the rotated dispersion tensor simulations, performed on a 51 by 51 grid system, are shown in Figure 26.



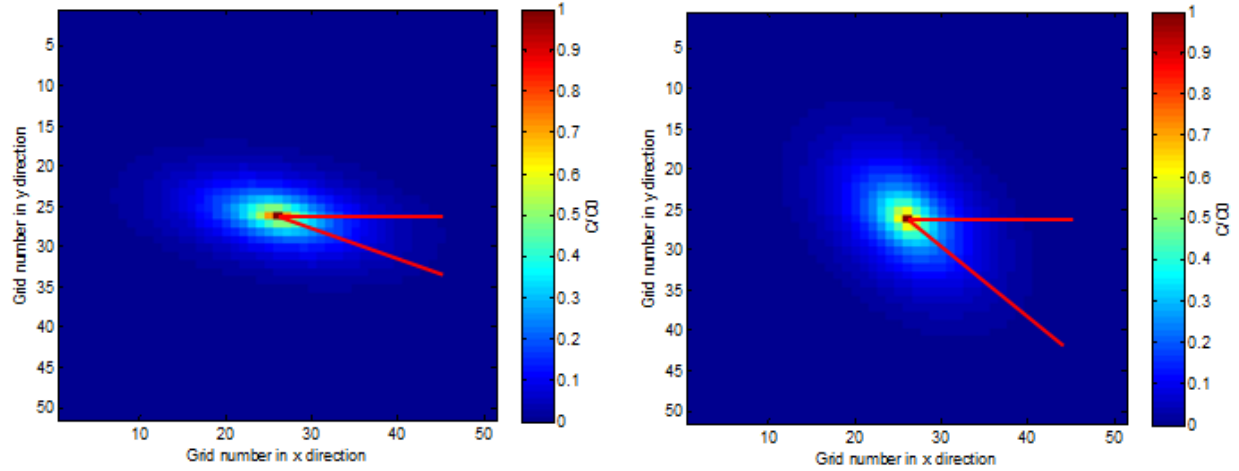


Figure 26. Concentration field for 20-degree (left) and 45-degree (right) rotation.

The superimposed red lines in Figure 26 depict 20-degree and 45-degree angles. For both cases, the direction of maximum dispersion is aligned with the degree of rotation, which indicates the finite difference solution correctly implemented the off-diagonal elements of the dispersion tensor.

Compared to the base case of Figure 25 however, the concentration fields in Figure 26 appear to have lower concentration gradients in the transverse direction. Thus, rotation appears to artificially cause additional dispersion in the transverse direction. This effect is likely due to the Cartesian nature of the grid-based simulator. When a concentration front spreads along a direction that is not one of the principal Cartesian directions, it cannot travel in a straight line. Instead the front must take a “stair step” path, which will result in artificially high dispersion in the transverse direction and artificially low dispersion in the longitudinal direction. This effect will be most pronounced when the longitudinal flow direction is least aligned with a principal Cartesian direction. In a two-dimensional system, this occurs at a 45-degree angle to the principal Cartesian directions. This effect can be seen in Figure 26 as the ratio of longitudinal spreading to transverse spreading of concentration is lowest for the 45-degree case.

This effect can be mitigated by increasing the grid refinement. To investigate, a series of simulations were performed with the same parameters as simulations 3 and 4 in Table 10 but with increasing numbers of finite difference grids. Simulations were performed for grid systems of 11 by 11 (121 grids), 51 by 51 (2,601 grids), 101 by 101 (10,201 grids), 251 by 251 (63,001), and 317 by 317 (100,489 grids). For each simulation, a concentration profile was recorded. For the 20-degree rotation case, the concentration profile was taken from the system origin to the edge located at  $x = 10\text{ft}$ ,  $y = 5\text{ft}$  (middle of right edge). For the 45-degree rotation case, the concentration profile was taken from the system origin to the corner located at  $x = 10\text{ft}$ ,  $y = 10\text{ft}$ . Results for all simulations are shown in Figures 27 and 28.

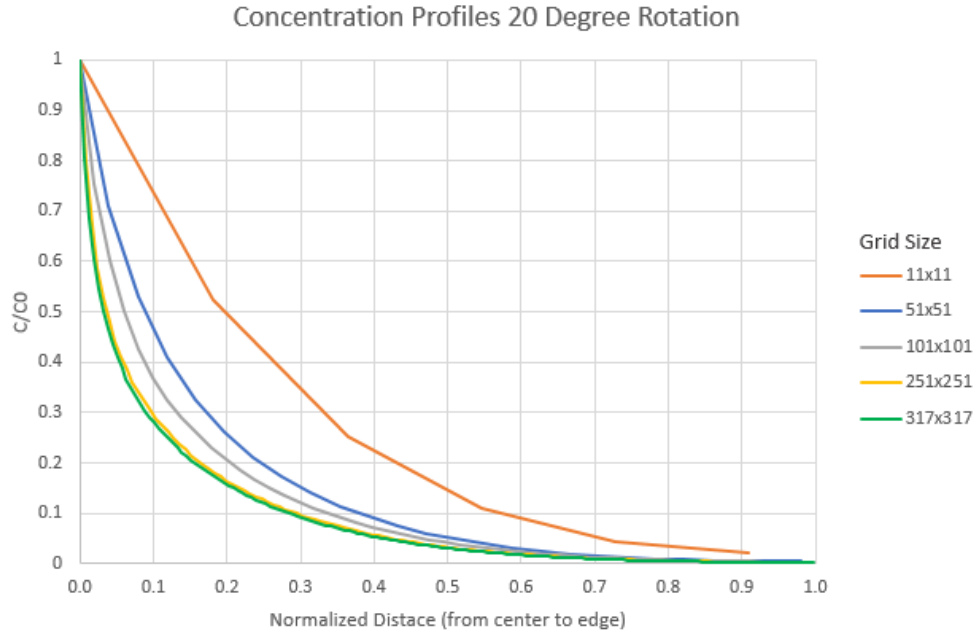


Figure 27. Concentration profiles for 20-degree rotation.

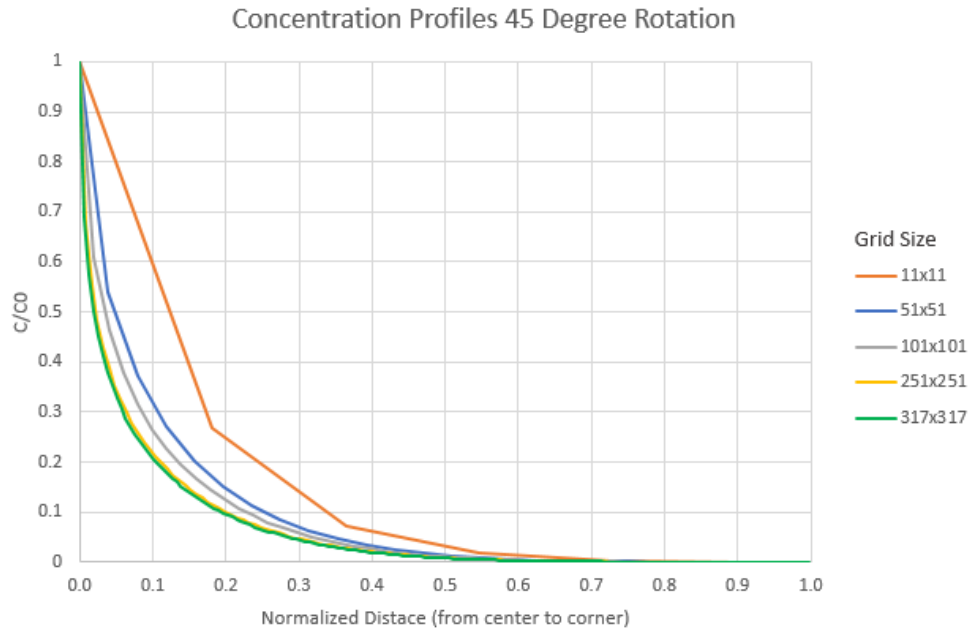


Figure 28. Concentration profiles for 45-degree rotation.

Concentration profiles for both simulations converge as the number of grid blocks used increases. This implies that increasing grid refinement can reduce errors due to concentration fields spreading in directions not aligned with the principal Cartesian directions of the system.

## 2.4. Concurrently Coupled Model

### 2.4.1. Concurrently Coupled Model Overview

The algorithm used to run the concurrently coupled simulator developed in this work is depicted in Figure 29.

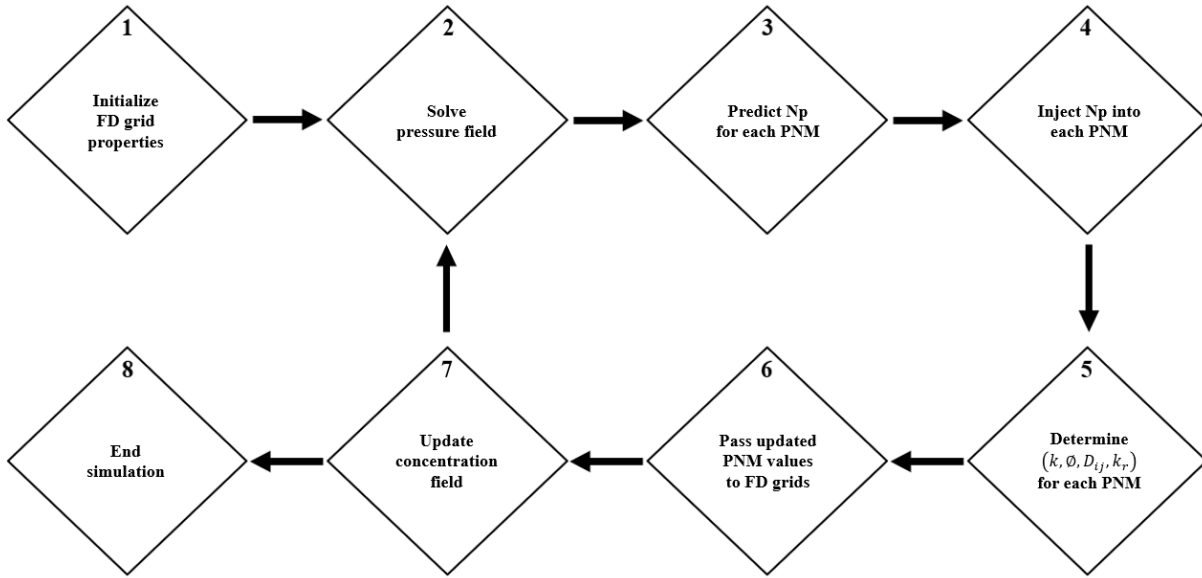


Figure 29. Algorithm for concurrently coupled particle transport and retention simulations.

Each finite difference grid block in the concurrently coupled model was first initialized with the properties of the embedded PNMs (Step1). Each time step then began by solving the pressure field (Step 2). In Step 3, the velocity flow field (derived from the pressure field) and the particle concentration field were used to predict the number of particles ( $N_p$ ) for each particle species that would enter each PNM during the time step. Simulations were then performed in Step 4 in which the number of particles as predicted in Step 3 were used to damage each embedded PNM. In Step 5, simulations were performed in each grid block (distinct from those in Step 4) to determine the continuum-scale properties of interest: permeability, porosity, retention coefficient, and dispersion coefficient (longitudinal and transverse). Retention and dispersion coefficients were determined for each particle species. These properties were then assigned to each finite difference grid block (Step 6) and the concentration field was solved for (Step 7). The two-way transfer of information, between the PNMs and continuum-scale grids (Steps 2 through 7), continued until the simulation was complete (Step 8). It is important to note that the user could select the frequency at which PNM property updates via PNM simulation occurred (Steps 3 through 6). This enabled high temporal resolution for pressure and concentration field updates, which helped to reduce numerical dispersion, while allowing the algorithm to run in a timely manner.

## Chapter 3. Results and Discussion

### 3.1. One-Dimensional Concurrent Coupling

Simulations with gradually increasing size discrepancies between embedded pore-scale models and finite difference grid blocks were run to identify potential challenges associated with the concurrently coupled particle filtration model. Simulations with no size discrepancy between the pore- and continuum-scale models, referred to in this work as 1-to-1 simulations, were first used to ensure that the boundary condition and parameter coupling had been implemented correctly and to evaluate the potential impact of numerical dispersion. These simulations were followed by simulations involving finite difference grid blocks three times larger than their embedded PNMs. The final one-dimensional concurrently coupled simulations involved finite difference grid blocks eleven times larger than their embedded PNMs. Additional concurrently coupled simulations with bidisperse particle systems were run at various pore- and continuum-scale size discrepancies. The accuracy of each concurrently coupled simulation was validated by a boundary coupled simulation with identical input parameters, such as particle concentration and system size. While the concurrently coupled simulations generated particle concentration information using a finite difference approximation to the modified version of the advection dispersion equation given by Equation 3, boundary coupled simulations tracked the pore-to-pore transport of each individual particle. The direct particle tracking of the boundary coupled simulations provided a fundamentally reliable representation of overall particle transport behavior that was used to evaluate the accuracy of the concurrently coupled simulations.

#### 3.1.1. One-Dimension 1-to-1 Concurrent Coupling with No Retention

A series of one-dimensional simulations with no particle retention were used to verify that the concurrently coupled model had been correctly developed. In the simulations, the continuum-scale finite difference model occupied the same volume as the embedded PNMs. When the continuum- and pore-scale models occupy the same volume and represent the same system, the behavior of the concurrently coupled system should replicate the behavior of a system containing only boundary coupled PNMs.

Simulations involving only boundary coupled PNMs were first run to serve as a basis for comparison for the concurrently coupled model. The simulated systems consisted of 20 boundary coupled PNMs. Injection of 50,000 particles at a constant rate into the system over 0.5 system pore volumes was simulated. A particle diameter size of 0.01 microns was used for all particles to ensure that they were too small to become trapped in the PNMs. In the simulations a constant flow rate boundary condition, which corresponded to a Darcy velocity of 0.01 cm/s was imposed, together with a constant fluid viscosity of 0.01 g/cm-s. At 0.5 pore volumes of injected fluid, particle concentrations were calculated in each grid block. Simulations for these conditions used Berea PNMs, random uniform (RU) PNMs, and Lattice PNMs. See section 2.1.1. for more information on these PNM systems. The resulting particle concentration profile at 0.5 pore volumes for each of the three PNM systems is shown in Figure 30.

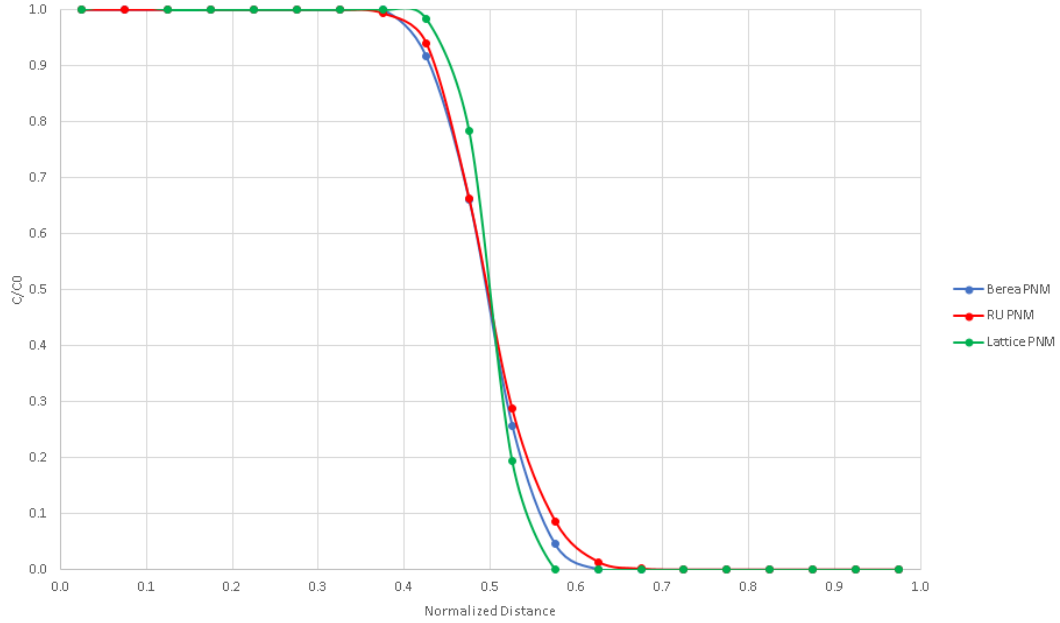


Figure 30. Concentration profiles of 50,000 particles injected into 20 boundary coupled PNM at 0.5 system pore volumes.

A comparison with the analytic solution for a constant injection concentration (Equations 34 and 35) was made to test the validity of the concentration profiles generated using the boundary coupled PNM simulations. Values for longitudinal dispersion and retention coefficients are required to generate the analytic solutions. These coefficients were obtained in separate simulations that used the same boundary conditions as the previous simulations. Section 2.1.3. provides details on the methods used to evaluate the dispersion coefficient. Dispersion coefficient values of  $1.0\text{E-}3 \text{ cm}^2/\text{s}$ ,  $1.2\text{E-}3 \text{ cm}^2/\text{s}$ , and  $5.0\text{E-}4 \text{ cm}^2/\text{s}$  were calculated for the Berea PNM, RU PNM, and Lattice PNM, respectively. Table 11 summarizes the parameters used in the analytical solution for each PNM. Figures 31 to 33 provide comparisons of the boundary coupled concentration profiles at 0.5 system pore volumes (Figure 30) to the analytical solutions using the parameters from Table 11 for each PNM system.

Table 11. Parameters for analytical solution for concentration profiles of particles injected into 20 boundary coupled PNM at 0.5 system pore volumes.

Pore Network Model	Dispersion Coefficient ( $\text{cm}^2/\text{s}$ )	Retention Coefficient (1/s)	Interstitial Velocity ( $\text{cm}/\text{s}$ )	Time (s)	PNM Length (cm)
Berea Sandstone	1.00E-03	0.0	6.56E-02	53.4	7.0
Random Uniform	1.20E-03	0.0	2.56E-02	349.3	17.9
Lattice	5.17E-04	0.0	1.12E-01	35.6	8.0

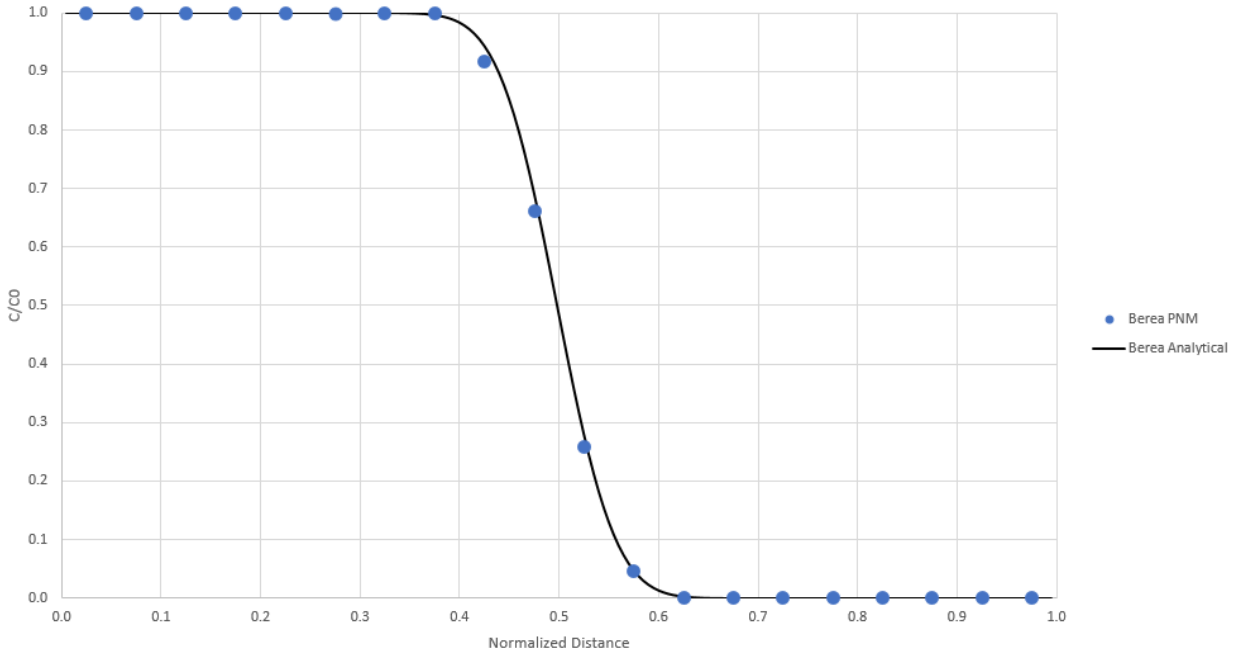


Figure 31. Analytical and simulated concentration profile of 50,000 particles injected into 20 boundary coupled PNMs at 0.5 system pore volumes (Berea PNM).

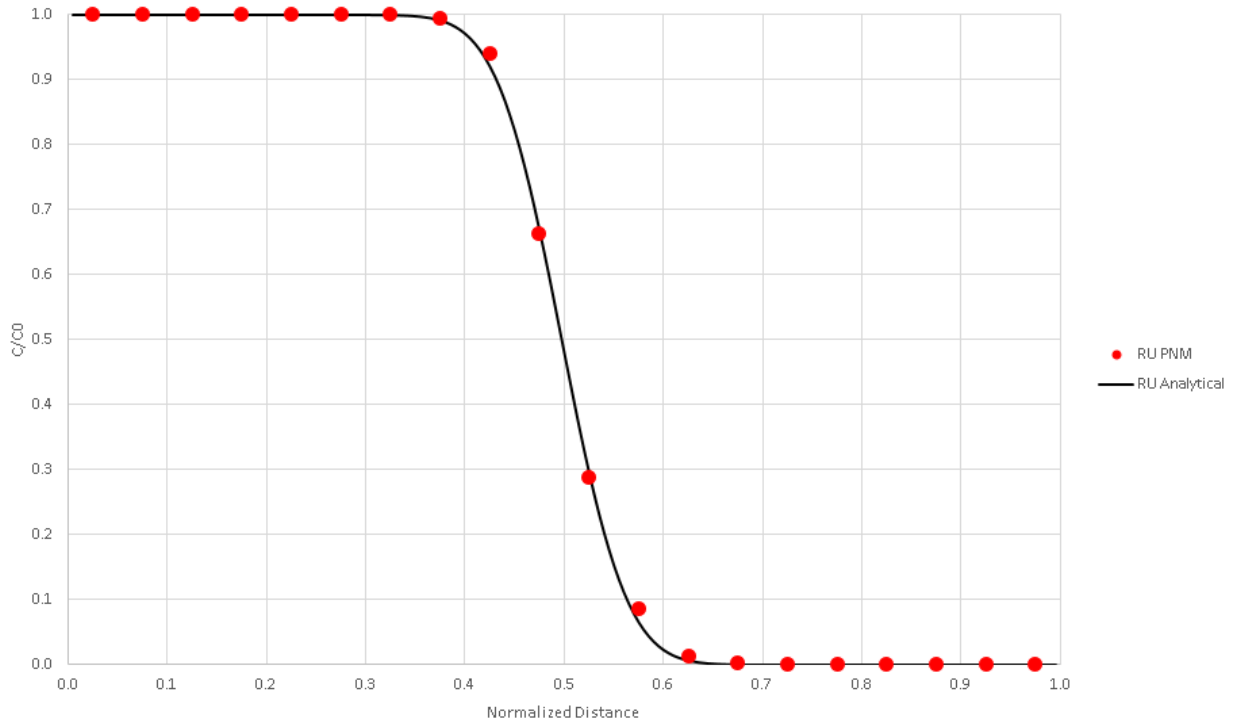


Figure 32. Analytical and simulated concentration profile of 50,000 particles injected into 20 boundary coupled PNMs at 0.5 system pore volumes (RU PNM).

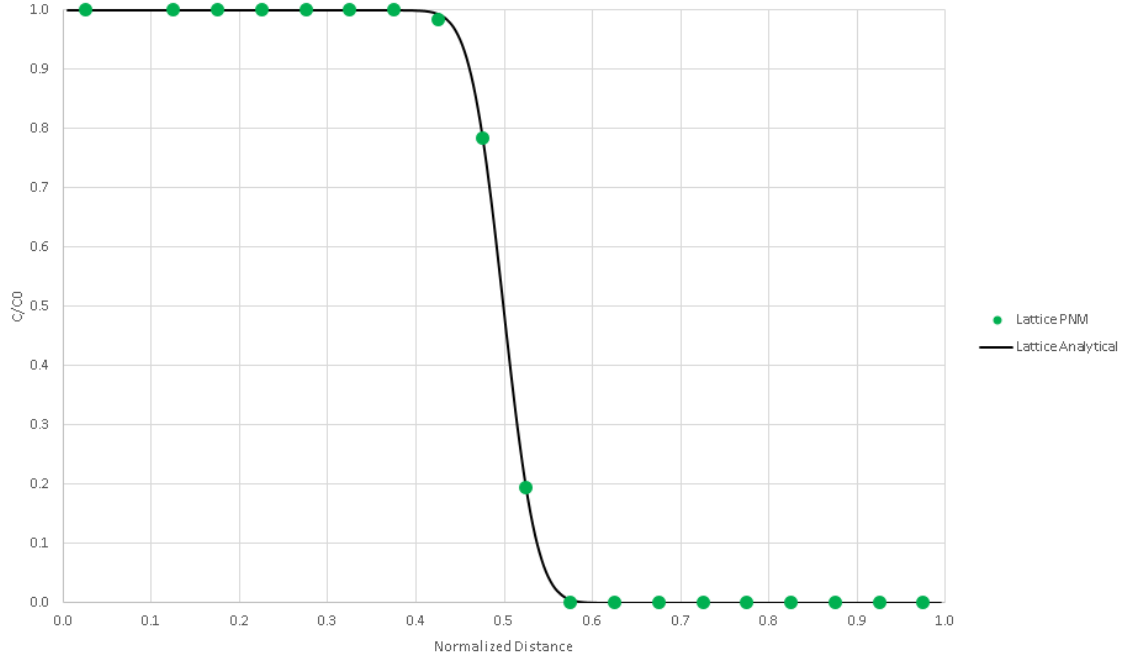


Figure 33. Analytical and simulated concentration profile of 50,000 particles injected into 20 boundary coupled PNMs at 0.5 system pore volumes (Lattice PNM).

The qualitative agreement of the matches between the analytical and simulated concentration curves provide support to the validity of the coefficient values. Additionally, because the simulated boundary coupled PNM concentration profiles match the analytical solutions, it can be inferred that, in the absence of retention, the PNM simulations produce physically realistic results consistent with classical theory. Given that the continuum-scale model developed in this work uses a finite-difference solution based on an approximate form of classical theory, it should therefore be in agreement the boundary coupled PNM solution when accurate coefficient values are used and numerical dispersion is small.

To verify that the finite difference model used by the concurrently coupled model *could* match the boundary coupled PNM solutions for particle transport, a series of simulations using only the finite difference model were performed (without embedded PNM simulations and coupling). These simulations were run with varying spatial and temporal resolutions with the same system parameters and boundary conditions of the previous boundary coupled PNM simulations. The retention and dispersion coefficients used were those obtained from the PNM simulations summarized in Table 11. Results for the three relevant dispersion coefficient values are shown in Figures 34-36.

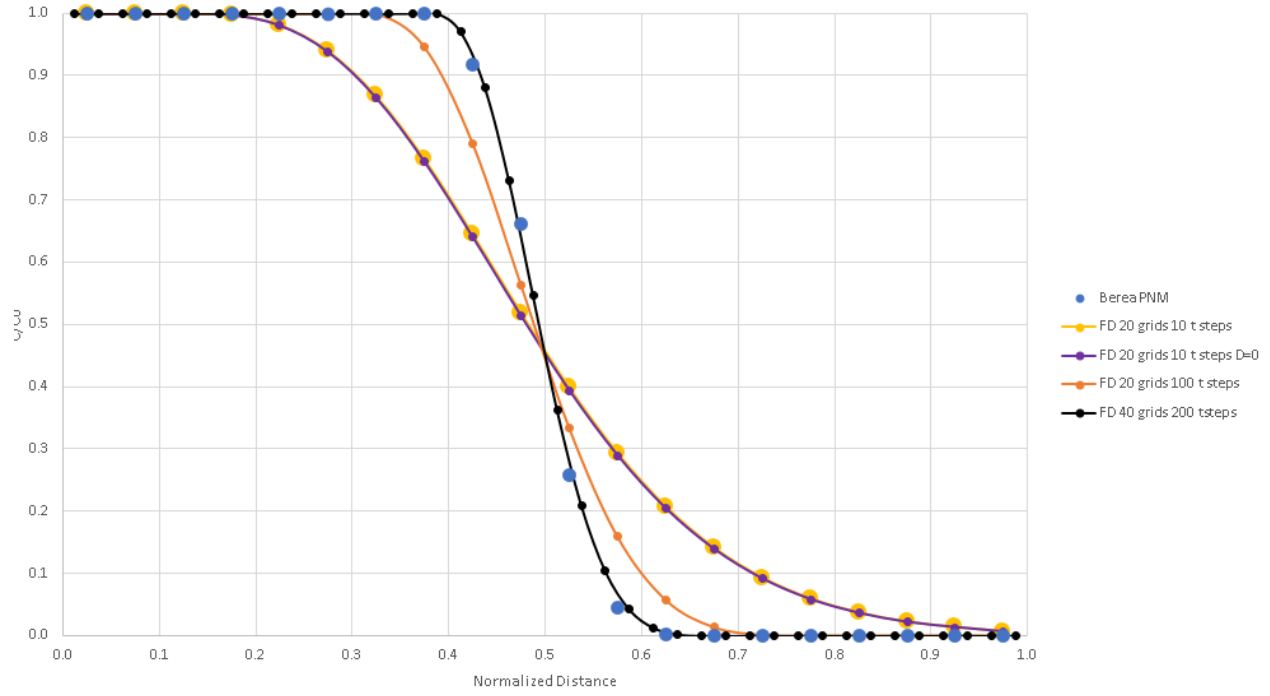


Figure 34. Concentration profiles for constant injection into 20 boundary coupled PNM at 0.5 system pore volumes with finite difference solutions (Berea PNM).

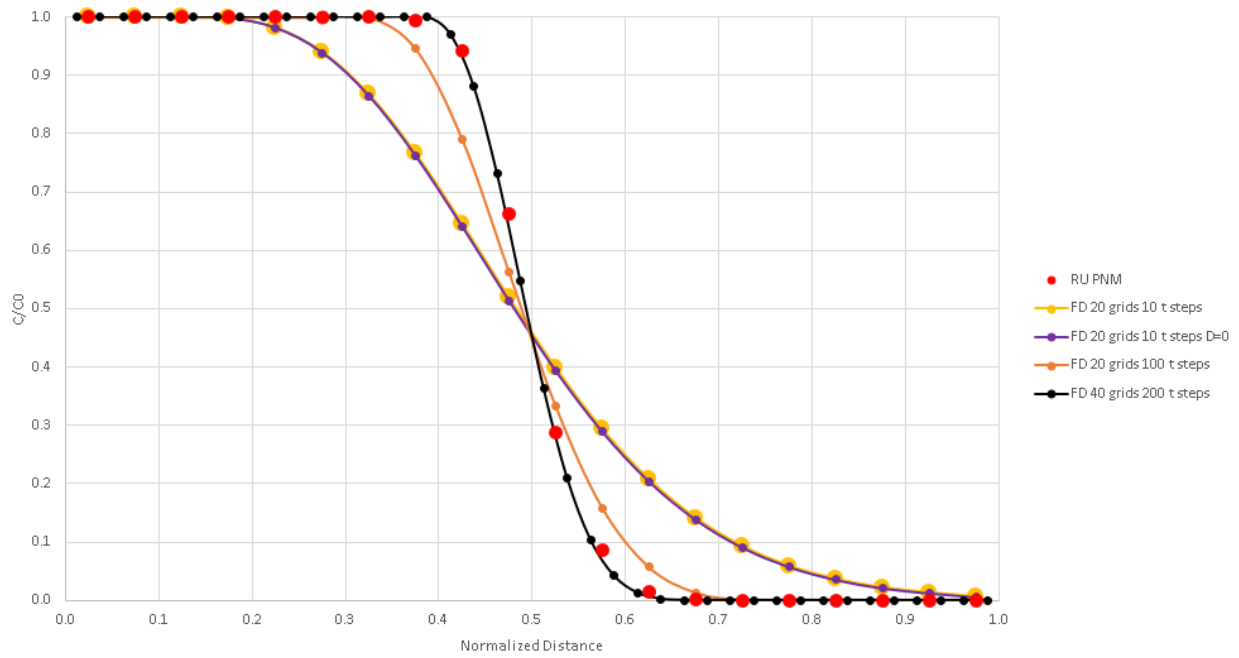


Figure 35. Concentration profiles for constant injection into 20 boundary coupled PNM at 0.5 system pore volumes with finite difference solutions (RU PNM).



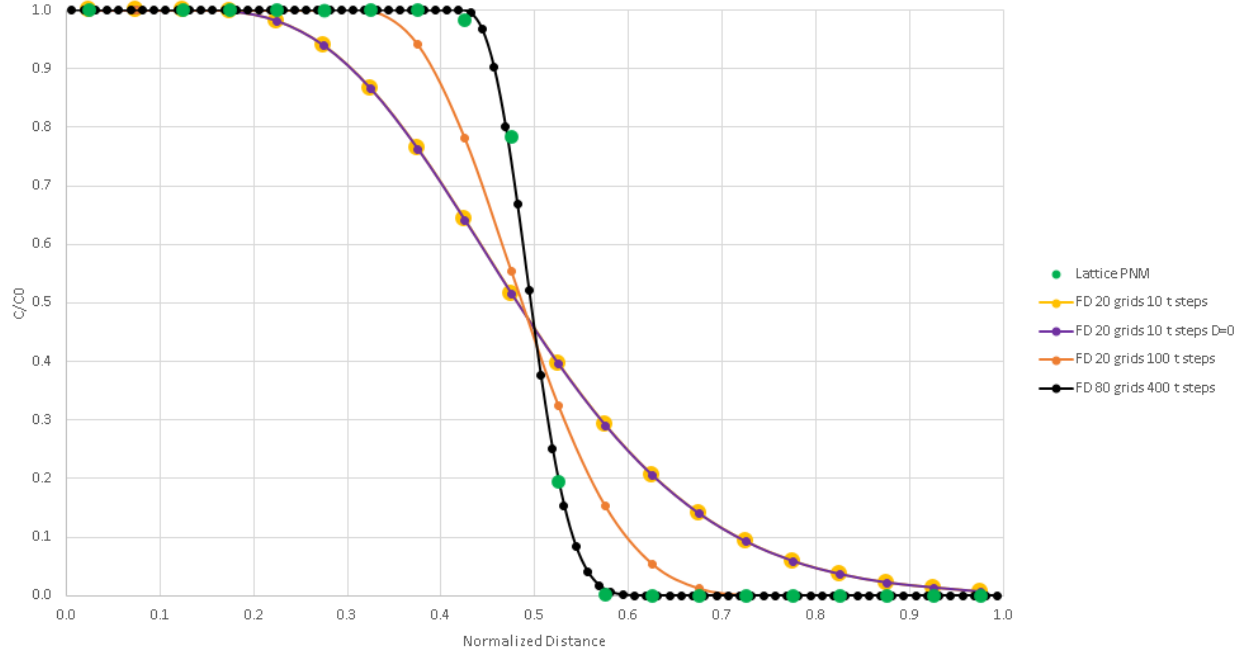


Figure 36. Concentration profiles for constant injection into 20 boundary coupled PNMs at 0.5 system pore volumes with finite difference solutions (Lattice PNM).

When 20 finite difference grid blocks and ten time steps are used in the finite difference model, numerical dispersion dominates the solution. This numerical dispersion is inherent to the finite difference model and cannot be reduced by lowering the dispersion coefficient used. This is seen in figures 34-36 where for all three cases the yellow curve, which uses the dispersion coefficients in Table 11, is nearly identical to the purple curve, which has a finite-but-near-zero value for the dispersion coefficient.

Numerical dispersion can be reduced by adding more finite difference grid blocks to the system (total system size remaining constant) or by using more time steps in the finite difference model (total simulated time remaining constant). The finite difference model approaches the boundary coupled PNM solution when numerical dispersion is sufficiently reduced. For the Berea PNM and RU PNM, 40 finite difference grid blocks and 200 time steps were sufficient to effectively eliminate numerical dispersion. The Lattice PNM required 80 finite difference grid blocks and 400 time steps. Having a more uniform velocity distribution, the Lattice PNM had less physical dispersion than the Berea PNM and RU PNM. A finer finite difference discretization is therefore required relative to the Berea PNM and RU PNM to allow physical dispersion to dominate over numerical dispersion.

The findings from the finite difference simulation comparisons indicate that a concurrently coupled system with 20 finite difference grid blocks and 20 embedded PNMs of the same size will be unable to match the 20 boundary coupled PNM solution. With that spatial discretization, the finite difference solution of the continuum-scale model exhibited excessive numerical dispersion. To overcome this limitation, it is possible to use different temporal and spatial discretizations for the continuum-scale and PNM models.

Although the size of a PNM is fixed, multiple finite-difference grid blocks can be used to represent the same amount of volumetric dimensions as a PNM in the coupled model. Each finite difference grid block within the volume of the PNM would have the same values for retention and dispersion coefficients, permeability, and porosity as the PNM. In a similar way, the finite difference time steps can be smaller than the simulated time during a PNM simulation. The finite difference grid block parameters remain constant at each small finite difference time step and are updated periodically. Increasing spatial and temporal resolutions in this way provides a means of effectively eliminating numerical dispersion for the sake of validation.

A series of simulations were performed to verify that the concurrently coupled model could replicate the boundary coupled PNM solution for the case of equal system volumes and no retention. For each PNM system (Berea, RU, and Lattice) a concurrently coupled simulation was performed in which 20 finite difference grid blocks and 100 time steps were used to simulate 0.5 pore volumes of particles injected at a constant rate. Additional simulations were performed, which used multiple finite difference grid blocks for each of the 20 PNMs in the concurrently coupled model. The multiple finite difference grid blocks representing each PNM had equivalent parameters derived from the single PNM they represented. The Berea and RU PNMs used a total of 40 finite difference grid blocks and 200 time steps in the concurrently coupled model. In comparison, the Lattice PNM used 80 finite difference grid blocks and 400 time steps. These parameters were selected as they corresponded to levels of discretization in the finite difference model, which effectively eliminated numerical dispersion in their respective PNM systems. Results from the concurrently coupled simulations as well as the boundary coupled PNM and finite-difference-only simulations are shown in Figures 37-39.

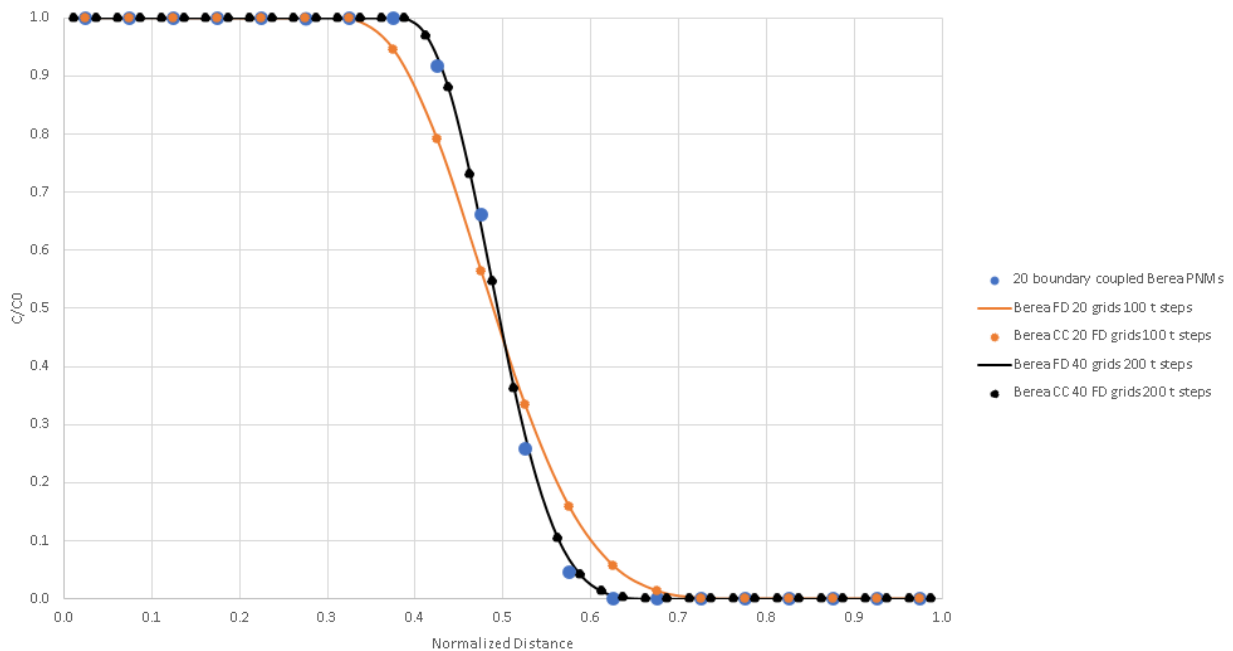


Figure 37. Concentration profiles for constant injection into 20 boundary coupled PNMs at 0.5 system pore volumes with finite difference and concurrently coupled solutions (Berea PNM).

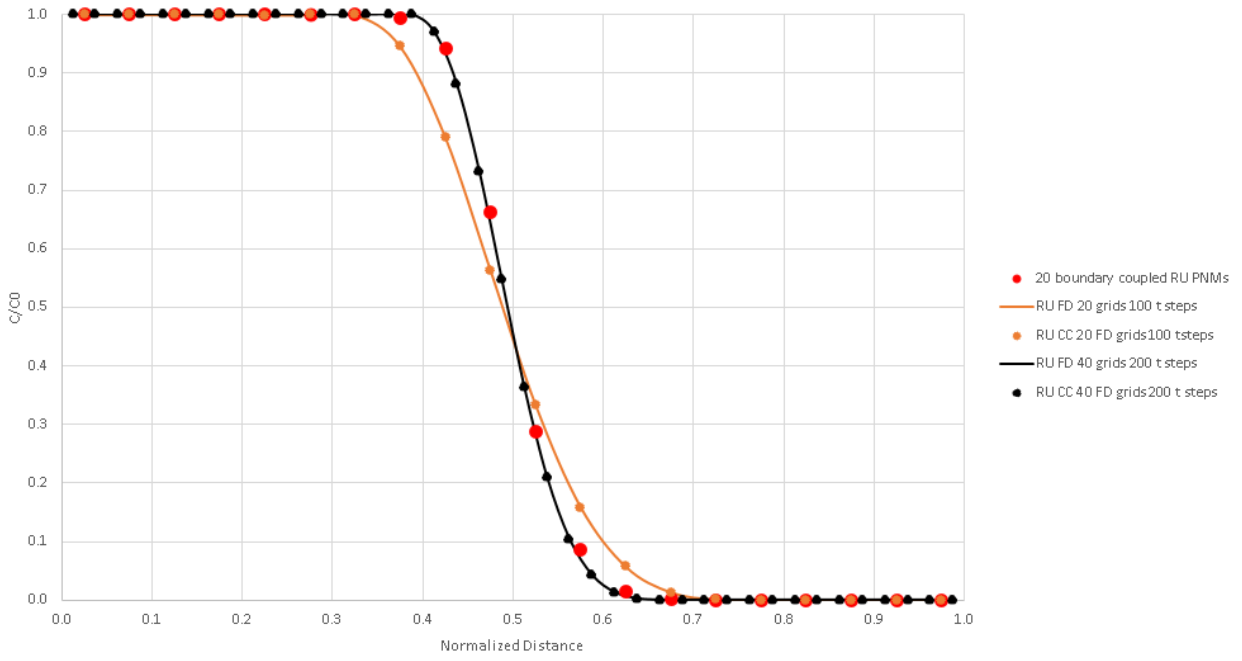


Figure 38. Concentration profiles for constant injection into 20 boundary coupled PNM at 0.5 system pore volumes with finite difference and concurrently coupled solutions (RU PNM).

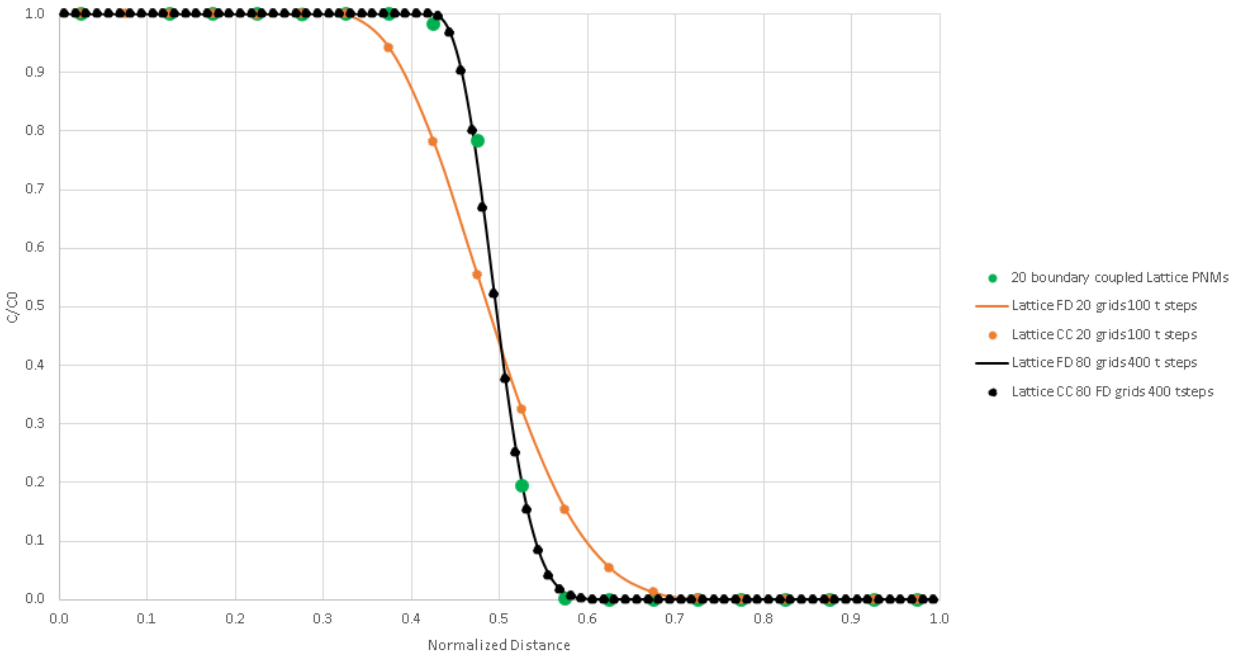


Figure 39. Concentration profiles for constant injection into 20 boundary coupled PNM at 0.5 system pore volumes with finite difference and concurrently coupled solutions (Lattice PNM).

These simulations demonstrate that, for the case of non-retaining particles, the concurrently coupled simulator can produce accurate results when the continuum-scale model occupies the same physical volume as the pore-scale model. The finite difference and concurrently coupled simulations produce identical results because the system discretizations were the same and parameter values for both were obtained from identical PNM simulations. The only difference was that the finite difference only simulations obtained the parameters from the PNMs in separate simulations, while the concurrently coupled model obtained the parameters from embedded PNMs at each simulation time step. Although this scenario was simple in that a system without retention has constant parameters, it shows that the concurrently coupled model can use boundary conditions from the continuum-scale to obtain key parameters of interest from pore-scale models, and pass these parameters back to finite difference grid blocks. Although limited in utility, because a sequentially coupled PNM and continuum-scale finite difference model could produce the same results as the concurrently coupled model, it served as a logical first step in this work.

### 3.1.2. One-Dimensional 1-to-1 Concurrent Coupling with Particle Retention

The advantage of using a concurrently coupled model becomes more evident in systems with particle retention. Systems with retention have changing parameters, such as permeability, porosity, and retention coefficient. The changes in these parameters are a complex function of particle and matrix interactions that can only be accurately measured at the pore-scale. Although experimental work can yield empirical functions of rock parameters, the accuracy of these functions is limited to the experimental conditions (particle size distributions, injection rates, etc.) used in the study. Using a concurrently coupled model allows for the measurement of changing parameters under any simulated situation. Furthermore, because physically representative PNMs can be generated for the specific system of interest, they have the potential to be more accurate than experimentally derived data, which may come from systems other than that being investigated.

A study was first performed to identify the conditions under which a 1-to-1 size concurrently coupled model would be valid. To reiterate, a 1-to-1 size concurrently coupled model is one in which the continuum-scale finite difference model occupies the same volume as the embedded PNMs. When the continuum- and pore-scale models occupy the same volume and represent the same system, the behavior of the concurrently coupled system should replicate that of a system containing only boundary coupled PNMs.

1-to-1 concurrently coupled simulations may fail to replicate boundary coupled simulations due to numerical dispersion. The boundary coupled simulations used in this study utilized a Lagrangian particle tracking method that was not impacted by numerical dispersion. However, truncation errors associated with the finite difference methods used by the concurrently coupled model caused numerical dispersion. When numerical dispersion dominates physical dispersion, simulation results become less accurate. This can occur if spatial resolutions or temporal resolutions are too coarse. Figure 40 compares analytic and finite difference concentration profiles at 0.5 system pore volumes injected for three cases with varying retention coefficients. The concentration profiles for these and all other simulations involving particle retention in this work represent only the concentration of non-trapped particles. For each simulation, 20 finite difference grid cells were used and all rock parameters remained constant throughout the simulation. The finite difference

grid cell dimensions were set equal to those of the Berea PNM. A dispersion coefficient of  $1.0 \text{ E-}3 \text{ cm}^2/\text{s}$  was used, and the 0.5 system pore volume injection time was discretized into 10 finite difference time steps (each time step equivalent to the injection of one grid cell pore volume).

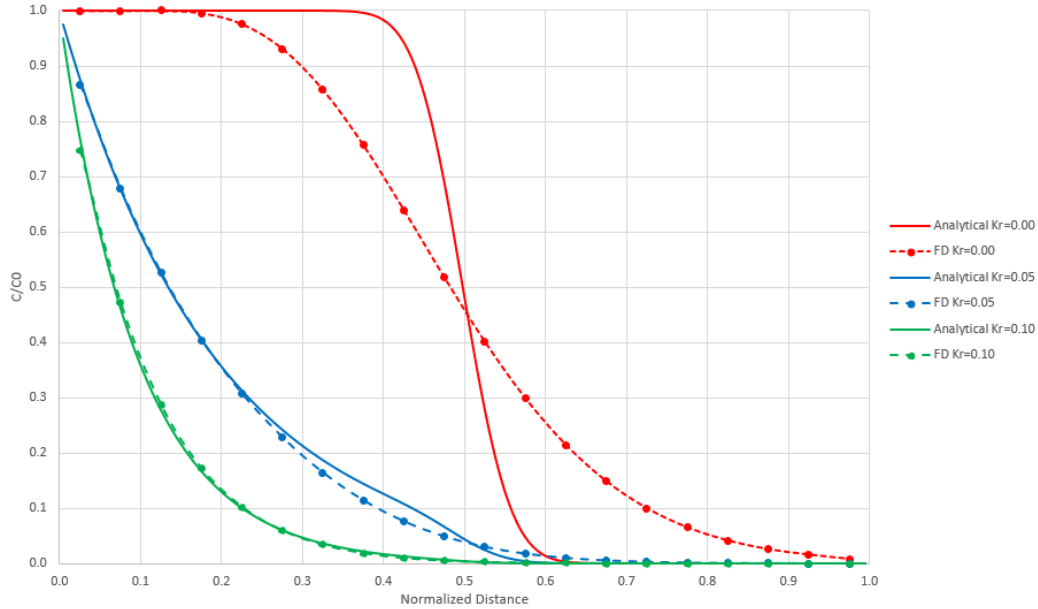


Figure 40. Analytic and finite difference concentration profiles at 0.5 system pore volumes with varying retention coefficient.

At this level of discretization (20 finite difference grid cells and 10 time steps), when no retention occurs ( $k_r = 0.00 \text{ s}^{-1}$ ), numerical dispersion causes significant error relative to the analytical solution. As  $k_r$  increases, the solution becomes dominated by the effect of retention and numerical dispersion results in less deviation from the analytical solution. Increasing the temporal resolution by adding more time steps (total simulated time held constant) reduces numerical dispersion. Figure 41 compares simulation results for the cases of  $k_r = 0.00 \text{ s}^{-1}$  and  $k_r = 0.05 \text{ s}^{-1}$  with varying numbers of time steps (10, 100, and 1,000) to analytical solutions.

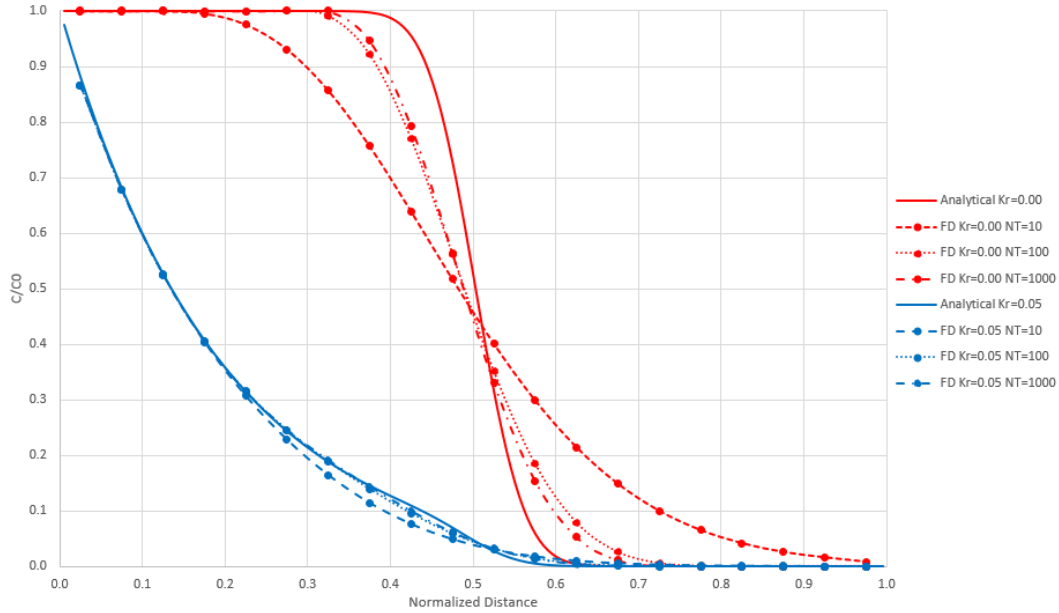


Figure 41. Analytic and finite difference concentration profiles at 0.5 system pore volumes with varying retention coefficient (varying temporal resolution).

Although numerical dispersion was reduced, it was not eliminated by increasing the temporal resolution alone. This implies that a 1-to-1 system with 20 finite difference grid cells and 20 embedded PNMs of the same size may be unable to match an analytic or boundary coupled result due to numerical dispersion. In general, concurrently coupled results will have more error due to numerical dispersion when systems have low physical dispersion and low retention.

A series of simulations were performed on the same systems of Figure 41 to investigate the impact of increasing spatial resolution on numerical dispersion. For all simulations 10 time steps were used but the number of finite difference grid blocks was varied with total system length held constant. Results for number of finite difference grids of 20, 200, and 2,000 compared to analytical solutions are summarized in Figure 42.

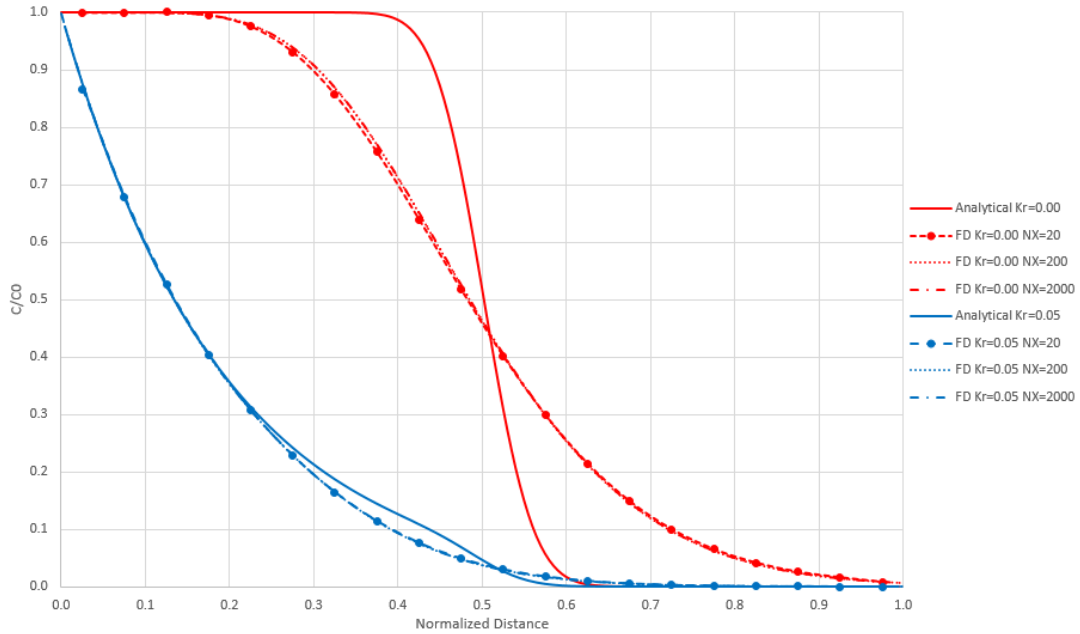


Figure 42. Analytic and finite difference concentration profiles at 0.5 system pore volumes with varying retention coefficient (varying spatial resolution).

Increasing the spatial resolution of the system had a negligible impact on numerical dispersion, which remained significant when only 10 time steps were used. Thus, simply increasing either spatial or temporal resolution alone does not ensure that numerical dispersion will be effectively eliminated.

To evaluate if the numerical dispersion inherent to the concurrently coupled model developed in this work was acceptable, a comparative simulation was performed using CMG's IMEX, a widely used commercial finite difference simulator with generally accepted numerical accuracy. The scenario chosen for the comparison was the injection of a non-trapping solute species at uniform injection concentration for 0.5 system pore volumes. The system was comprised of 20 finite difference nodes with sizes and properties equivalent to the Berea PNM. For the concurrently coupled model, given that no particles could be retained, system properties remained constant and no PNM simulations were required to update system properties. The dispersion coefficient for the solute species was set to zero so that any dispersion in the simulation would be due solely to numerical dispersion. To create an identical simulation in CMG, a solute species was created by using the SEAWATER feature. This feature allows for the injection of a non-reactive seawater species. The properties of the injected seawater were made identical to the in-situ fluid, so the seawater concentration was purely a solute species, with no impact on the rock or fluid system. The input file for the CMG simulation containing all simulation parameters can be found in Figure A1 of the Appendix. Results of the two simulations are shown in Figure 43.

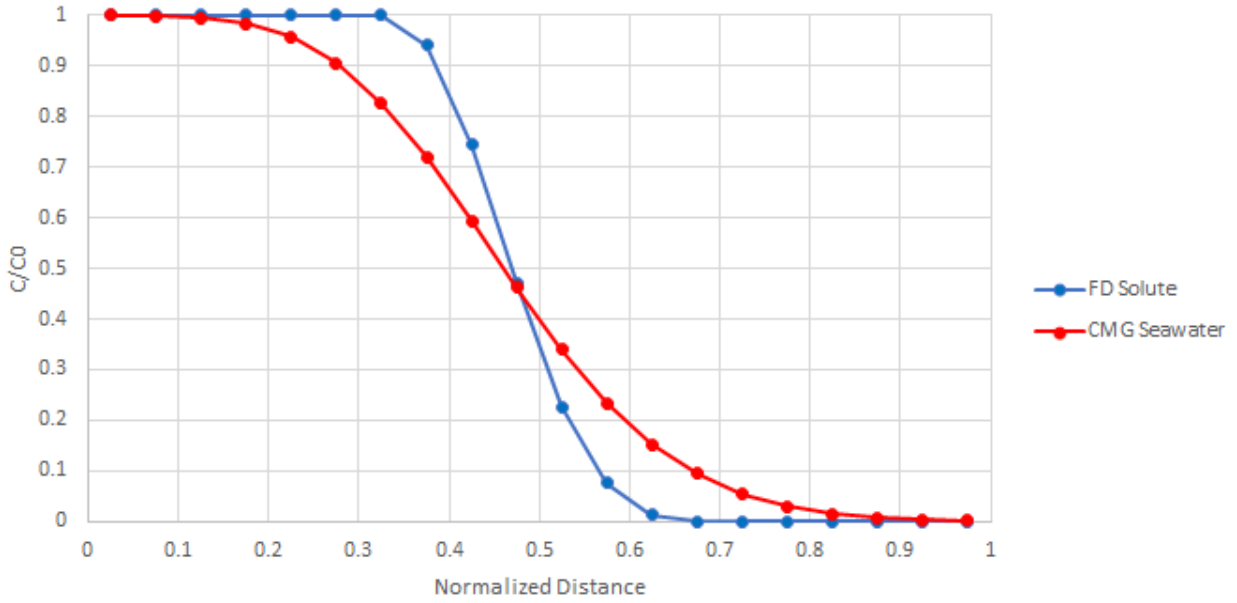


Figure 43. Comparison of numerical dispersion to commercial simulator.

The finite difference simulator used in the concurrently coupled model of this work exhibited significantly less numerical dispersion than the CMG model. The improved accuracy can be attributed to the use of the QUICK upwinding scheme applied in this work. Given that the accuracy of the finite difference model used in this work is on par with and potentially better than a widely used commercial software, the numerical dispersion of the concurrently coupled model was considered low enough given other potential sources of error, such as coefficient value accuracy.

A series of simulations were performed to confirm that numerical dispersion could be eliminated at appropriate levels of spatial and temporal resolution. Simulations were performed with increasing levels of spatial and temporal resolution (total simulated time and domain size held constant) until a resolution was found that effectively eliminated numerical dispersion. The results of these simulations are shown in Figure 44.

At sufficiently fine spatial and temporal resolutions, it was possible to effectively eliminate numerical dispersion. Although the finite difference solutions shown in Figure 44 used a relatively high resolution to eliminate numerical dispersion, acceptable accuracy was achieved with coarser resolutions. Furthermore, systems with significant levels of retention require much less resolution to eliminate numerical dispersion than systems without retention. Although updating parameters with PNM simulations may be time consuming when performed at each finite difference time step in a concurrently coupled simulation, parameter updates are only needed if a change in rock parameters has occurred.



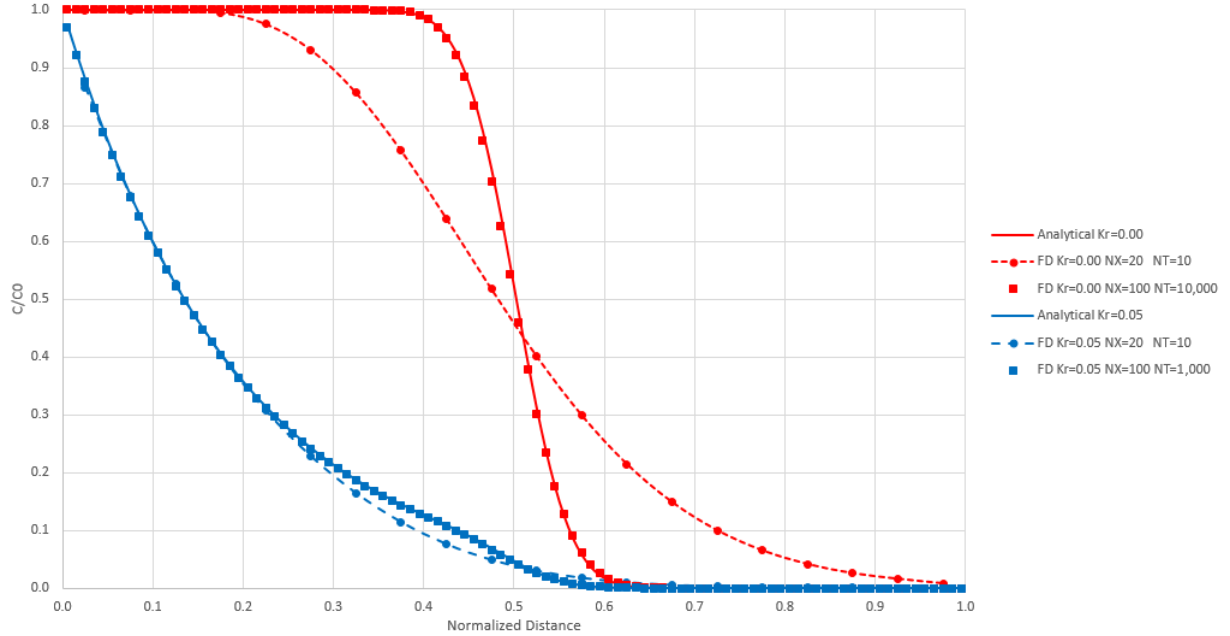


Figure 44. Analytic and finite difference concentration profiles at 0.5 system pore volumes with varying retention coefficient (numerical dispersion eliminated).

The simulation results depicted in Figure 44 required spatial resolutions smaller than the length of a single Berea PNM to reduce numerical dispersion. However, the ultimate goal of this work was to simulate conditions in which the spatial resolution of the finite difference model was much larger than the size of the embedded PNMs. As an intermediate step to this ultimate goal, a series of simulations were performed to identify a 1-to-1 concurrently coupled system which had finite difference grid cells equal in volume to their embedded PNMs, with low numerical dispersion. From Figure 41 it can be seen that if there is no retention, a system of 20 finite difference grid cells equal in size to the Berea PNM will exhibit significant numerical dispersion, even with very high temporal resolutions. Simulations were performed in which the number of finite difference grid cells was increased (grid cell size remaining constant) until numerical dispersion could be effectively eliminated with a reasonable temporal resolution. Results for  $k_r = 0.00 \text{ s}^{-1}$  and  $k_r = 0.05 \text{ s}^{-1}$  are shown in Figures 45 and 46 respectively.

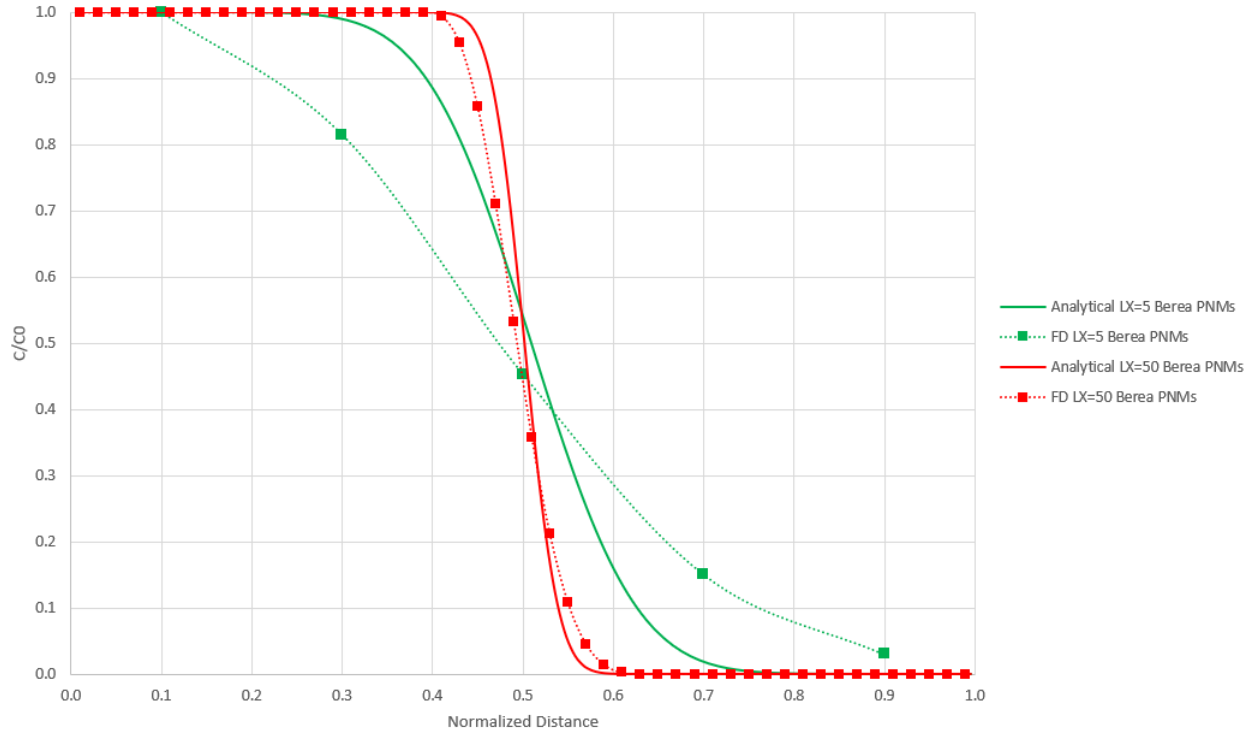


Figure 45. Analytic and finite difference concentration profiles at 0.5 system pore volumes for finite difference grid sizes equal to Berea PNM dimensions ( $k_r = 0.00 \text{ s}^{-1}$ ).

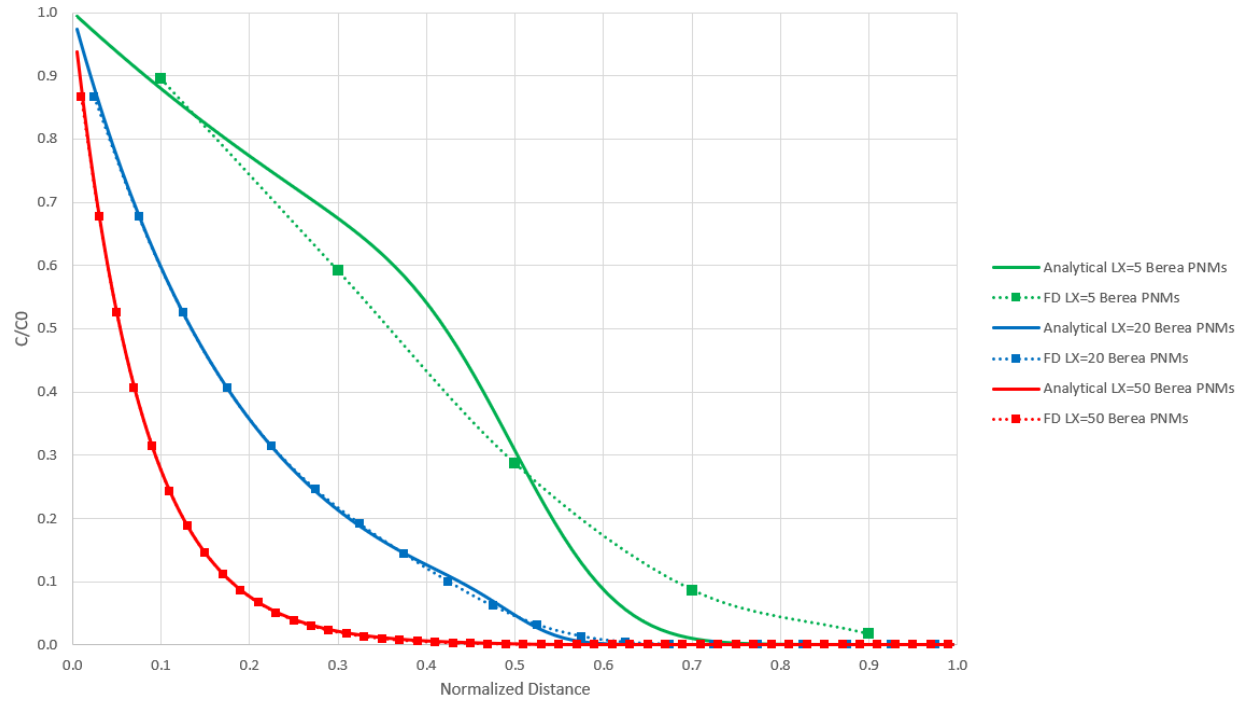


Figure 46. Analytic and finite difference concentration profiles at 0.5 system pore volumes for finite difference grid sizes equal to Berea PNM dimensions ( $k_r = 0.05 \text{ s}^{-1}$ ).

When  $k_r = 0.00 \text{ s}^{-1}$  and each finite difference grid was equivalent in size to a single Berea PNM, increasing the number of finite difference grids alone could not eliminate numerical dispersion. Although adding more finite difference grids reduced the effect of numerical dispersion, the system length increased. A longer system length resulted in a sharper concentration front. In practice, with a finite difference model, a sharper concentration front is more difficult to replicate than a relatively more spread-out front because sharper fronts are more impacted by numerical dispersion. Effectively this meant that the finite difference model, although second order accurate, could not model without error a system with finite difference grid blocks of the same size and dispersion coefficient as the Berea PNM, when  $k_r = 0.00 \text{ s}^{-1}$ . Thus, the concurrently coupled model would not be capable of producing error free predictions of concentration profiles under such 1-to-1 model conditions. However, as shown in Figure 44, error free predictions could be made if each embedded PNM was represented by multiple finite difference grid blocks. Alternatively, it can be inferred that error free results could also be obtained if the Berea PNM was smaller in size. In practice however, smaller PNMs are unsuitable as they contain fewer pores and tend to be less representative of the true porous media compared to larger PNMs.

If retention is present, it is possible for numerical dispersion to be eliminated when each finite difference grid is equivalent in size to a single Berea PNM. As can be seen in Figure 46, as the number of finite difference grid cells was increased, numerical dispersion caused less and less error. This research primarily considered cases where retention was non-zero. Thus, it was possible to perform accurate modeling when the concurrently coupled model had finite difference grid blocks that were the same size as their embedded PNMs. As particle trapping progresses however, retention coefficients decrease. As retention coefficients decrease, numerical dispersion becomes more dominant. Therefore, it was difficult to know a priori if an accurate simulation was possible for a given 1-to-1 concurrently coupled system.

Simulations were performed to identify a situation with changing retention coefficient that could be accurately modeled by a 1-to-1 concurrently coupled system with finite difference grids equivalent in size to a single Berea PNM. A particle size of 10 microns was chosen for influent damaging particles as this particle size became trapped in significant numbers in the Berea PNM. Initially, the effect of 10-micron particle trapping on retention and dispersion coefficients for the Berea PNM was investigated. Figures 47 and 48 demonstrate how these parameter values changed as a function of the number of 10-micron particles trapped in a single Berea PNM.

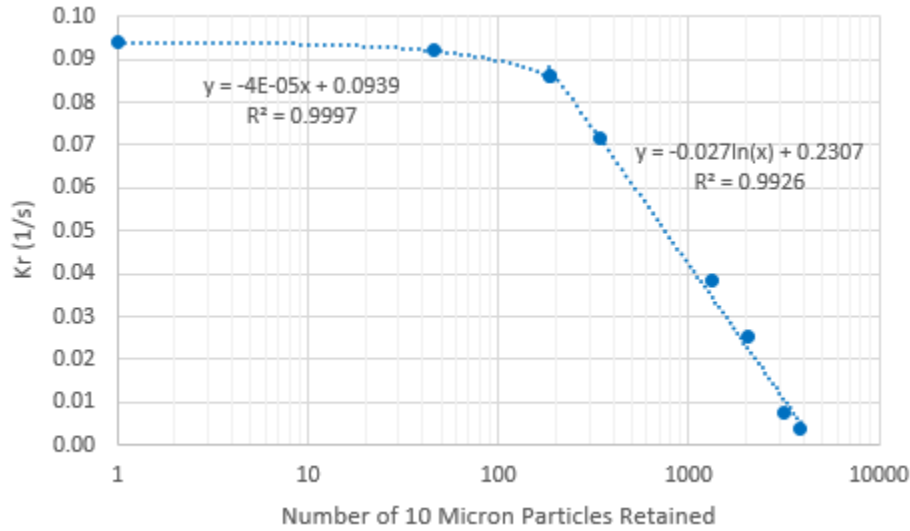


Figure 47. Retention coefficient vs number of 10-micron particles retained in a single Berea PNM.

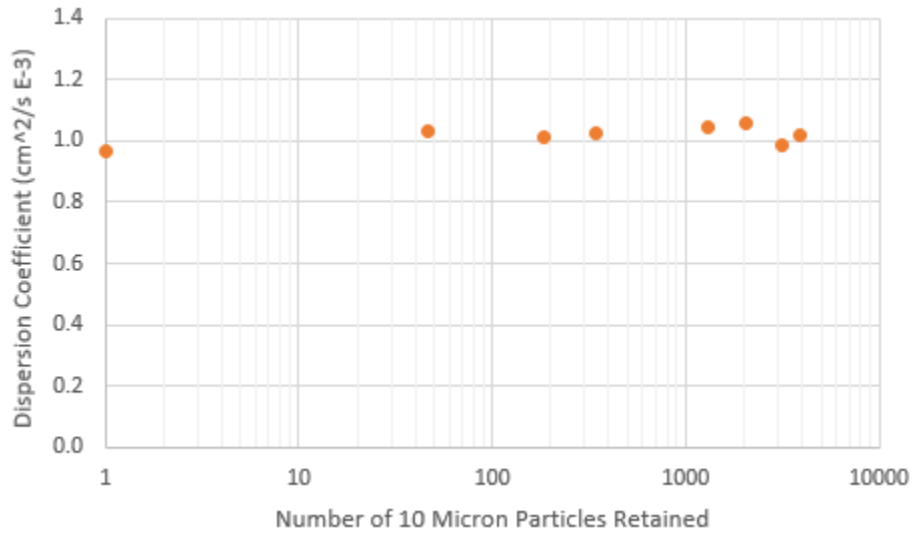


Figure 48. Dispersion coefficient vs number of 10-micron particles retained in a single Berea PNM.

For this particular PNM, at relatively small numbers of 10-micron particles retained (less than about 200), retention coefficient decreased approximately linearly. Once the number of 10-micron particles retained exceeds about 200 however, the retention coefficient decreased in a non-linear fashion and could be approximated with a good degree of accuracy using a logarithmic model. Dispersion coefficient in the Berea PNM was far less impacted by the retention of 10-micron particles. Although its value fluctuated around an average of  $1.02 \text{ E-3 cm}^2/s$ , its minimum and maximum value differed by less than 10% for the case of 10-micron particles. Thus, for practical

purposes the dispersion coefficient of the Berea PNM was independent of the degree of 10-micron particle trapping.

As an intermediate step towards running a 1-to-1 concurrently coupled model with PNMs, simulations were performed that used a piecewise empirical equation to periodically update retention coefficient in the case of 10-micron particle injection. Use of an empirical equation for retention coefficient, although not possible in general, was faster than using a PNM simulation. This aided in rapid testing of the concurrently coupled model. The piecewise empirical equation used was obtained by replotting Figure 47 with number of particles injected as the independent variable, rather than number of particles retained. The replotted version of Figure 47 is shown in Figure 49.

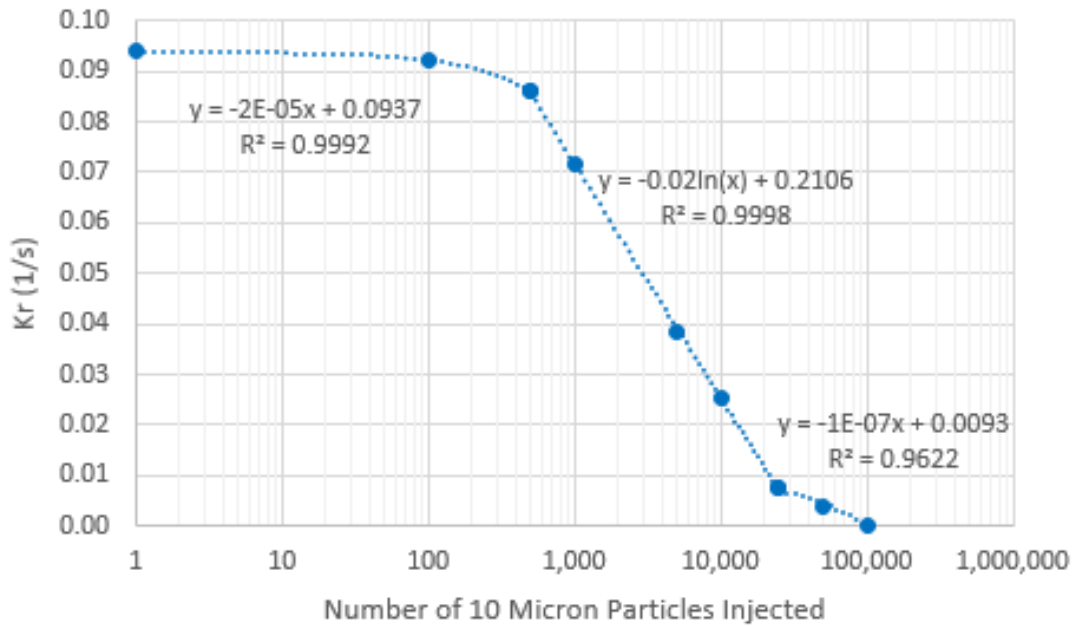


Figure 49. Retention coefficient vs number of 10-micron particles injected into a single Berea PNM.

The resulting piecewise empirical equation can be written as

$$k_r = \begin{cases} -2E-5N_p + 0.0937 & \text{if } N_p \leq 500 \\ -0.02 \ln(N_p) + 0.2106 & \text{if } 500 \leq N_p \leq 25,000 \\ -1E-7N_p + 0.0093 & \text{if } N_p > 25,000 \end{cases} \quad (42)$$

where  $N_p$  represents number of particles injected into a given PNM. When using Equation 42, a minimum value of zero was used as a lower limit for values of  $N_p$  larger than 100,000. Number of particles injected was used as the independent variable as it is simpler to predict than number of particles retained in a PNM.

Regardless of whether a PNM simulation or an empirical function was used to obtain grid block properties, a formulation was required to determine  $N_p$ . For a given grid cell  $j$  and time step length  $\Delta t$ ,  $N_p$  (number of particles entering an embedded PNM) can be evaluated as

$$N_{p,j} = C_{j-\ell_{PNM}/2} Q \Delta t \quad (43)$$

where  $Q$  represents volumetric flow rate into the PNM and  $C_{j-\ell_{PNM}/2}$  (units of number of particles per volume) represents particle concentration in block  $j$  evaluated at the upwind face of the embedded PNM. It is important to note that  $N_p$  is defined as the number of particles that enter the PNM, not the grid block. Various methods are available for evaluating  $C_{j-\ell_{PNM}/2}$  and linear interpolation between  $C_j$  and  $C_{j-1}$  was used, the accuracy of which was sufficient for the purpose of this work. If the embedded PNM and finite difference grid blocks are the same size, then they share the same face location and the number of particles entering the grid block is the same as that entering the PNM. In this scenario equation 43 becomes

$$N_{p,j} = \frac{C_j + C_{j-1}}{2} Q \Delta t \quad (44)$$

However, if the embedded PNM is smaller than the finite difference grid block, the number of particles entering the PNM may be significantly different than the number of particles entering the finite difference grid block over any given time step. Failure to evaluate  $N_{p,j}$  using the upwind PNM face concentration can result in significant error, as Section 3.1.5. will demonstrate.

Importantly, before a given time step, all grid block parameters should be determined and these parameters remain constant during the time step. If parameter values change over the course of a time step, then use of a set of parameters that was valid only at the beginning of a time step can lead to error. For example, particle retention may result in a lower value of retention coefficient at the end of a time step compared to the beginning. Thus, applying the initial larger retention coefficient value over that finite difference time step would lead to a predicted concentration value in the grid block that would be too low. Similarly, if the finite difference model used the retention coefficient value at the end of the time step, the predicted concentration value in the grid block would be higher than the true value. Thus, it is better to evaluate parameter values at an intermediate time between the beginning and end of a time step, and apply these intermediate values over the duration of the time step. For this reason, this work used a value of  $N_p$  evaluated at a time halfway between the beginning and end of the time step to determine grid block parameter values. This intermediate value of  $N_p$ , called  $N_{pi}$  in this work, can be evaluated for a given grid cell  $j$  at a given time step  $n$  as

$$N_{pi,j} = \frac{1}{2} \left( \sum_{t=0}^n N_{p,j} + \sum_{t=0}^{n+1} N_{p,j} \right) - \sum_{t=0}^{n-1} N_{pi,j} \quad (44)$$

where the term in parentheses represents the cumulative number of particles injected half way between the current and next time step, and the rightmost term represents the cumulative number of particles previously injected into the grid cell.

As a basis of comparison for the concurrently coupled models, concentration profiles were generated after 0.5 system pore volumes of injection of 10-micron-diameter particles into various boundary coupled Berea PNM systems. The first set of simulations considered a total of 50,000 particles injected into 10, 20, and 40 boundary coupled Berea PNMs. For all cases, the particles were injected at a constant rate and concentration over the 0.5 system pore volume period. The concentration profiles for these simulations are shown in Figure 50.

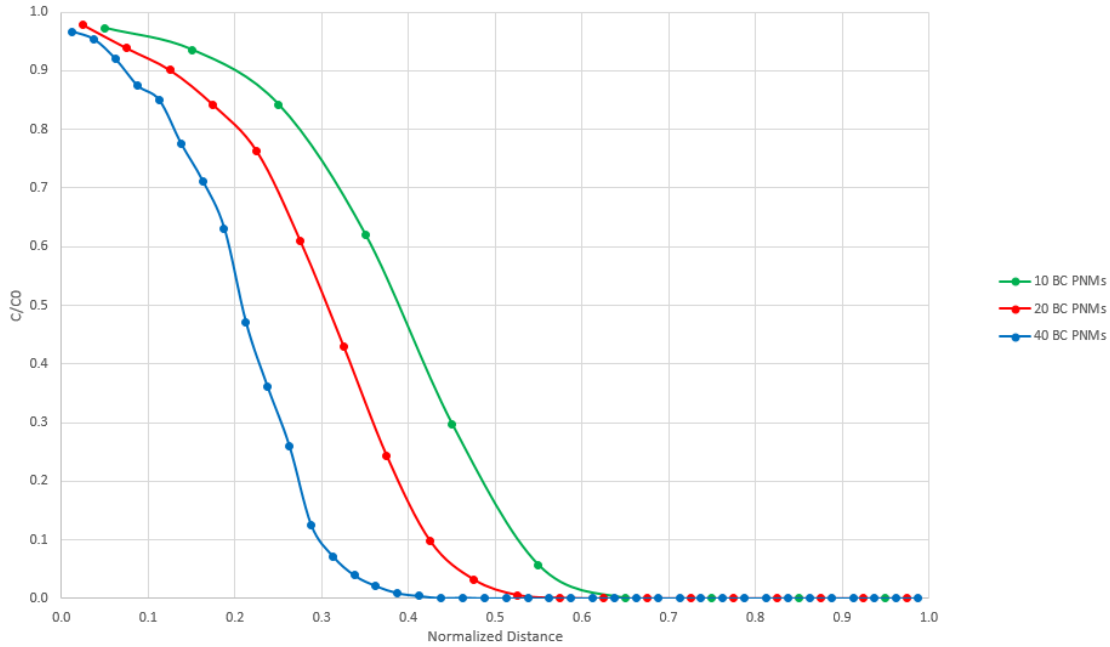


Figure 50. Concentration profiles for injection of 50,000 10-micron particles into 10, 20, and 40 boundary coupled Berea PNMs at 0.5 system pore volumes.

It is important to note that concentration values in a given PNM should be evaluated using effective rather than bulk pore volumes. In this work effective pore volume was calculated by summing the pore volume of all pores which had non-zero inlet and outlet flow rates. The concentration within a given PNM,  $C_{PNM}$ , normalized to inlet concentration,  $C_0$ , was determined as

$$C_0 = \frac{\text{Total Number of Injected Particles}}{\text{Total PV Injected [cm}^3\text{]}} \quad (45)$$

$$C_{PNM} = \frac{\text{Number of particles in PNM}}{\text{Effective PNM Pore Volume [cm}^3\text{]}} \quad (46)$$

$$\frac{C_{PNM}}{C_0} = \frac{\text{Number of particles in PNM}}{\text{Effective PNM Pore Volume [cm}^3\text{]}} \frac{\text{Total PV Injected [cm}^3\text{]}}{\text{Total Number of Injected Particles}} \quad (47)$$

As particles become retained, throat conductance values can become zero resulting in pores that do not contribute to fluid flow in the system. These no flow pores contribute to bulk porosity but

not effective porosity. As more particle retention occurs, effective porosity decreases. If this effect is not taken into account and bulk porosity is used to determine particle concentration values inside a given PNM, the result will be artificially low values of grid block concentration.

To illustrate this point, solute flow simulations were run on two boundary coupled systems of 10 Berea PNMs. The first simulation used non-damaged Berea PNMs and the second simulation involved Berea PNMs that had been damaged by a random mix of 100,000 10-micron-diameter particles and 100,000 13-micron-diameter particles. In each simulation 10,000 solute particles were injected over 0.8 system pore volumes. PNM concentration values in the two simulations were evaluated using both bulk and effective porosity as the basis for PNM pore volume when determining solute concentration values. Table 12 contains bulk and effective porosity values for the two PNMs.

Table 12: Bulk and effective porosity values for undamaged and damaged Berea PNMs.

<b>PNM</b>	<b>Porosity Type</b>	<b>Porosity</b>	<b>Effective/Bulk Porosity</b>
Undamaged Berea	Bulk	0.152	1.0
Damaged Berea	Bulk	0.152	1.0
Undamaged Berea	Effective	0.149	0.98
Damaged Berea	Effective	0.142	0.93

Both the undamaged and damaged Berea PNMs have the same bulk porosity. In the undamaged PNM about 2% of pores do not contribute to flow resulting in an effective porosity value about 98% of the bulk porosity. Injection and retention of particles into the undamaged Berea PNM resulted in reducing the effective porosity to about 93% of bulk porosity. Concentration profile results from the two simulations are displayed in Figures 51 and 52.



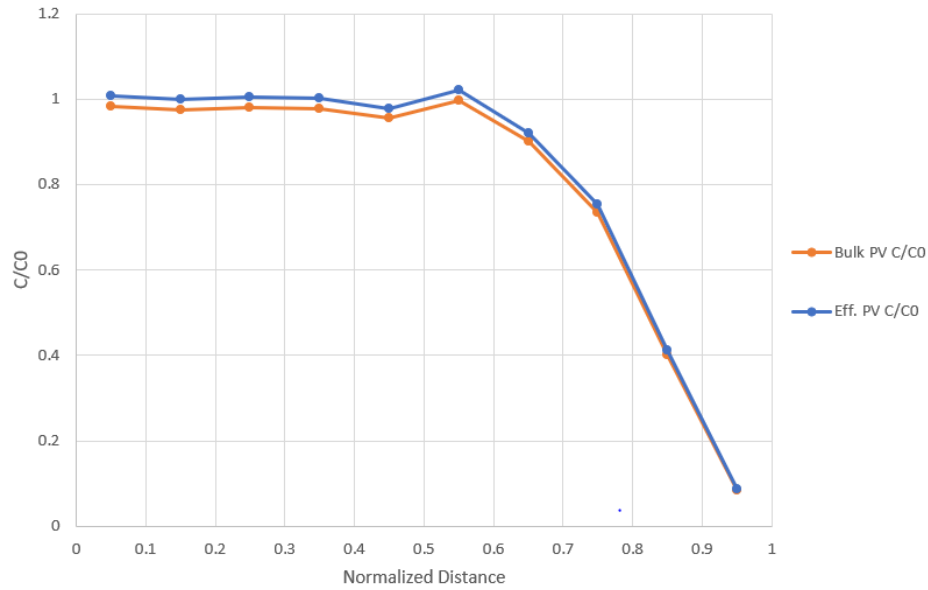


Figure 51. Solute concentration profile comparison: undamaged Berea PNMs.

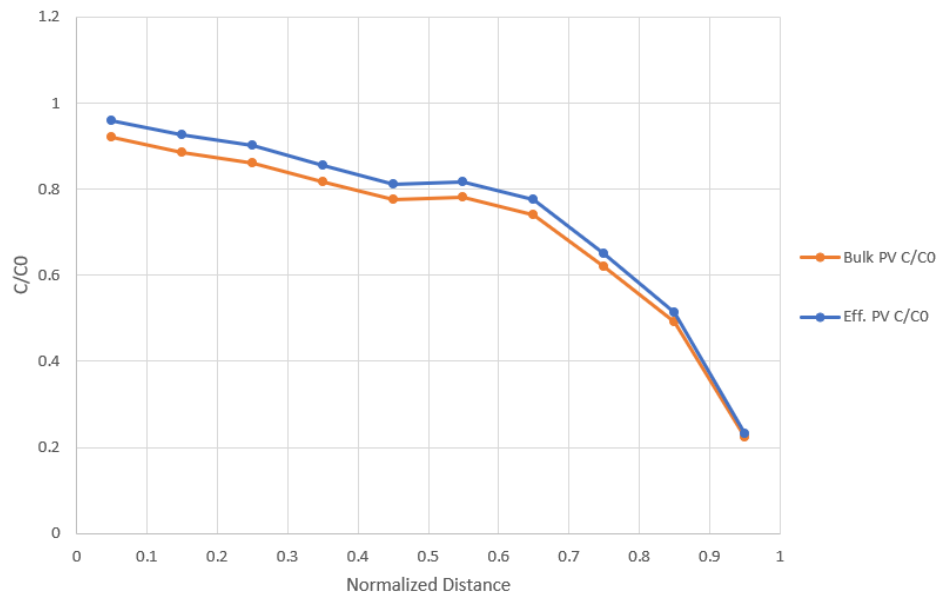


Figure 52. Solute concentration profile comparison: damaged Berea PNMs.

In the undamaged system there was little difference in bulk and effective porosity, which corresponded to little difference in the concentration profiles calculated by both methods. On the other hand, in the damaged system the concentration profile as evaluated using bulk porosity was noticeably lower than that evaluated using effective porosity. Extrapolating the concentration curves to the inlet, the value corresponding to the effective porosity formulation trended towards 1.0, while that determined by bulk porosity trended to below 1.0 (about 0.95). Given that the inlet concentration should be 1.0, it can be inferred that effective porosity is the proper porosity to use when evaluating PNM concentration values. If bulk porosity were used to determine PNM

concentrations, boundary coupled simulations with significant amounts of retained particles and relatively lower effective porosities would have artificially low concentration values. This would lead to artificial discrepancies between concurrently coupled simulations and boundary coupled simulations with identical input parameters.

1-to-1 concurrently coupled simulations were performed and compared to the boundary coupled results of Figure 50. The results of these simulations, shown in Figure 53, used the piecewise empirical formula of Equation 42 to evaluate  $k_r$ . For each system size, one concurrently coupled simulation was performed in which the finite difference grid cells had the same size as a Berea PNM, and a second concurrently coupled simulation was performed with an order-of-magnitude higher spatial resolution.

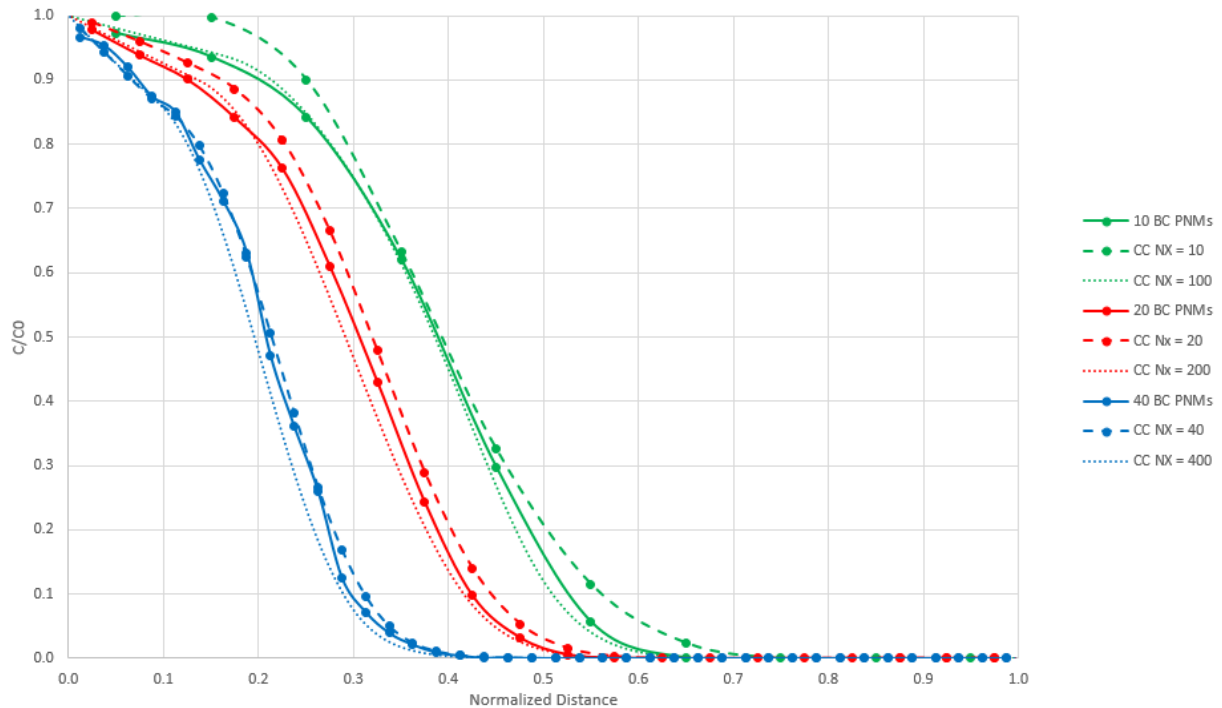


Figure 53. Comparison of concentration profiles for injection of 50,000 10-micron particles into 10, 20, and 40 boundary coupled Berea PNMs at 0.5 system pore volumes with concurrently coupled simulations (empirical formulation for  $k_r$ ).

The higher spatial resolution simulations had resolutions fine enough to effectively eliminate numerical dispersion. Therefore, the spread between the high resolution and low resolution concurrently coupled simulations was purely due to numerical dispersion. With 10 finite difference grid cells, numerical dispersion was significant and caused the concurrently coupled model to differ significantly from the high resolution and boundary coupled cases. As the number of finite difference grid cells increased, the difference between the high and low resolution concurrently coupled simulations decreased. Despite the effects of numerical dispersion, concurrently coupled simulation results produced good qualitative matches for the cases of 20 and 40 boundary coupled PNMs. As long as the error associated with using an empirical formulation for  $k_r$  is small, a

concurrently coupled model using PNM's rather than the empirical formulation should also result in good matches with boundary coupled simulations.

For completeness, simulations were performed which were identical to those shown in Figure 53, with a total number of particles injected of 25,000 and 10,000 rather than 50,000. The results of these simulations are shown in Figures 54 and 55. Simulations for 10 boundary coupled PNM's were omitted due to the previously observed significant impact of numerical dispersion with only 10 finite difference grid cells.

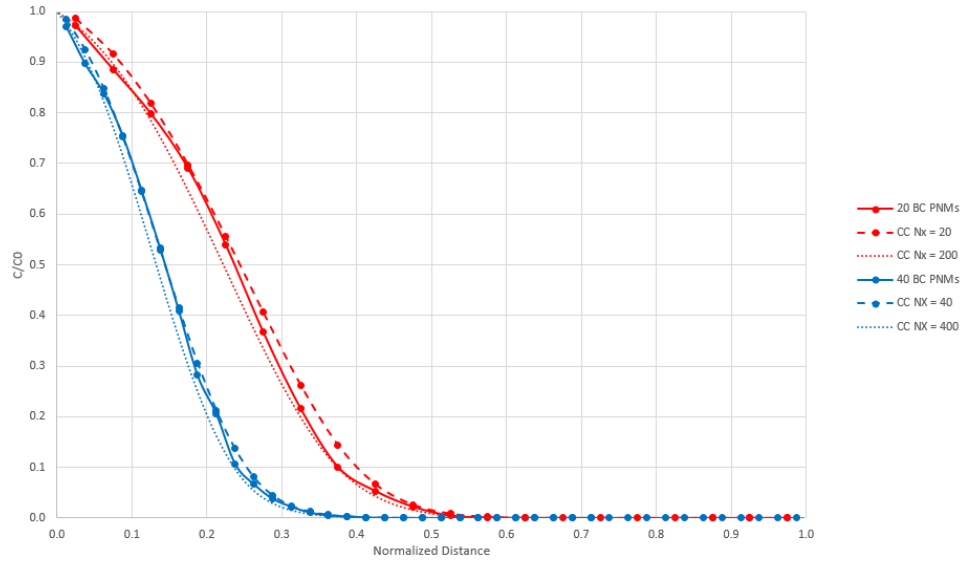


Figure 54. Comparison of concentration profiles for injection of 25,000 10-micron particles into 20 and 40 boundary coupled Berea PNM's at 0.5 system pore volumes with concurrently coupled simulations (empirical formulation for  $k_r$ ).

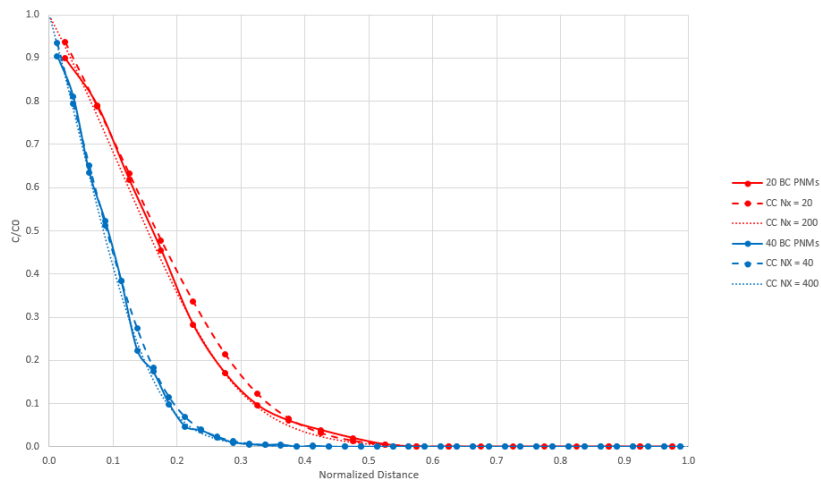


Figure 55. Comparison of concentration profiles for injection of 10,000 10-micron particles into 20 and 40 boundary coupled Berea PNM's at 0.5 system pore volumes with concurrently coupled simulations (empirical formulation for  $k_r$ ).

As was the case for 50,000 particles, concurrently coupled simulations using finite difference grid cells the same size as the Berea PNM and Equation 42 for  $k_r$  were able to produce good qualitative matches with boundary coupled simulations for 25,000 and 10,000 10-micron particles injected.

Simulations were performed to confirm that the concurrently coupled model using PNMs to update coefficient values rather than the empirical formulation of Equation 42 could accurately match boundary coupled simulation results. 1-to-1 concurrently coupled simulations using PNMs were performed for a system size of 20 Berea PNMs and total number of 10-micron particles injected of 50,000, 25,000, and 10,000. Results are summarized in Figure 56.

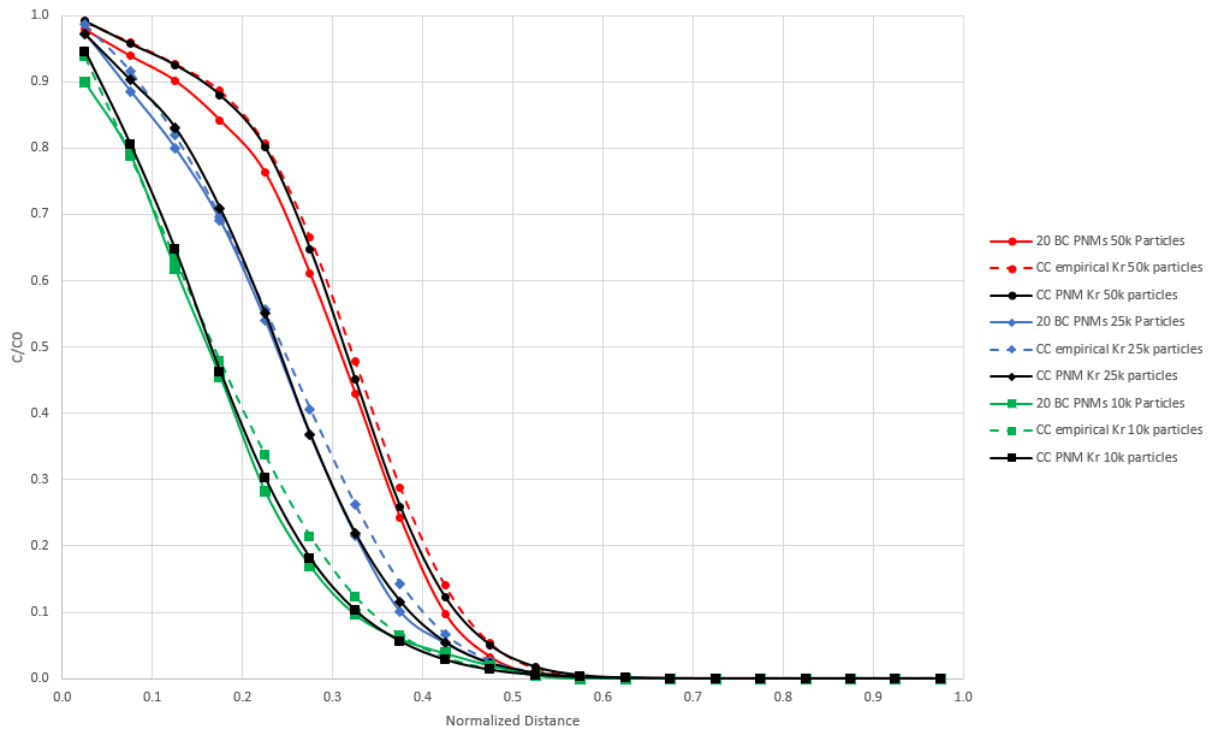


Figure 56. Comparison of concentration profiles for injection of 10-micron particles into 20 boundary coupled Berea PNMs at 0.5 system pore volumes with concurrently coupled simulations.

The concurrently coupled simulations using PNMs to evaluate  $k_r$  were able to replicate the boundary coupled PNM simulation results with a high degree of accuracy. Discrepancies between the concurrently coupled simulations using PNMs and the boundary coupled results can be attributed to numerical dispersion. Evidence of this discrepancy can be inferred from Figure 56 as concurrently coupled simulations with fewer particles injected more closely reproduced the boundary coupled results. When fewer particles were injected, fewer particles damage the system and retention coefficients remained larger. Larger retention coefficients correspond to solutions more dominated by retention and less influenced by numerical dispersion. Also, when relatively large numbers of particles were injected and retained (as in the case of 50,000 particles injected) retention coefficients were reduced to almost zero and numerical dispersion caused additional

error. Discrepancies between the concurrently coupled simulations using PNMs and those using the empirical formulation to calculate  $k_r$  can be attributed to error in the empirical formulation.

The results of Figure 56 demonstrate that a concurrently coupled model can use embedded PNMs to accurately evaluate grid block properties and simulate particle transport and retention. Particle retention in those simulations caused grid block properties to vary significantly in time and space. An analytic solution or finite difference model with constant parameters would have been unable to reproduce the boundary coupled results. Although, as was demonstrated, accurate finite difference simulation results can be obtained when empirical formulations are used to evaluate grid block properties, these formulations are time consuming to produce, not entirely accurate, and most importantly are limited by the precise set of conditions used in their creation.

It is important to note that the single coefficient retention model of Equation 3 governs particle transport and retention in the concurrently coupled model. Although previous experimental work has shown this model to be deficient in scenarios in which size exclusion is the dominant mechanism for retention, it provided accurate results in the 1-to-1 scenario. The improved accuracy of the model can be attributed to the use of PNM simulations to periodically update the retention coefficient in each finite difference grid block. Thus, the concurrently coupled model was able to accurately simulate particle transport and retention in a straining dominated scenario without the use of additional empirical parameters needed for alternate models, such as those of Tufenkji and Elimelech (2004) and Porubcan and Xu (2010). This demonstrates the potential for concurrent coupling to provide a flexible and simple means of simulating particle transport and retention.

### 3.1.3. One-Dimensional 3-to-1 Concurrent Coupling – Single Particle Size

Having demonstrated the accuracy of the 1-to-1 concurrently coupled model, the next stage of model development focused on scenarios where the underlying PNMs were smaller than their embedded grid blocks. For the concurrently coupled model to be useful for practical situations, the embedded PNMs ultimately have to be significantly smaller than the finite difference grid blocks. As discussed previously, PNMs are typically on the order of centimeters in length while finite difference grid blocks in most systems of interest are on the order of meters. A series of simulations were conducted to investigate the challenges and accuracy of concurrently coupled models with such large size discrepancies.

As an intermediate step to simulating particle transport and retention in a concurrently coupled system with order-of-magnitude differences in size between embedded PNMs and finite difference grid blocks, a series of simulations were performed with small differences in size between the pore- and continuum-scale models. The first system chosen was one-dimensional and contained 10 finite difference grid cells. Each grid cell had a PNM embedded in its center, with the length of the PNM in the direction of flow being one-third that of the grid cell. Dimensions of the PNM in non-flow directions were equivalent to the finite difference grid cells. Given the three-to-one size ratio of grid cells to PNMs, this system will be referred to as a 3-to-1 system. A single grid cell and embedded PNM for the 3-to-1 concurrently coupled system is depicted in Figure 57.

Before running concurrently coupled simulations on the 3-to-1 system, a baseline was obtained by running a boundary coupled simulation of 30 Berea PNMs (equivalent system size to the 3-to-1

system described in the paragraph above). The boundary coupled model tracks the pore-to-pore transit of every particle and so produces reliable concentration profiles to evaluate the accuracy of the concurrently coupled model. For the boundary coupled baseline simulation, 25,000 10-micron-diameter particles were injected over 0.5 pore volumes with a constant inlet velocity of 0.01 cm/s. Fluid viscosity was held constant at 1 cp. The concentration profile of the particles in the boundary coupled system is shown in Figure 58.

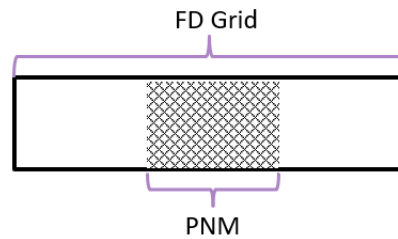


Figure 57. Illustration of a 3-to-1 concurrently coupled PNM and finite difference grid cell.

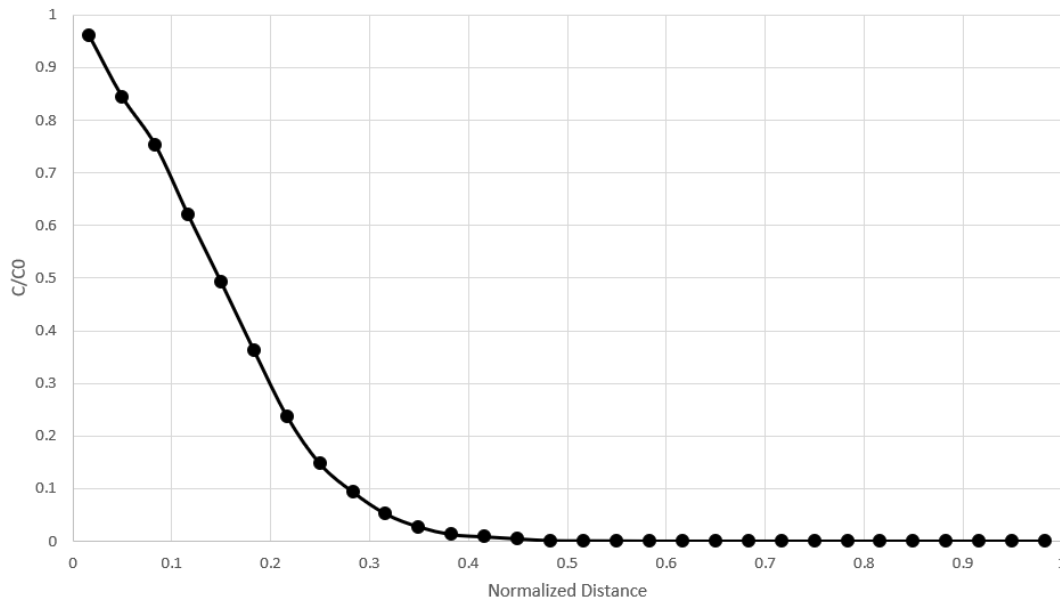


Figure 58. Concentration profile for 30 boundary coupled PNM baseline simulation.

With a baseline for comparison established, the 3-to-1 boundary coupled system was simulated. A constant inlet boundary concentration, constant inlet flow velocity of 0.01 cm/s, and constant fluid viscosity of 1 cp were used. The 3-to-1 system was comprised of 10 finite difference grid blocks each with an embedded PNM as depicted in Figure 57, thus making the concurrently coupled system equivalent in size to the boundary coupled system. Grid block properties were initialized according to the Berea PNM properties in Table 1 and were updated before each of the 100 time steps in the simulation. Figure 59 compares the concentration profile generated for the 10-micron-diameter particles by the 3-to-1 concurrently coupled model to that of the boundary coupled model. For completeness, a 1-to-1 simulation was also run and is included in Figure 59.

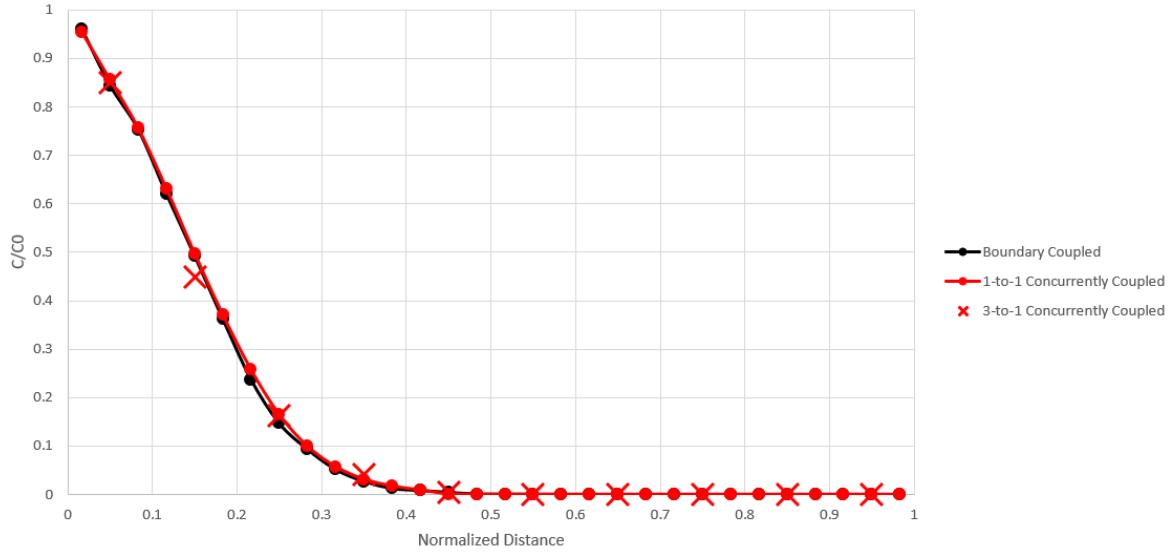


Figure 59. Concentration profile comparison of 3-to-1 and boundary coupled simulations.

The 3-to-1 concurrently coupled simulation results compared favorably with those of the boundary coupled model, indicating that the changes in grid cell properties were properly calculated and updated by the embedded PNMs. While promising, the result could have been achieved using an empirical formulation for network properties due to the fact that a single particle size was used in the simulation. The utility of the concurrently coupled model was evaluated by using more complex simulations involving multiple particles sizes.

#### 3.1.4. One-Dimensional 3-to-1 Concurrent Coupling – Multiple Particle Sizes

Given that many systems involving particle transport and retention involve particles with multiple sizes, the multi-species capabilities of the concurrently coupled model were tested. The ability to flexibly handle multiple particle species is a key advantage of concurrently coupled simulators. Traditional finite difference models rely on empirical formulations of key parameters to determine updated grid block properties. Although this is possible for single particle size systems, as was demonstrated in section 2.4.3, it is highly impractical for multi-particle size systems. To investigate this and highlight the benefit of using a concurrently coupled model, preliminary simulations were run on a single Berea PNM to investigate the impact of different particle sizes and sequences on particle transport and retention behavior.

The simplest multi-size particle system, that of two different particles sizes, was used in the simulations. These two-particle size simulations are referred to as A/B simulations in this work representing the two sizes. In the first A/B simulation, 10,000 7-micron-diameter particles were injected into a single Berea PNM over two network pore volumes, immediately followed by 10,000 10-micron-diameter particles over an additional two pore volumes. The resulting effluent concentration curve is shown in Figure 60. Simulation results are summarized in Table 13.

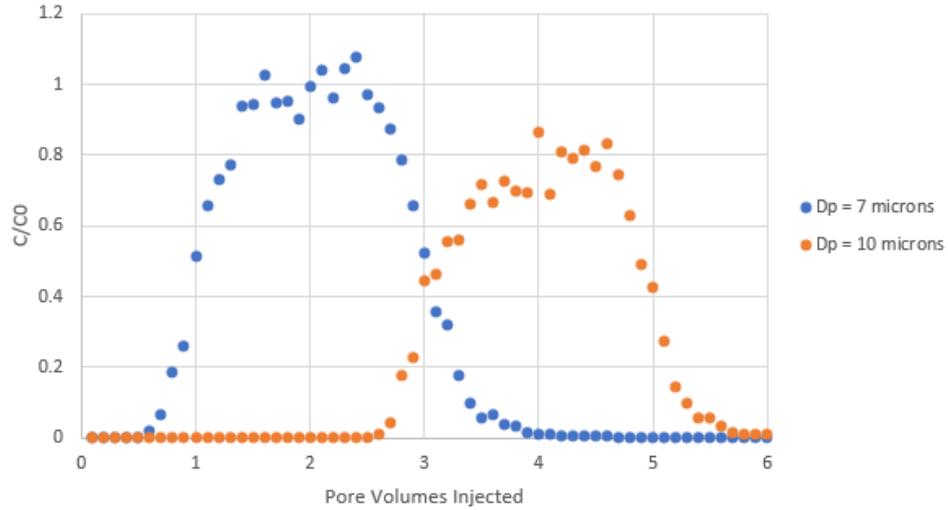


Figure 60. Effluent concentration curves for 10,000 7-micron-diameter particles followed by 10,000 10-micron-diameter particles into a Berea PNM.

Table 13. Particle retention summary for Figure 60.

Particle Diameter (microns)	Number Injected	Number Retained	Percent Retained	Retention Coefficient (1/s)
7	10,000	0	0.0	0
10	10,000	2,380	23.8	8.91E-02

None of the 7-micron-diameter particles were retained while 23.8% of the subsequent 10-micron-diameter particles were retained in the Berea PNM. Throat radii of the Berea PNM were analyzed to investigate the absence of retention of the 7-micron-diameter particles. A histogram of the throat diameter of curvatures (TDC) for each throat in the PNM is provided in Figure 61, where a TDC is defined as the tightest diameter of curvature, as measured by the smallest inscribed sphere that can pass through a throat.



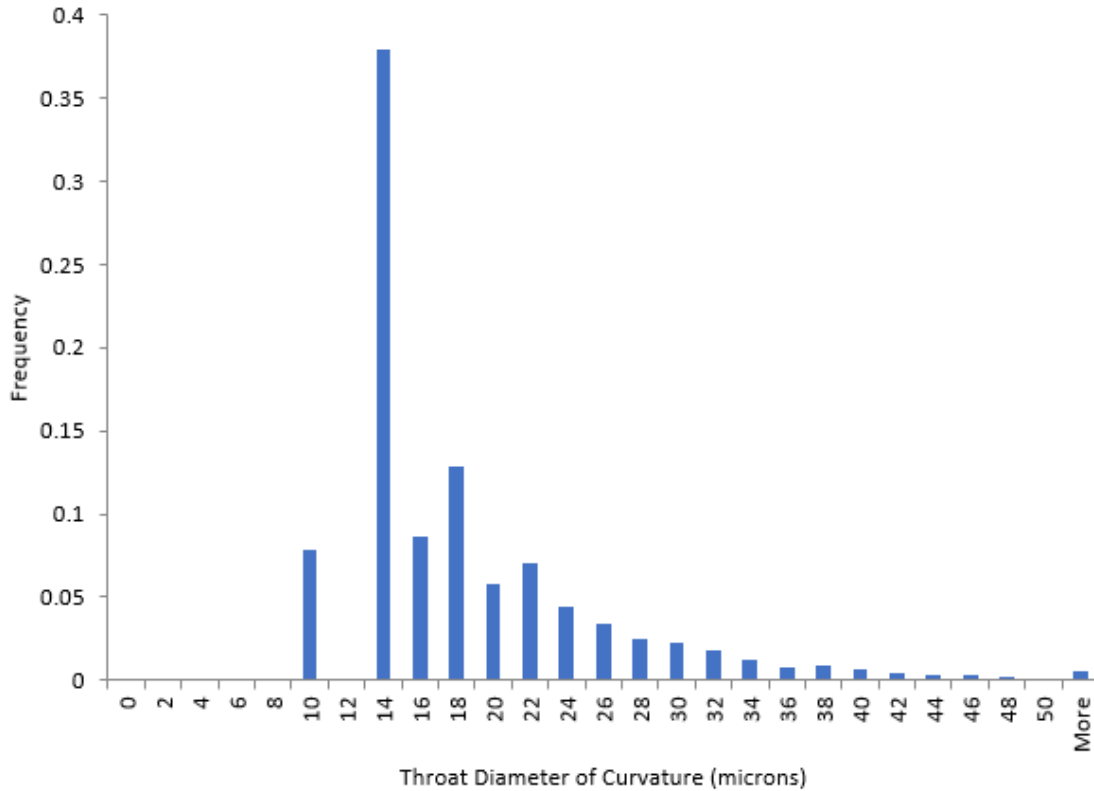


Figure 61. Histogram of throat diameter of curvatures for the Berea PNM.

It is clear that none of the seven micron particles were retained in the previous simulation because no throats were small enough for them to become trapped. The unrealistic features of the throat TDC histogram, such as the lack of throats with TCD values between zero and nine microns, is likely a consequence of the finite resolution of the microtomography image used to create the Berea PNM. Despite the limitations of the three-dimensional digital imaging and network generation process, the Berea PNM was still valid for investigating particle transport and retention.

The subsequent A/B simulation was identical to that run previously, however the 10-micron-diameter particles were injected first and the 7-micron-diameter particles were injected thereafter. Effluent concentration curves and the simulation result summary are shown in Figure 62 and Table 14 respectively.

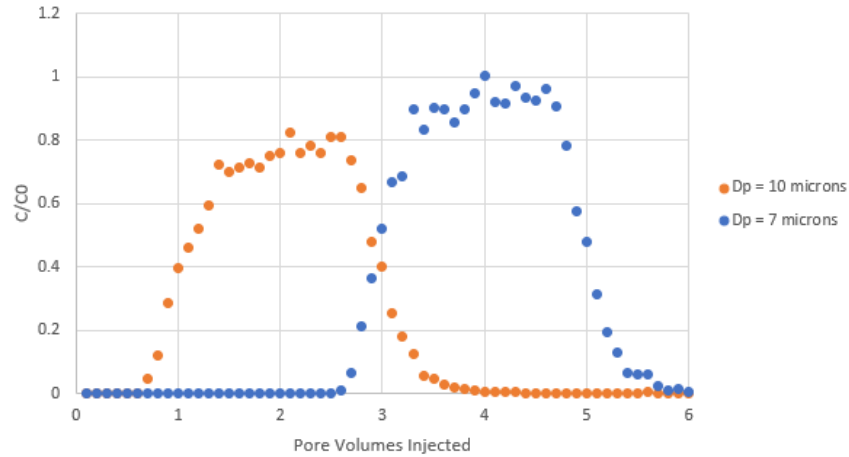


Figure 62. Effluent concentration curves for 10,000 10-micron-diameter particles followed by 10,000 7-micron-diameter particles into a Berea PNM.

Table 14. Particle retention summary for Figure 62.

Particle Diameter (microns)	Number Injected	Number Retained	Percent Retained	Retention Coefficient (1/s)
10	10,000	2,338	23.4	8.76E-02
7	10,000	473	4.7	1.08E-02

The injection of 10-micron-diameter particles led to an increase in the retention of seven micron particles from zero to about five percent. This demonstrates that for certain situations, particle sequence can impact transport and retention behavior. For the sake of completeness, an additional A/B simulation was performed which was identical to the first two, with the modification that injection of 14-micron-diameter particles was followed by the injection of 7-micron-diameter particles. Effluent concentration curves and the simulation result summary are shown in Figure 63 and Table 15 respectively.

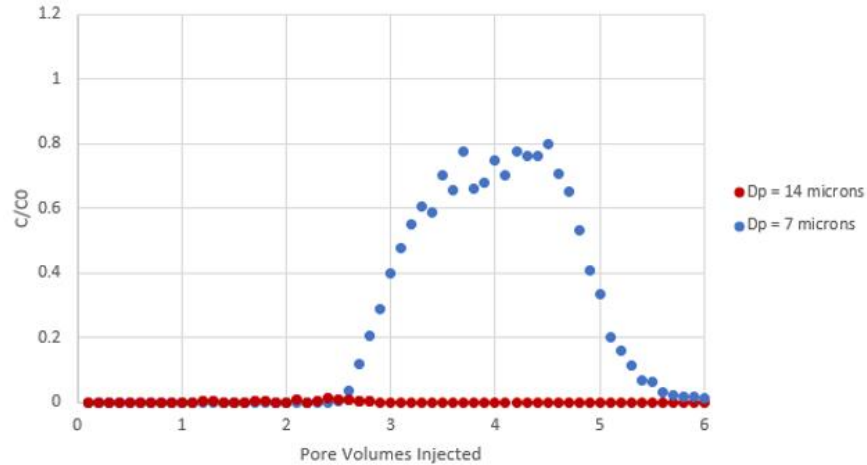


Figure 63. Effluent concentration curves for 10,000 14-micron-diameter particles followed by 10,000 7-micron-diameter particles into a Berea PNM

Table 15. Particle retention summary for Figure 63.

Particle Diameter (microns)	Number Injected	Number Retained	Percent Retained	Retention Coefficient (1/s)
14	10,000	9,974	99.7	1.77
7	10,000	2,678	26.8	1.03E-1

Nearly all of the relatively large 14-micron-diameter particles were retained in the PNM, which led to over 25% of the 7-micron particles being retained. Thus, both the size and sequence of particles entering a porous medium can have a significant impact on the transport and retention of those particles. While particle size and sequence can clearly impact transport behavior, the previous A/B simulations involved particle sizes that resulted in particles which were nearly all retained or all passed through the Berea PNM.

A second set of A/B simulations was performed to investigate the magnitudes of the impacts of particle size and sequence on transport behavior. To this end, A/B simulations were performed using more moderate particle diameters of 10 and 13 microns. A series of three A/B simulations were performed on the Berea PNM. These three A/B simulations will be referred to as Cases A, B, and C and are described in table 16.

Table 16. A/B simulation descriptions for cases A, B, and C.

Simulation Case	Description
<b>A</b>	15,000 10-micron-diameter particles injected over 3 PNM pore volumes, followed by 15,000 13-micron-diameter particles injected over an additional 3 PNM pore volumes. Particles injected into Berea PNM.
<b>B</b>	15,000 13-micron-diameter particles injected over 3 PNM pore volumes, followed by 15,000 10-micron-diameter particles injected over an additional 3 PNM pore volumes. Particles injected into Berea PNM.
<b>C</b>	15,000 10-micron-diameter particles and 15,000 13-micron-diameter particles injected together over 6 PNM pore volumes. Particles injected into Berea PNM.

For all three cases, particles were injected at constant concentrations. For Case C, the 10 and 13-micron-diameter particles were mixed randomly. Effluent concentration curves for Cases A, B, and C are provided in Figures 64-66 and retention results are summarized in Table 17.

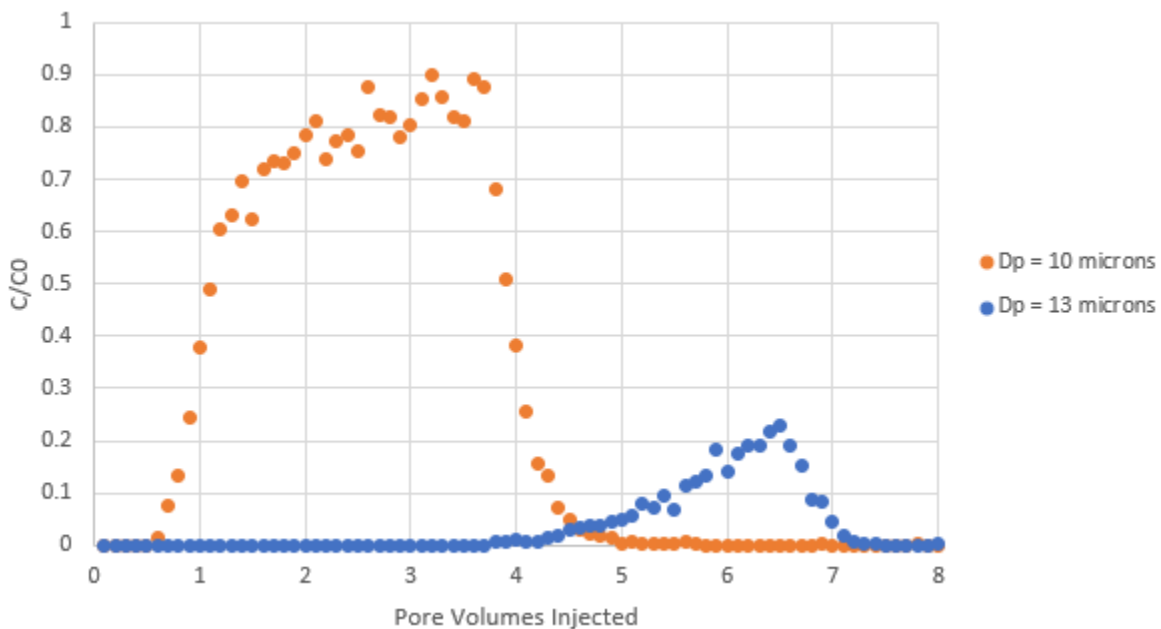


Figure 64. Effluent concentration curves for Case A: 15,000 10-micron-diameter particles followed by 15,000 13-micron-diameter particles injected into a Berea PNM.

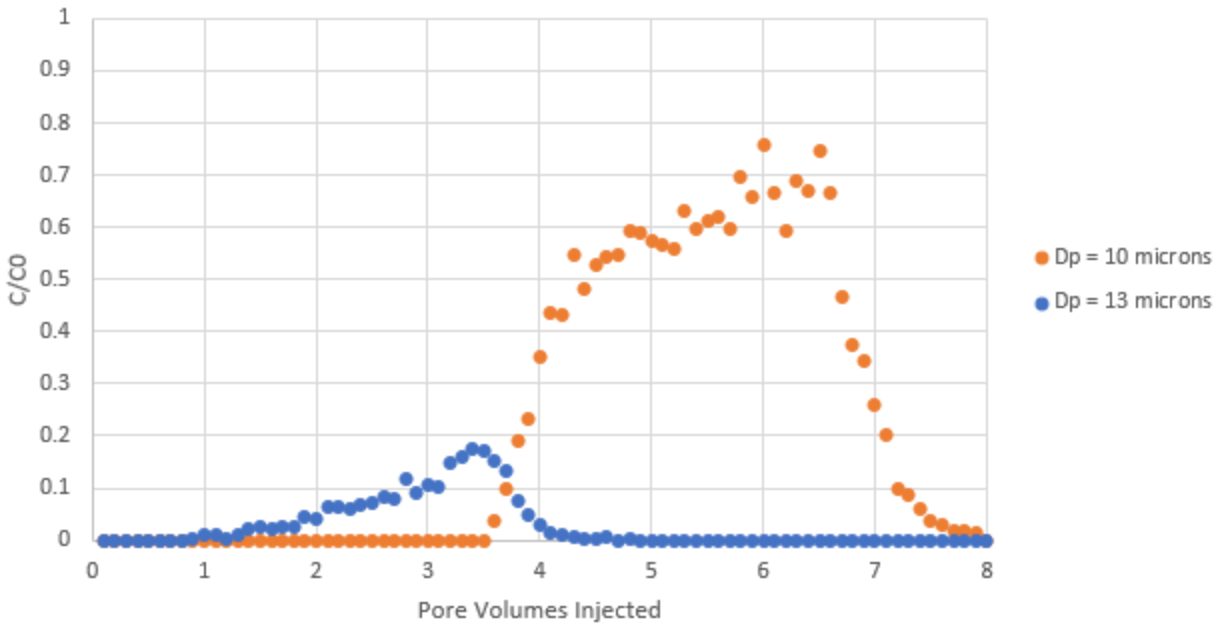


Figure 65. Effluent concentration curves for Case B: 15,000 13-micron-diameter particles followed by 15,000 10-micron-diameter particles injected into a Berea PNM.

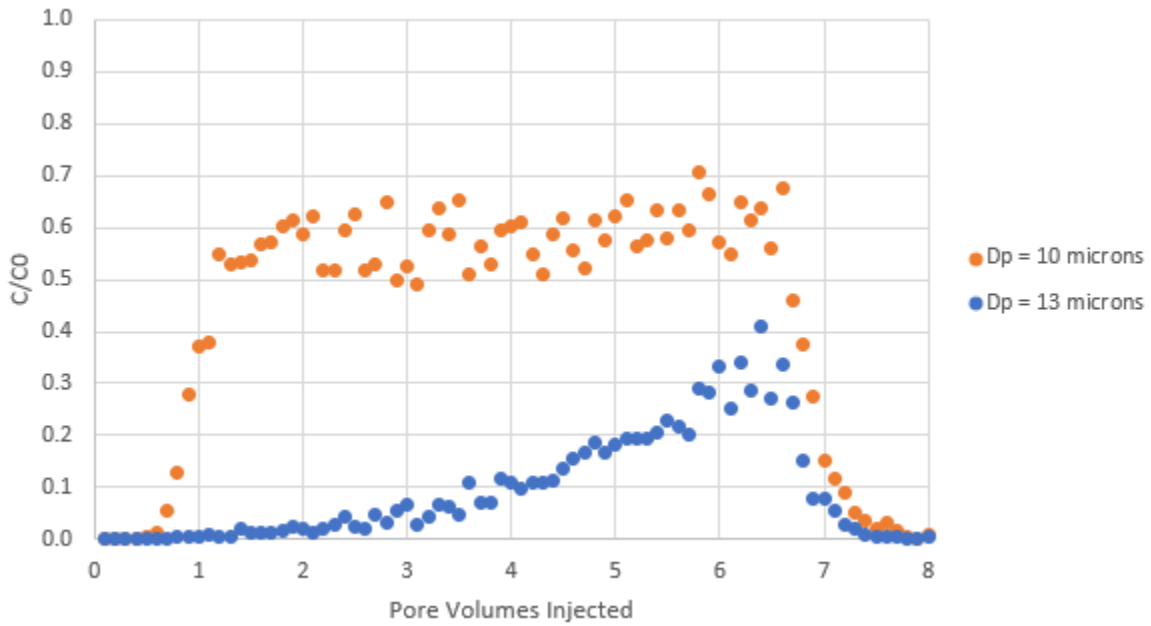


Figure 66. Effluent concentration curves for Case C: 15,000 10-micron-diameter particles and 15,000 13-micron-diameter particles mixed injection into a Berea PNM.

Table 17. A/B simulation results summary for cases A, B, and C.

<b>Simulation Case</b>	<b>Percent 10-micron-diameter Particles Retained</b>	<b>Percent 13-micron-diameter Particles Retained</b>
<b>A</b>	20.2	90.1
<b>B</b>	38.2	92.4
<b>C</b>	41.8	87.3

The smaller particle species had more than double the extent of retention in case C compared to case A. Although the larger particle size showed a smaller change in retention behavior, cases B and C differed in the number of trapped particles by 5.7%, a non-negligible amount. Particle size should therefore be appropriately incorporated into particle transport and retention models in order for them to be accurate.

Logical arguments can be made to explain the behavior of cases A and B, however the behavior of case C demonstrates the complexity of particle transport and retention. In case A, the smaller particles were injected first and likely plugged smaller throats, diverting the flow field into more of the larger throats. This likely led to the large particles subsequently injected in case A flowing into more large throats with less overall retention of the larger particle species. In case B, the injection of a larger particle species first resulted in greater retention of the smaller species. The larger particles likely became trapped in throats that the smaller particles would normally have been able to pass through, which reduced their throat sizes, leading to the observed greater retention of the larger species. Interestingly, the mixed injection in case C led to the largest retention of smaller particles and the least retention of the larger particles amongst cases A, B, and C. The retention behavior of particles therefore cannot simply be interpolated from more extreme cases of particle injection sequencing like cases A and B. This highlights the fact that particle transport and retention is fundamentally a pore-scale phenomenon. Models that incorporate pore-scale effects directly, such as concurrently coupled models, will have significant advantages over those that do not, such as traditional finite difference based models based on the ADE.

To verify that the results of cases A, B, and C were not unique to the PNM model used, two additional sets of A/B simulations were performed, one on a damaged version of the Berea PNM, and one on the RU PNM described in Section 2.1.1. To alter the Berea PNM, 15,000 13-micron-diameter particles (a size that becomes retained at a high rate) were injected into the Berea PNM. The resulting altered PNM is referred to as the damaged Berea PNM. The three A/B simulations run on the damaged Berea PNM are referred to as cases D, E, and F, and are described in table 18.

Table 18. A/B simulation descriptions for cases D, E, and F

Simulation Case	Description
<b>D</b>	10,000 10-micron-diameter particles injected over 2 PNM pore volumes, followed by 10,000 13-micron-diameter particles injected over an additional 2 PNM pore volumes. Particles injected into Berea PNM previously damaged by 15,000 13-micron-diameter particles.
<b>E</b>	10,000 13-micron-diameter particles injected over 2 PNM pore volumes, followed by 10,000 10-micron-diameter particles injected over an additional 2 PNM pore volumes. Particles injected into Berea PNM previously damaged by 15,000 13-micron-diameter particles.
<b>F</b>	10,000 10-micron-diameter particles and 10,000 13-micron-diameter particles injected together over 4 PNM pore volumes. Particles injected into Berea PNM previously damaged by 15,000 13-micron-diameter particles.

As with cases A, B, and C, particles were injected at constant concentrations. For Case F, the 10 and 13-micron-diameter particles were mixed randomly. Effluent concentration curves for Cases D, E, and F are provided in Figures 67-69 and retention results are summarized in Table 19, which includes cases A, B, and C for comparison.

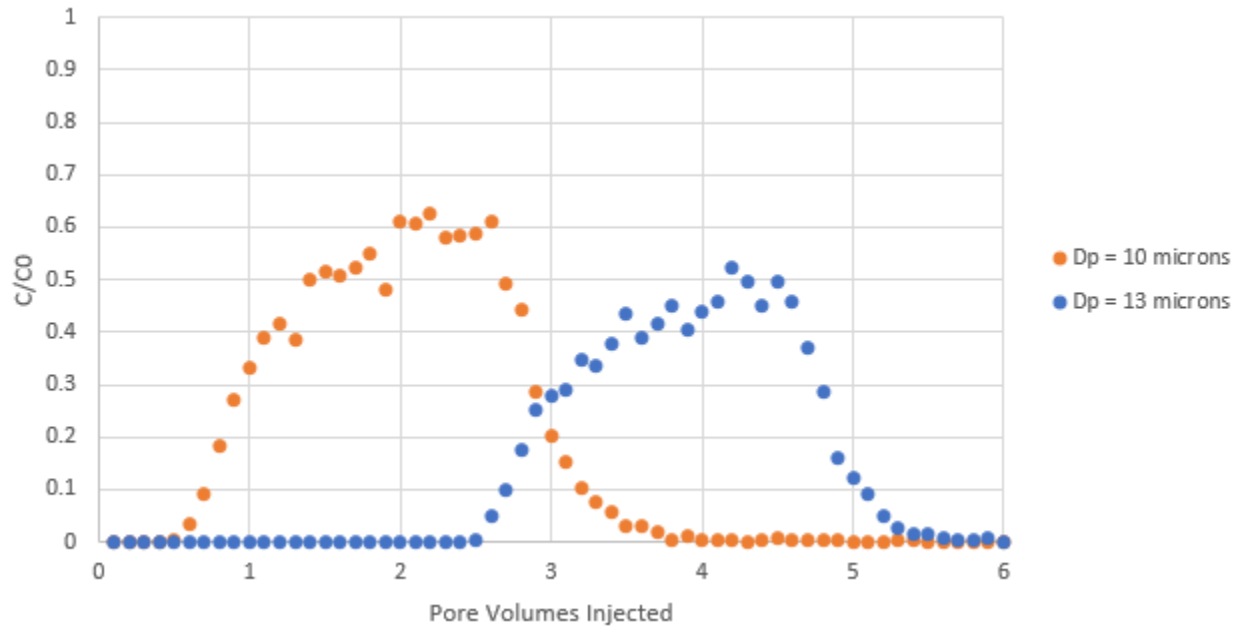


Figure 67. Effluent concentration curves for Case D: 10,000 10-micron-diameter particles followed by 10,000 13-micron-diameter particles injected into a Berea PNM.

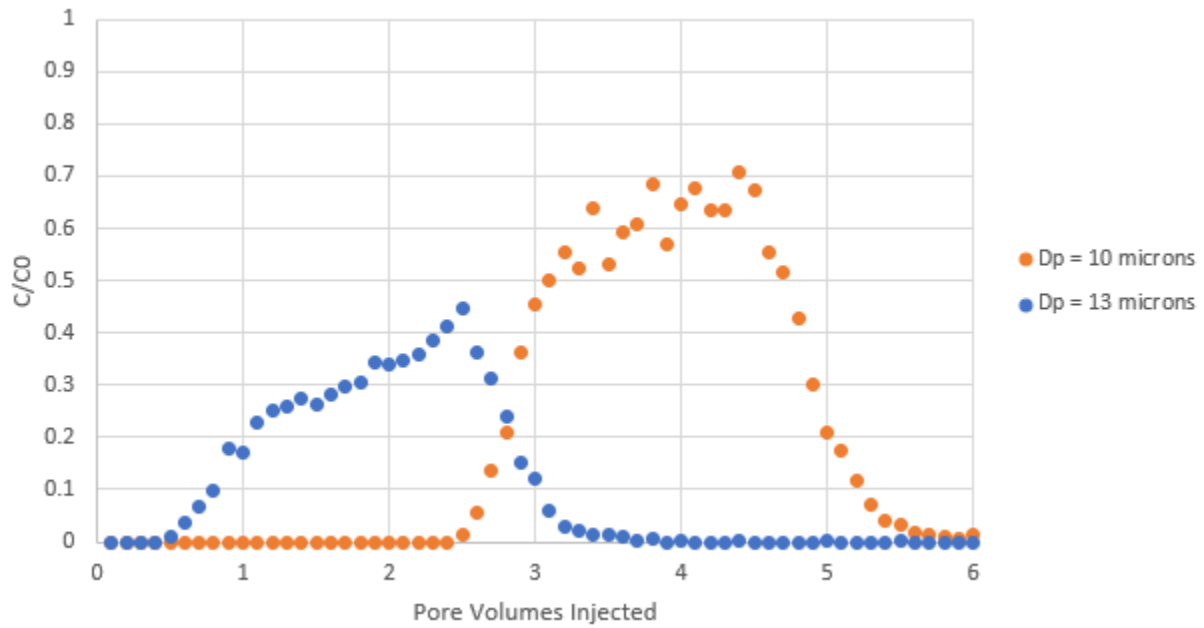


Figure 68. Effluent concentration curves for Case E: 10,000 13-micron-diameter particles followed by 10,000 10-micron-diameter particles injected into a Berea PNM.

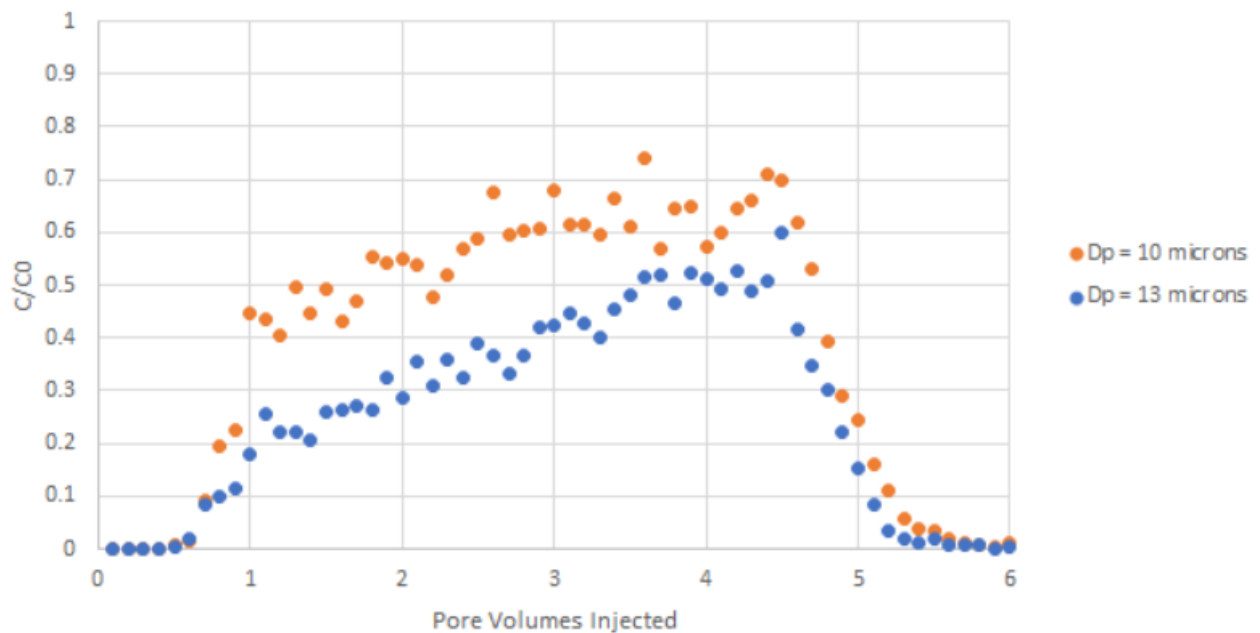


Figure 69. Effluent concentration curves for Case F: 10,000 10-micron-diameter particles and 10,000 13-micron-diameter particles mixed injection into the damaged Berea PNM.



Table 19. A/B simulation results summary for cases A through F.

Simulation Case	Percent 10-micron-diameter Particles Retained	Percent 13-micron-diameter Particles Retained
A	20.2	90.1
B	38.2	92.4
C	41.8	87.3
D	43.4	56.1
E	35.4	66.5
F	40.5	60.7

With a significant amount of particle trapping having already taken place in the damaged Berea PNM, the amount of retained 10 and 13-micron-diameter particles was closer in cases D, E, and F compared to cases A, B, and C. Although the sequence and sizes of particles in cases D, E, and F mimicked cases A, B, and C, the relative retention of the cases differed significantly. For example, case A showed the *lowest* amount of 10-micron particle retention amongst cases A, B, and C. As with case A, case D had 10-micron particles being injected first, however the 10-micron particles exhibited the *greatest* amount of retention amongst cases D, E, and F. This further demonstrates the need for pore-scale modeling, as relative retention behaviors can change within a single system as that system's properties change.

A final set of A/B simulations for testing purposes were run on the RU PNM. As with cases A through F, two particle sizes were selected that would exhibit moderately low and moderately large amounts of retention. To identify appropriate particle sizes, the throat diameters of curvature of the RU PNM system, plotted as a histogram in Figure 70, were analyzed.

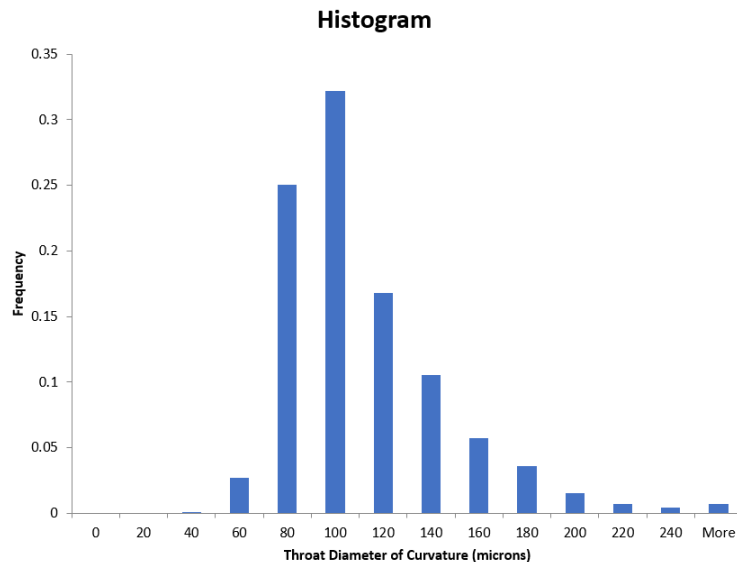


Figure 70. Histogram of throat diameter of curvatures for the RU PNM.

Given the that the RU PNM was made of a random packing of spheres, its throat size distribution follows a smooth log-normal distribution. Upon analysis of the distribution, particle diameters of 70 microns (mostly non-trapping) and 85 microns (moderately likely to trap) were selected for use in the A/B simulations. Three simulations were run on the RU PNM with similar parameters to cases D, E, and F. Descriptions of the A/B simulations run on the damaged RU PNM, referred to as cases G, H, and I are provided in table 20.

Table 20. A/B simulation descriptions for cases E, F, and G.

Simulation Case	Description
<b>G</b>	10,000 70-micron-diameter particles injected over 2 PNM pore volumes, followed by 10,000 85-micron-diameter particles injected over an additional 2 PNM pore volumes. Particles injected into the RU PNM.
<b>H</b>	10,000 85-micron-diameter particles injected over 2 PNM pore volumes, followed by 10,000 70-micron-diameter particles injected over an additional 2 PNM pore volumes. Particles injected into the RU PNM.
<b>I</b>	10,000 70-micron-diameter particles and 10,000 85-micron-diameter particles injected together over 4 PNM pore volumes. Particles injected into the RU PNM.

Effluent concentration curves for Cases G, H, and I are provided in Figures 71-73 and retention results are summarized in Table 21, which includes cases A through F for comparison.

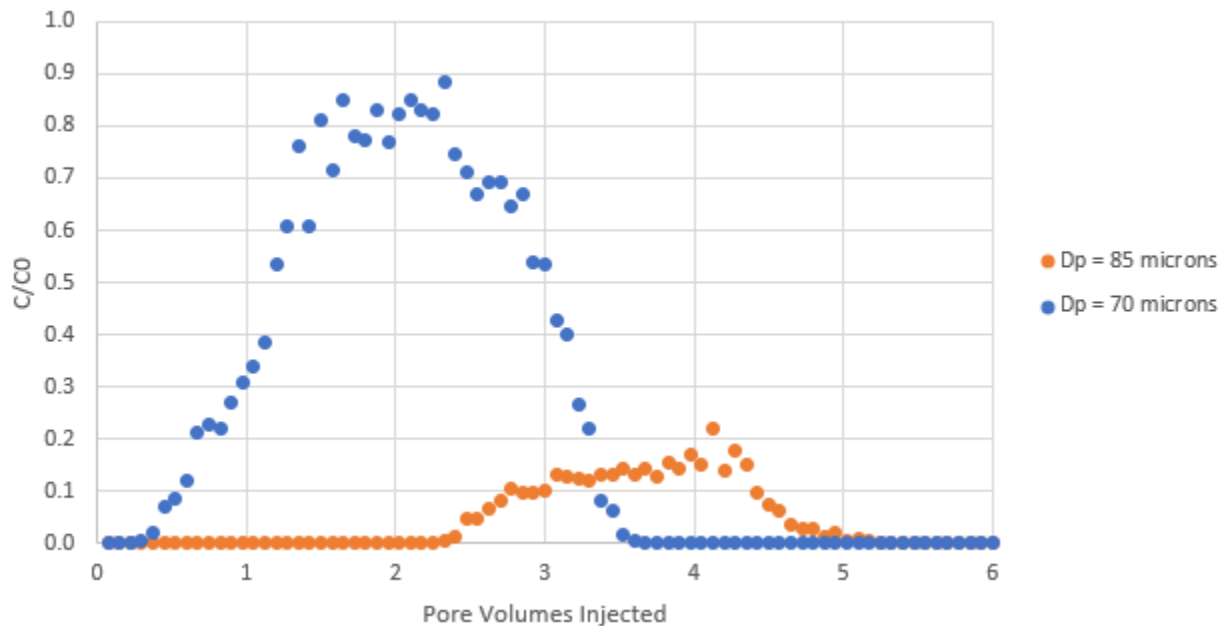


Figure 71. Effluent concentration curves for Case G: 10,000 70-micron-diameter particles followed by 10,000 85-micron-diameter particles injected into the RU PNM.

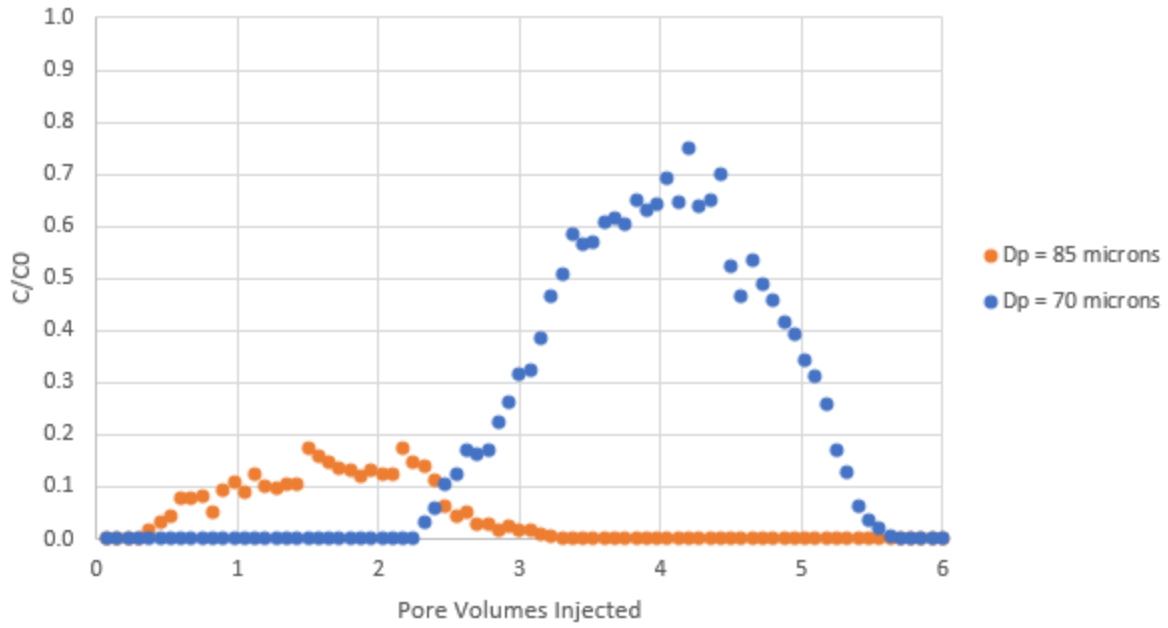


Figure 72. Effluent concentration curves for Case H: 10,000 85-micron-diameter particles followed by 10,000 70-micron-diameter particles injected into the RU PNM.

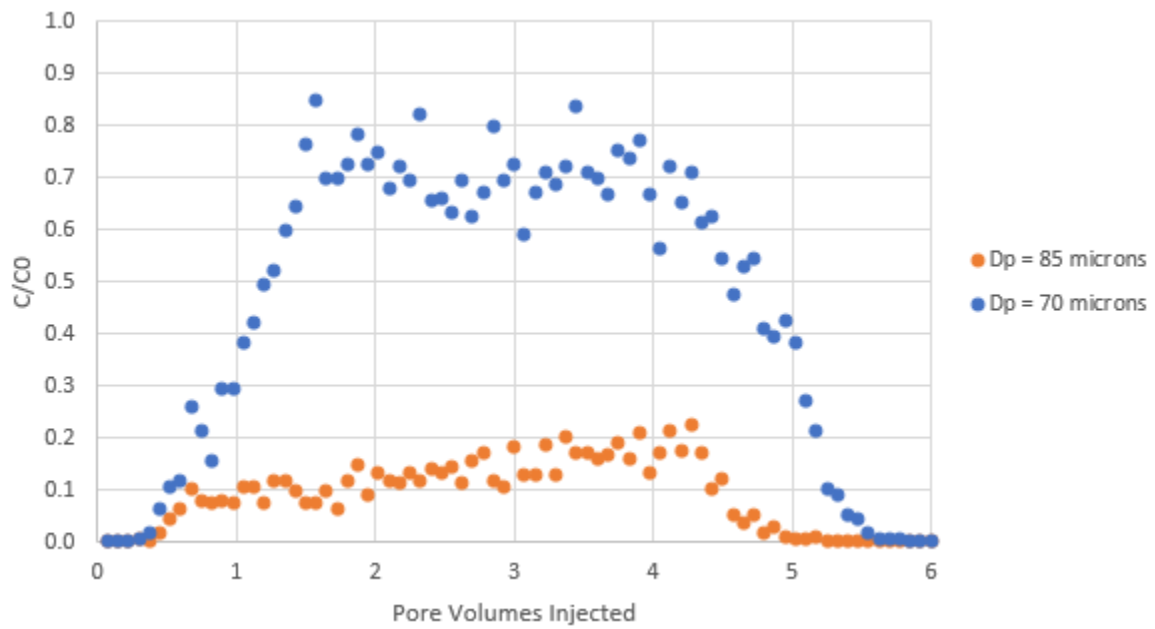


Figure 73. Effluent concentration curves for Case I: 10,000 70-micron-diameter particles and 10,000 85-micron-diameter particles mixed injection into the RU PNM.

Table 21. A/B simulation results summary for cases A through I.

<b>Simulation Case</b>	<b>Percent of Smaller Particle Species Retained (10-micron-diameter for cases A-F, 70-micron-diameter for cases G-I)</b>	<b>Percent of Larger Particle Species Retained (13-micron-diameter for cases A-F, 85-micron-diameter for cases G-I)</b>
<b>A</b>	20.2	90.1
<b>B</b>	38.2	92.4
<b>C</b>	41.8	87.3
<b>D</b>	43.4	56.1
<b>E</b>	35.4	66.5
<b>F</b>	40.5	60.7
<b>G</b>	17.9	86.3
<b>H</b>	34.4	87.5
<b>I</b>	30.1	86.5

The retention results for cases G, H, and I are different from those of A, B, and C and D, E, and F in regard to the relative amounts of retention for the different sequences of smaller and larger particles. More specifically, case H was the only case in which the injection of the larger particle first resulted in the highest amount of small particle species retention. Also, cases G, H, and I exhibited little difference in the retention behavior of the larger species compared to cases A, B, and C and cases D, E, and F. Therefore, particle size and sequence were seen to impact multiple porous media samples, which provides evidence that these parameters should be accounted for in a wide range of, if not all, systems in which particle transport and retention is being modeled.

The A/B simulations above demonstrate that particle size, number, and sequence can have significant impacts on particle transport behavior. For a traditional finite difference simulator to accurately account for these parameters an empirical formulation would need to be made for an effectively infinite combination of particle sizes, sequences, and amounts. This poses a significant limitation in the ability of traditional finite difference simulators to accurately model particle transport and retention. While this limitation was demonstrated for the simplest of multi-particle systems, the situation becomes even more intractable for systems with more than two particle sizes. While boundary coupled PNM simulations can easily handle multiple particle sizes, they are very limited in scale. On the other hand, concurrently coupled models enable system sizes at practical scales and the ability to accurately simulate multi-particle size systems in a computationally efficient manner.

To remove the effects of the digital imaging process (which gave discrete pore and throat sizes) for subsequent simulations, a portion of the throats with TDC values between 13 and 15 microns were adjusted so that the TDC distribution would more closely follow a log-normal distribution. Figure 74 shows the adjusted TDC histogram for the Berea PNM and Figure 75 compares the original and adjusted values to a log-normal distribution. Although Figure 75 should technically be plotted as a histogram, for the sake of simpler interpretation it is displayed as an XY scatter plot with lines.

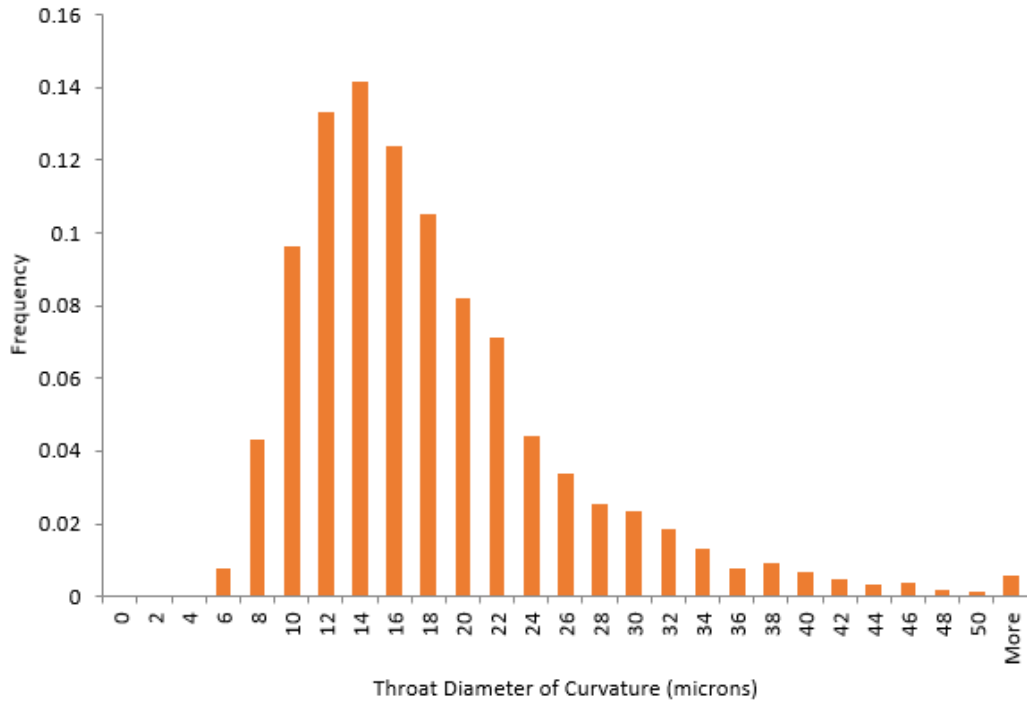


Figure 74. Histogram of throat diameter of curvatures for the adjusted Berea PNM.

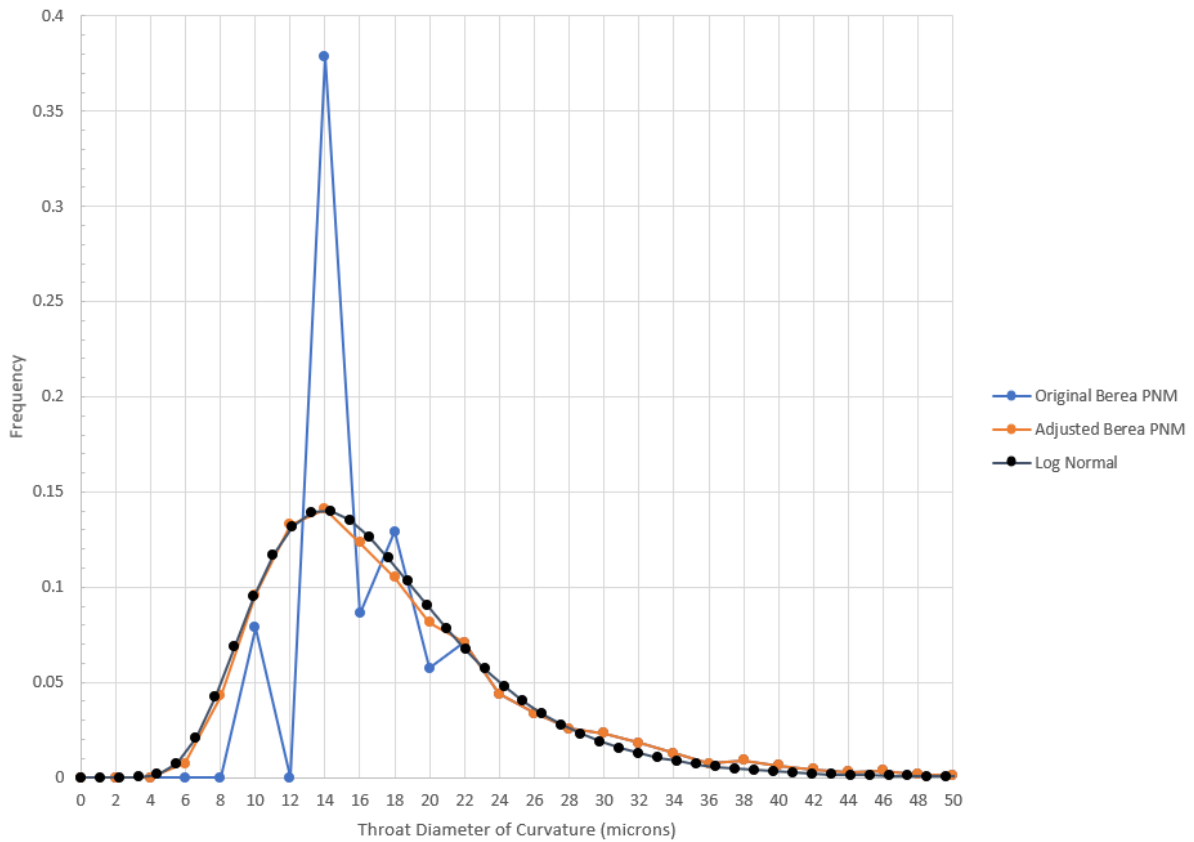


Figure 75. Comparison of throat diameter of curvature distributions of the original and adjusted Berea PNM to a log-normal distribution.

The Berea PNM with adjusted TDC values more closely follows a log-normal distribution compared to the original Berea PNM. The adjusted throats were selected randomly amongst those with TDC values in the 13 to 15 micron range, and the new TDC values were randomly assigned. For consistency, relevant PNM parameters dependent on TDC, such as hydraulic conductance, were adjusted proportionally.

In analyzing the effluent concentration data during this A/B testing a phenomenon related to determining retention coefficients became evident. In many of the effluent concentration curves of cases A through I, the plateau of the curve had a positive slope, rather than a slope of zero, which would be predicted by the modified version of classical colloidal filtration theory (CFT) with a single-coefficient retention model. Even though CFT models particle retention due to mechanisms other than straining, it provides valuable insight into the macroscopic retention behavior that can be captured by single-coefficient models, so it is used here for comparison purposes. The phenomenon of non-zero slope effluent concentration plateaus is particularly noticeably in cases E and F. French (2015) also noticed this phenomenon. Figure 76 from French (2015) shows effluent concentration curves for three cases of different numbers of particles (ten thousand, one hundred thousand, and one million) of uniform size being injected into 10 boundary coupled PNMs. Also shown are effluent concentration curves as predicted by the modified CFT, where the retention and dispersion coefficients used in the modified CFT models were evaluated from effluent concentration curves of the same numbers of particles injected into a single PNM.

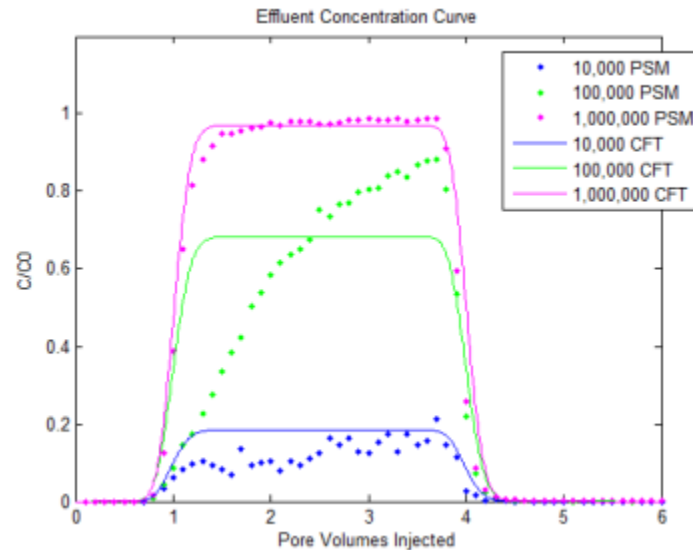


Figure 76. Effluent curves produced by three sets of simulations injecting different number of particles into ten network models in series and comparing the results to the CFT model using a dispersion and retention coefficient obtained from a single network model. (French, 2015)

It is highly likely that the upward slopes of the plateaus were due to changing retention coefficients during the simulations. Early in the simulations, retention coefficients will be highest and the values of effluent concentrations will be lowest. As the simulation progresses, particle retention causes flow to divert into only the throats large enough for particles to pass through. The lessened

particle retention at the end of the simulation leads to higher effluent concentrations and an overall upwards sloping effluent concentration profile. The effect is moderate in the simulation with 10,000 particles and very significant in the simulation with 100,000 particles. Thus, the more significant slope in the 100,000 particle case was likely due to a greater change in retention coefficient. The effect is muted in the simulation with 1,000,000 particles likely because the large number of particles caused the retention coefficient to approach zero rapidly, from where it could not change significantly. As can be seen in the 100,000 case, the effluent concentration is nearly 1.0 at the end of the simulation. This implies that the retention concentration was nearly zero after approximately 0.4 pore volumes (100,000 particles injected) for the 1,000,000 particle case. The effluent concentration curve approaching 1.0 approximately 0.4 pore volumes after breakthrough for the 1,000,000 particle case supports this inference.

This phenomenon has important consequences. Firstly, retention coefficients should be evaluated at specific points in time, not by fitting CFT models to raw effluent concentration curves. If the latter approach is used, retention coefficient values may not be accurate because 1) CFT modified with single-coefficient retention models predict zero slope effluent concentration profiles while effluent concentration curves can have a slope and 2) the value of the retention coefficient may change from the beginning of the simulation in a non-linear manner, making it difficult to identify at what point the computed value actually represented the system. As discussed in Section 2.1.3., this work evaluates retention coefficients as specific points in time by determining the number of particles that *would* become retained in the system, but does not actually retain those particles or alter the system when doing so. Thus, when determining the retention coefficient in this work the system does not change, which enables the retention coefficient to remain constant. Attempting to determine the retention coefficient in a manner that alters the system, such as using an effluent concentration curve from a particle retention simulation, will lead to artificially low values of retention coefficient. The greater the number of particles used to evaluate the retention coefficient, the lower the value will be. This is due to the fact that retention coefficients trend to zero as all throats that are too small for particles to become trapped get plugged and flow is diverted such that only throats large enough for particles to pass through remain. Thus although large numbers of particles may be used to achieve statistical significance, this will make the calculated value more precise but artificially low. Evidence of this can be seen in the 10,000 particle case (blue data set) in Figure 76, where an artificially low value of retention coefficient likely led to the modified CFT model under-predicting the amount of particle retention. Critically, because the concurrently coupled model developed in this work evaluates retention coefficients at specific points in time, it has the ability to calculate retention coefficients as frequently as needed. This ability would be needed any time the retention coefficient changed rapidly. For example, if the retention coefficient changed by 10% after just 100 particles were injected, the retention coefficient could be accurately determined by the model in this work. However, an effluent concentration curve based on so few particles would likely have a large amount of noise, leading to an inaccurate retention coefficient value. Although retention coefficients were the focus of this discussion, similar arguments could be made for any dynamic property derived from a pore-scale model.

Having established that particle size and sequence can have a material impact on transport and retention, 3-to-1 concurrently coupled simulations were performed to test the model for accuracy in evaluating these parameters. Two 3-to-1 concurrently coupled A/B simulations were run in addition to the previous 3-to-1 simulation with a single particle size. The two additional

simulations involved particles of 10 and 13-micron-diameters. To make the results of the A/B simulations comparable to those of Section 3.1.3., the same non-particle simulation parameters (boundary flow rate, fluid viscosity, and system length) were used. Descriptions of the three A/B 3-to-1 simulations are provided in Table 22.

Table 22. A/B simulation descriptions for 3-to-1 concurrently coupled simulation cases.

Simulation Case	Description
<b>2A</b>	25,000 10-micron-diameter particles injected over 0.5 system pore volumes. Particles injected into 10 3-to-1 finite difference grid cells each embedded with a Berea PNM (identical simulation to that in Section 2.4.3).
<b>2B</b>	25,000 13-micron-diameter particles injected over 0.5 system pore volumes, followed by 25,000 10-micron-diameter particles injected over an additional 0.5 PNM pore volumes. Particles injected into 10 3-to-1 finite difference grid cells each embedded with a Berea PNM.
<b>2C</b>	25,000 10-micron-diameter particles and 25,000 13-micron-diameter particles injected together over 0.5 system pore volumes. Particles injected into 10 3-to-1 finite difference grid cells each embedded with a Berea PNM.

As with the single particle size 3-to-1 case shown in Figure 58, boundary coupled simulations were run for each case to obtain results to which the concurrently coupled models could be compared. The boundary coupled simulations involved 30 Berea PNMs to make the system equivalent in size to the 3-to-1 case. Concentration profiles of the 10-micron-diameter particles for each boundary coupled simulation are plotted in Figure 77. For the sake of comparison, the concentration profiles were taken after 0.5 pore volumes of injection of the 10-micron-diameter particle species. This corresponded to simulation times of 0.5 pore volumes for cases 2A and 2C, and 1.0 pore volumes for case 2B.

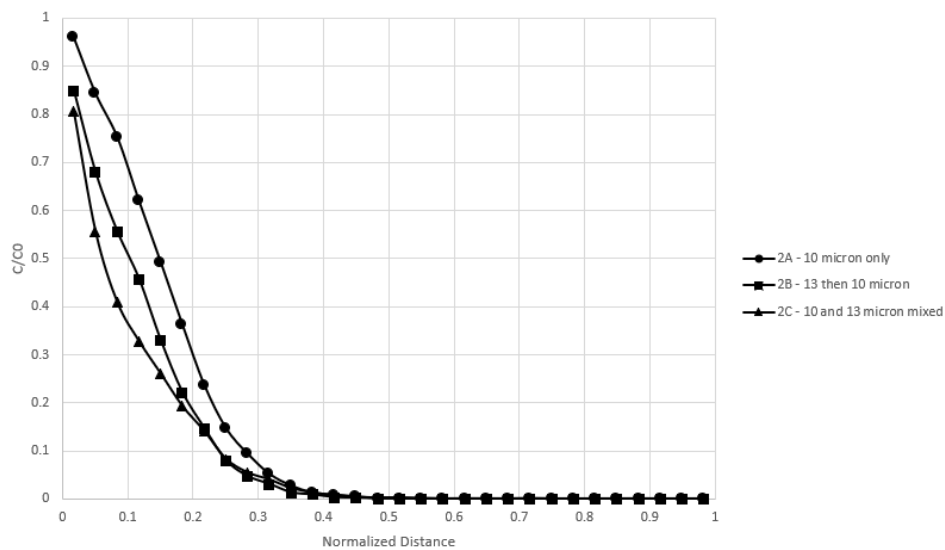


Figure 77. 10-micron particle species concentration profiles for 30 boundary coupled PNM baseline simulations for cases 2A, 2B and 2C.



Noticeable differences in the concentration profiles for the 10-micron particles were observed in the baseline PNM results. The differences in these profiles are due solely to the order in which the two particle sizes entered the system. Qualitatively, the behavior of cases 2A and 2C match that observed in the experimental work of Xu and Saiers (2009), which investigated the transport of single and bidisperse particle suspensions. Xu and Saiers (2009) noted that the extent of retention for the smaller particle species in the monodisperse case (2A in this work) was less than that in the bidisperse case (2C in this work). Xu and Saiers (2009) attributed the increased retention of the smaller species in the mixed case to the larger species partially constricting pore throats that the smaller species would have otherwise been able to pass through. The ability of the boundary coupled model to achieve a qualitative match with comparable experimental data provides evidence that the straining rules implemented by the PNM were physically realistic.

As previously discussed, such results would be very difficult to model with a traditional finite difference simulator based on the ADE. Such a model would need to rely on complex empirical formulations to obtain grid block properties such as particle retention and dispersion coefficients. These empirical formulations would be time consuming to create and limited to the specific particle sizes used in this simulation. For a system containing multiple particle sizes, those models would be inaccurate and prohibitively time consuming to create.

3-to-1 concurrently coupled simulations were run for each case and compared to the baseline boundary coupled PNM results. All simulations used 100 finite difference time steps with PNM updates at each time step. The number of time steps utilized was sufficient to minimize the effects of numerical dispersion. Grid block properties were also updated frequently. In practice the simulator was made more efficient by only updating properties for grids that encountered entering particles. The results, as well as 1-to-1 concurrently coupled results are shown in Figure 78.

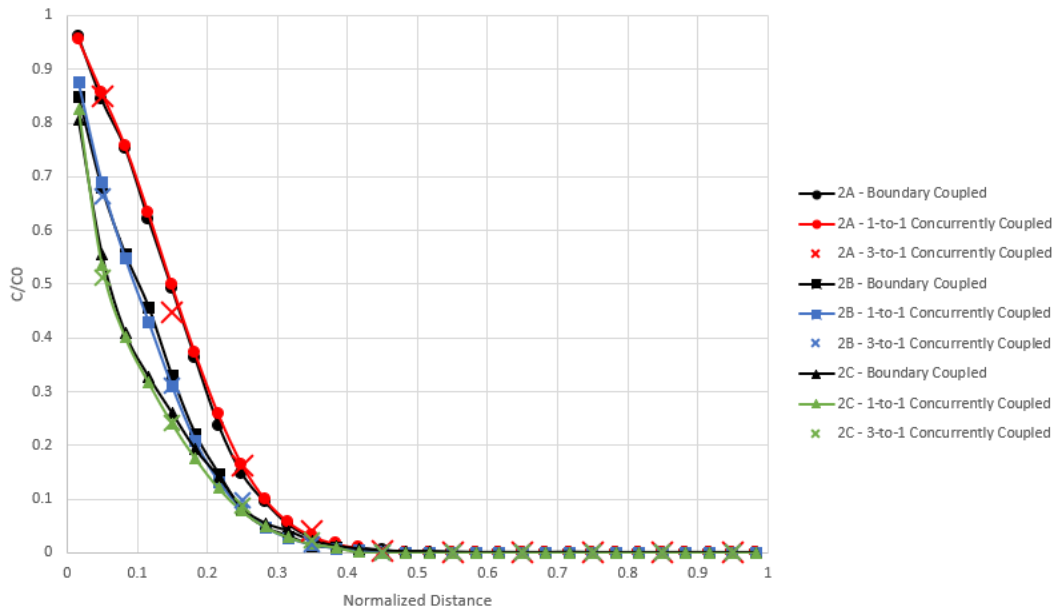


Figure 78. 10-micron concentration profile comparison of 3-to-1 and boundary coupled simulations for cases 2A, 2B, and 2C.

The concurrently coupled simulator was able to capture the complex transport behavior of the three situations. Accurate results were achieved despite the 3-to-1 discrepancy in the size of the finite difference grid blocks and embedded PNMs. This example demonstrates the potential for the concurrently coupled model to accurately incorporate complex pore-scale phenomena in a computationally efficient finite difference framework. The 3-to-1 size discrepancy also allowed for the same system size to be simulated with three times fewer PNMs than in the boundary coupled simulations. Furthermore, the concurrently coupled simulations solved for species properties in a flexible manner, which could have accounted for any number of particle sizes and sequences.

While the 3-to-1 results were promising, the total system length in these simulations was 10.5 cm. This scale indicated that concurrently coupled models can be used effectively at the core scale, however the ultimate goal of this work was to develop a concurrently coupled model that could be applied to field scale systems. To this end, the size discrepancy between finite difference grid block and embedded PNM was extended to an order-of-magnitude.

### 3.1.5. One-Dimensional 11-to-1 Concurrent Coupling – Multiple Particle Sizes

The final one-dimensional simulations run before running the model in three-dimensional space evaluated the accuracy of the concurrently coupled model in cases with an order-of-magnitude difference in size between finite difference grid and embedded PNMs. For a typical PNM on the order of centimeters, this size difference corresponds to system sizes on the order of meters, which is the scale of most practical laboratory problems, and represents a progression to the ultimate objective of this work. To achieve an order-of-magnitude difference in size, simulations were run in which each finite difference grid cell was 11 times larger in length than its embedded PNM.

Simulations were first run to evaluate the impact of how the number of particles entering the PNM at each time step ( $N_p$ ) was calculated. To reiterate, in the concurrently coupled simulations,  $N_p$  was calculated for each grid cell at the beginning of each time step to determine how many particles would be simulated as entering the embedded PNM during that time step. The formula used in this work to determine  $N_p$  for a given grid cell  $j$  and time step length  $\Delta t$  was

$$N_{p,j} = C_{j-\ell_{PNM}/2} Q \Delta t \quad (48)$$

where  $Q$  represents volumetric flow rate and  $C_{j-\ell_{PNM}/2}$  (units of number of particles per volume) represents particle concentration in block  $j$  evaluated at the upwind face of the embedded PNM. A priori it was not known that the upwind concentration used in Equation 48 should be evaluated at the upwind face of the embedded PNM. To arrive at this conclusion, simulations were run for two possible locations to evaluate the upwind particle concentration: at the upwind PNM face and at the upwind finite difference grid face. Figure 79 illustrates these upwind locations for an arbitrary grid block  $j$ .

To identify which of these upwind locations was most suitable for determining  $N_{p,j}$ , a baseline simulation was first obtained by simulating the injection of 500,000 10-micron-diameter particles into 660 boundary coupled Berea PNMs over 0.5 system pore volumes. Next, 1-to-1, 3-to-1, and 11-to-1 concurrently coupled simulations were run for the possible upwind locations to evaluate

the particle concentration used in determining  $N_{p,j}$ . The concentration values at the upwind locations were determined using linear interpolation between the concentrations evaluated at the centers of finite grid cells  $j$  and  $j-1$ . Linear interpolation was deemed to have enough accuracy for the purposes of this work because concentration gradients were relatively small in the scenarios simulated. For other work, involving scenarios with sharp concentration gradients, a more accurate method of interpolation could be implemented. The concentration profiles at the end of all simulations are plotted in Figure 80.

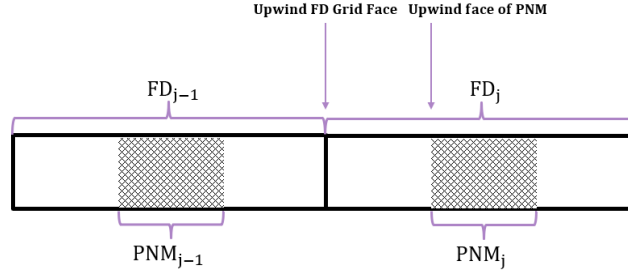


Figure 79. Illustration of potential upwind locations for evaluation of  $N_{p,j}$ .

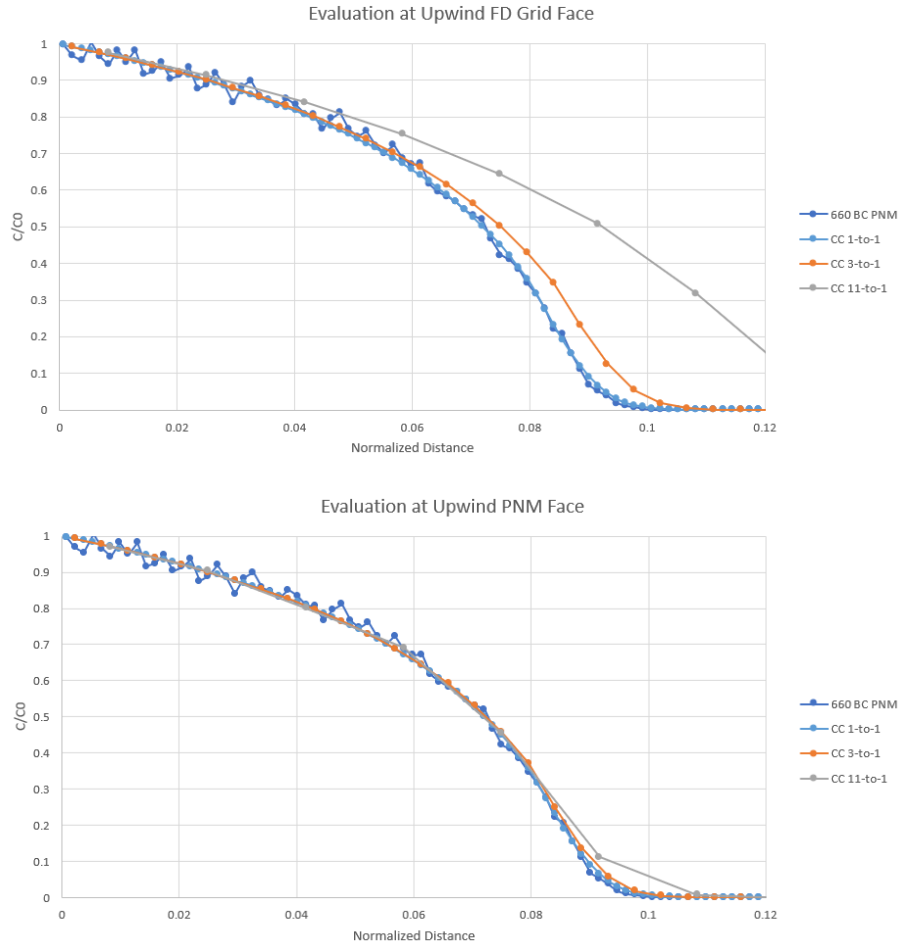


Figure 80. Comparison of upwind evaluation points for determining  $N_{p,j}$ : FD grid face (top) and PNM face (bottom).

Using the upwind PNM face as the location to evaluate particle concentration in determining  $N_{p,j}$  led to consistent results between the boundary coupled and concurrently coupled results. As the size discrepancy between finite difference grid blocks and embedded PNMs increased, error increased towards the end of the concentration profile (about 0.09 normalized distance). Given that the error in the 1-to-1 case was negligible and increased monotonically for the systems with larger size discrepancies between the pore and finite difference models, the error can most likely be attributed to numerical dispersion resulting from having fewer finite difference grids. Use of the upwind grid face was seen to overpredict concentration values for larger size discrepancies. Larger size discrepancies resulted in larger overpredictions of particle concentration values. For the 1-to-1 case the upwind grid face and embedded PNM are at the same location so both produce accurate results compared to the boundary coupled simulations. As the size discrepancy between the embedded PNM and finite difference grid increases, the distance between grid center and grid face increases. This led to use of a concentration value to predict  $N_{p,j}$  that was increasingly farther upwind, and in that case, higher. The higher concentration values led to higher values of  $N_{p,j}$ , more retained particles, lower values of retention coefficient, and ultimately higher concentration values. Comparing the two results it was clear that  $N_{p,j}$  should be evaluated using the concentration value upwind of the embedded PNM. This is conceptually reasonable, as the concentration at this location is most representative of the fluid that will enter the embedded PNM during the time step. Importantly, the 11-to-1 simulation was able to match the boundary coupled simulation, providing the first evidence that a concurrently coupled model can accurately simulate situations with an order-of-magnitude size difference between pore- and continuum-scale models. While promising, these preliminary results were for a single-particle-size species.

A/B simulations were performed to evaluate the ability of the concurrently coupled simulator to accurately predict multi-particle species transport in systems with order-of-magnitude discrepancies in size between embedded PNMs and finite difference grids. Systems composed of Berea PNMs with no prior particle damage only allow minimal penetration for moderately sized particles. As can be seen in Figure 80, particles had penetrated a normalized distance of 0.1 after more than half a million particles were injected over 0.5 pore volumes. To more quantitatively illustrate this point, Figure 81 shows concentration profiles for 100,000 particles injected into systems in which a fixed percentage of particles are trapped at in each grid block.

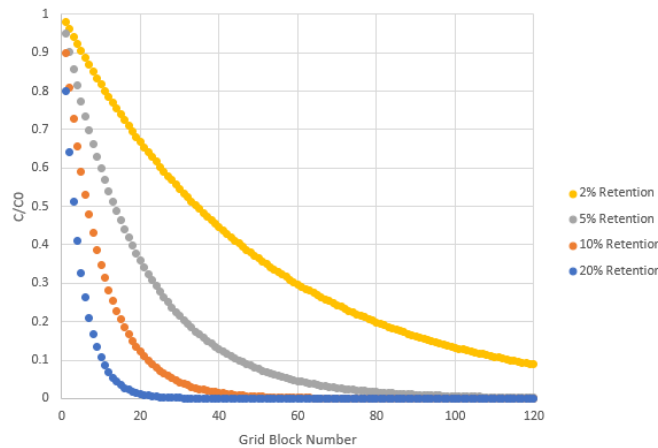


Figure 81. Concentration profiles for systems with fixed amount of retention in each grid block.

When 20% of particles are retained in each grid block, the farthest a particle species can reach is about 20 grids. The 20% retention value is moderately low given that in the A/B simulations in section 3.1.4., the initial retention rate of 10-micron-diameter particles for the Berea PNM was seen to vary from about 20-40%. In order to test the accuracy of an 11-to-1 system, a boundary coupled PNM simulation is needed as a baseline. A boundary coupled system of 110 PNMs was chosen for the 11-to-1 simulation baselines so that the concurrently coupled simulations would have ten nodes (roughly the minimum size desirable to reduce numerical dispersion). To allow particles to penetrate into the 110 PNM boundary coupled baseline simulations, the A/B simulations for the 11-to-1 cases used slightly smaller particle sizes of 7 and 10-micron-diameter particles. These particle sizes corresponded to 6.3% and 20.2% retention respectively.

Three A/B 11-to-1 simulation cases were run with 7 and 10-micron-diameter particles. Descriptions of the three simulations cases are provided in Table 23.

Table 23. A/B simulation descriptions for 11-to-1 concurrently coupled simulation cases.

<b>Simulation Case</b>	<b>Description</b>
<b>3A</b>	100,000 7-micron-diameter particles injected over 0.8 system pore volumes. Particles injected into 10 11-to-1 finite difference grid cells each embedded with a damaged Berea PNM.
<b>3B</b>	100,000 10-micron-diameter particles injected over 0.8 system pore volumes, followed by 100,000 7-micron-diameter particles injected over an additional 0.8 PNM pore volumes. Particles injected into 10 11-to-1 finite difference grid cells each embedded with a damaged Berea PNM.
<b>3C</b>	100,000 7-micron-diameter particles and 100,000 10-micron-diameter particles injected together over 0.8 system pore volumes. Particles injected into 10 11-to-1 finite difference grid cells each embedded with a damaged Berea PNM.

For each case, a boundary couple simulation of 110 damaged Berea PNMs was simulated to obtain a baseline concentration curve. The baseline boundary coupled concentration curves for the 7-micron-diameter particles are plotted in Figure 82. For the sake of comparison, the concentration profiles were taken after 0.8 pore volumes of injection of the 7-micron-diameter particle species. This corresponded to simulation times of 0.8 pore volumes for cases 3A and 3C and 1.6 pore volumes for case 3B.

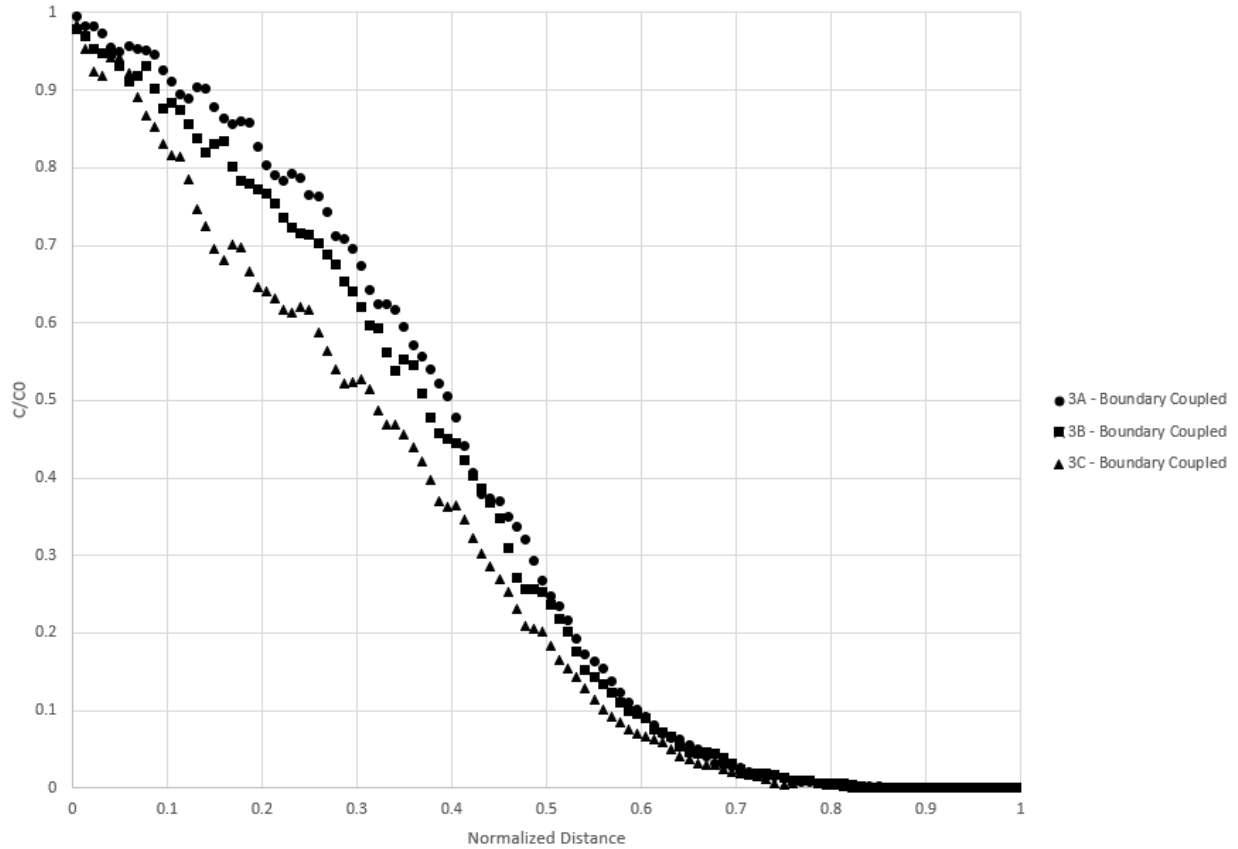


Figure 82. 7-micron particle species concentration profiles for 110 boundary coupled damaged Berea PNM baseline simulations for cases 3A, 3B and 3C.

With the baseline concentration curves obtained, 11-to-1 simulations were performed for cases 3A, 3B, and 3C. The results of these simulations are shown in Figure 83. For completeness, 5-to-1 simulations were also run for cases 3A, 3B, and 3C and are included in the result comparison. One hundred time steps were used for all concurrently coupled simulations and PNM properties were updated at each time step.

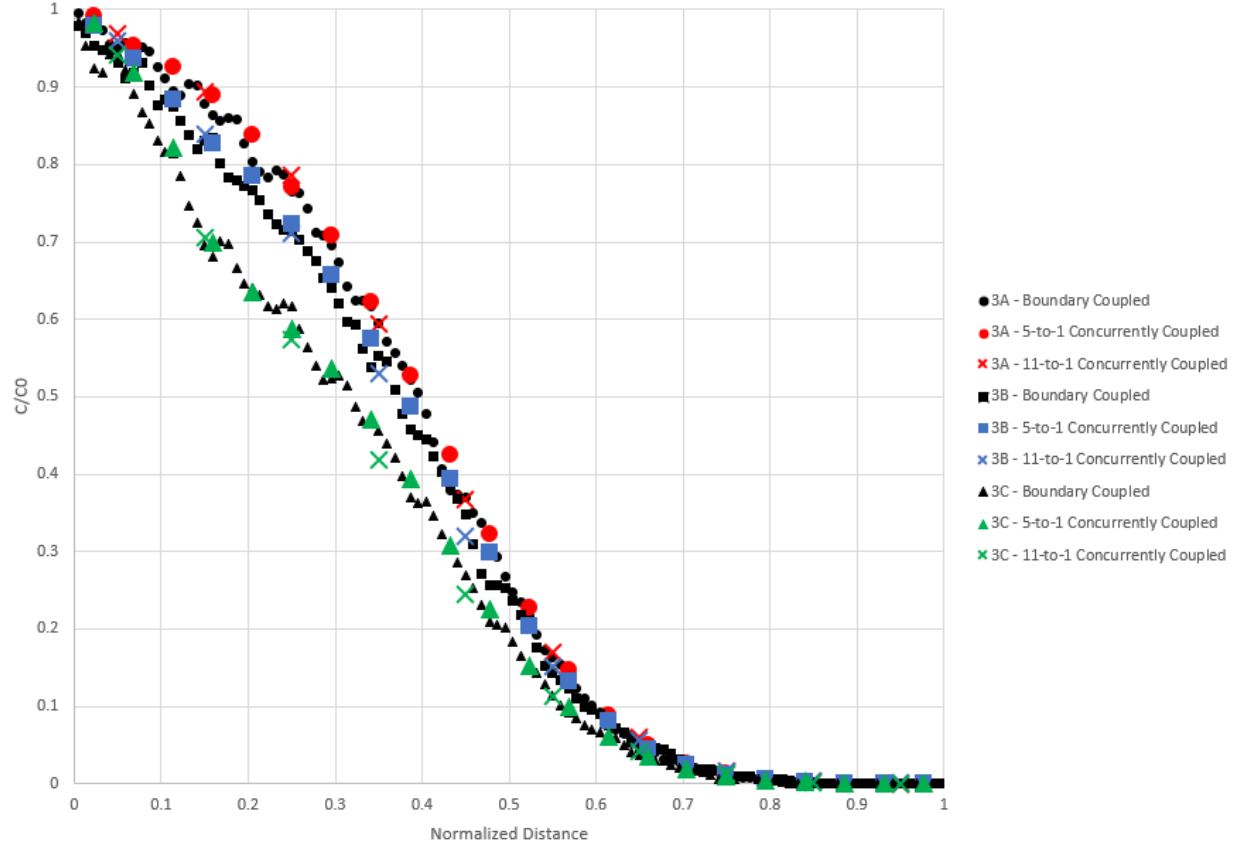


Figure 83. 10-micron concentration profile comparison of 11-to-1 and boundary coupled simulations for cases 3A, 3B, and 3C.

Overall, the 11-to-1 simulations compared favorably to the boundary coupled simulations. Each 11-to-1 concurrently coupled simulation followed closest to the boundary coupled simulation it represented. This indicates that the concurrently coupled model was able to incorporate pore-scale particle retention dynamics for a multi-particle system with an order-of-magnitude difference in the size of the embedded pore-scale models and finite difference grid blocks. The length of the systems for cases 3A, 3B, and 3C was 38.5 cm, a length on the order-of-magnitude of typical core samples. This result was significant in that it provided evidence that concurrently coupled models can be used to directly incorporate pore-scale effects in systems with sizes of practical interest. Furthermore, these results for the boundary coupled simulations were computationally demanding to obtain, taking around 36 hours. Although in some cases, the concurrently coupled simulations were even more computationally demanding, due to the fact that the PNM simulations were run in series. If performed in parallel, the PNM updates could be done rapidly and the concurrently coupled model would be much more efficient than the boundary coupled model. The results could not have been obtained by a traditional finite difference simulator, given the limitations of empirical models, to determine dynamic pore-scale properties. Therefore, the concurrently coupled model was demonstrated to simulate situations that alternative models could also do, but much more slowly at best, and at worst would be incapable of generating accurate simulations.

While the need to update grid block properties with PNMs was time consuming and led to some boundary coupled simulations being faster than the concurrently coupled simulations, the concurrently coupled model framework is ideally suited for parallel processing. At each time step, the number of particles that can enter each PNM can be quickly calculated and each PNM's grid block properties could be updated in parallel, since they are independent of each other. Thus, the PNM parameter updates do not scale with system size, making timely concurrently coupled simulations on systems of any size feasible, as long as enough memory can be obtained to store each PNM's data.

A sensitivity analysis was performed to define the effect of PNM property update frequency. To this end, 11-to-1 concurrently coupled simulations of case 3C were run with the number of times PNM property updates occurring during the simulation ranging from 0 to 100. Results of the simulations are shown in Figure 84.

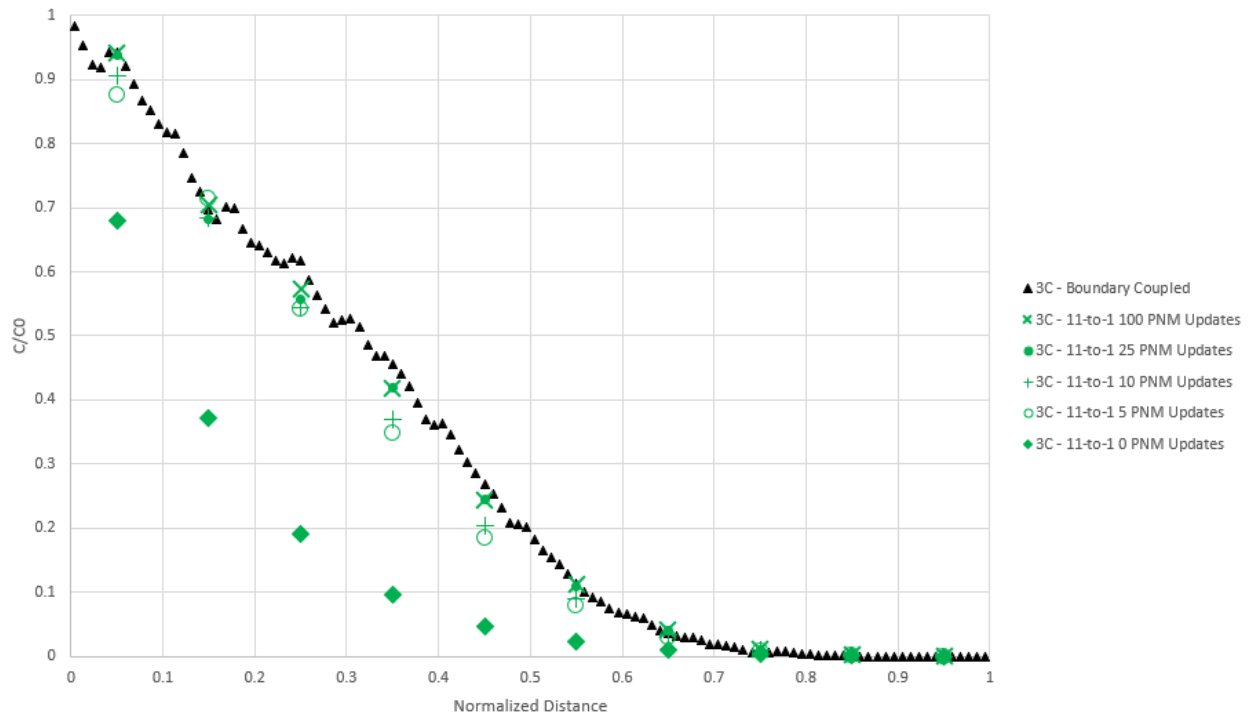


Figure 84. Sensitivity of concurrently coupled simulation results to PNM update frequency.

As in figure 83, 11-to-1 concurrently coupled simulation results converged to the baseline boundary coupled simulations. Updating the PNM property values 0 times, the equivalent of using constant grid block property values, resulted in a significantly reduced concentration profile. With no updates, the retention coefficients remain artificially high and are not reduced over time as particles become retained. Convergence towards the boundary coupled simulations occurred quickly, with significant improvements over constant coefficient values occurring with just 5 PNM updates, and nearly converged values after 25 PNM updates.



Although the concurrently coupled model is capable of running multi-species particle filtration simulations for cases with two orders of magnitude difference in size between embedded PNMs and finite difference grids, obtaining baseline results using boundary coupled models would be computationally prohibitive. For example, obtaining a baseline simulation for a 100-to-1 concurrently coupled model with 10 finite difference grid cells would have required a 1,000 PNM boundary coupled model. The issue compounds for multi-dimensional systems, where the same 100-to-1 size difference would require 100,000 boundary coupled PNMs for two-dimensional cases, and 10,000,000 boundary coupled PNMs for three-dimensional cases. The computational limitations of boundary coupled models for larger system sizes was one of the motivations for this work. Having demonstrated the capabilities of the concurrently coupled model in one-dimensional systems, the focus of this work was to demonstrate the potential of the concurrently coupled model for three-dimensional applications.

### 3.2. Three-Dimensional Concurrent Coupling

#### 3.2.1. Extension of One-Dimensional Model to Three Dimensions

The purpose of this work was to develop an enhanced model whose capabilities could provide simulation results which were unavailable from and superior to those generated by previous models. Consequently this would necessitate the use of experimental data for comparison and validation purposes. However, given that the objective of this work was to determine the viability of concurrently coupled models, such comparisons to experimental data were outside the scope of this work.

Modifications to the one-dimensional concurrently coupled simulator were made to make it compatible for three-dimensional simulations. The first adjustment made was to the evaluation of the number of influent particles used to damage a given PNM for a given time step (step 3 in Figure 29) for each of the 3 principal directions. Thus, equation 48 was modified to

$$N_{p,j,d} = C_{j-\ell_{PNM}/2,d} Q_d \Delta t \quad (49)$$

Where subscript  $d$  indicates each of the 3 principal flow directions,  $Q_d$  represents volumetric flow rate into the PNM in the direction  $d$ , and  $C_{j-\ell_{PNM}/2,d}$  (units of number of particles per volume) represents particle concentration in block  $j$  evaluated at the upwind face of the embedded PNM in the  $d$  flow direction. It is important to note that the cross-sectional area of the PNM in the three-dimensional simulations was not identical to that of the finite difference grid blocks, as was the case in the one-dimensional simulations. The volumetric flowrate into the PNM for a given flow direction,  $Q_d$ , was adjusted accordingly. In step 5 of the concurrently coupled simulator algorithm, the number of influent particles for each flow direction were injected into the PNM.

The second key adjustment to the concurrently coupled flow simulator occurred in step 6 of the simulator algorithm, in which PNM properties were determined. In this step, permeability was calculated for all 3 principal directions, and retention and dispersion coefficients were calculated in the principal flow direction with the largest magnitude of flow velocity in that grid block. Given that the PNM flow simulator used in this work was not designed to simulate flow through the PNM in a direction not aligned with one of the principal directions, this was an acceptable simplification.

This is not a limitation of PNMs in general and in principle longitudinal dispersion and retention coefficients could be determined along the exact flow direction. Given the absence of baseline results for comparison to the three-dimensional simulation results, the gain in coefficient accuracy was not considered necessary. Similarly, transverse dispersion coefficients were determined by assuming that they were 10% of the longitudinal dispersion coefficient for a given PNM, a reasonable assumption for the systems modeled in this work (Herrera, 2009).

### 3.2.2. Three-Dimensional Continuum-scale Concurrent Coupling

Pursuant to modifications made to enable the concurrently coupled model to operate in three dimensions, a realistic three-dimensional continuum-scale system was derived from the SPE 10 data set to test the model for a practical application. The designated application was that of a waterflood in a geospatially heterogeneous porous medium. As noted by Sharma et al. (1997), this application is highly relevant as there have been many reported instances of water well injectivity loss due to inadequate particle filtration at the surface, resulting in significant particle retention in the subsurface. The single phase nature of the concurrently coupled simulator used in this work is also appropriate for a waterflooding application.

To obtain a realistic permeability distribution at the continuum-scale, a three-dimensional system based on a 7 by 14 by 3 grid block subset of the SPE 10 data set was generated. The selected subset contains the cells from (29, 144, 7) to (36, 158, 10) of the SPE 10 data set. This subset was selected because it has a wide permeability range spanning two orders of magnitude and has well defined geologic features, such as diagonally segregated areas of high and low permeability in the upper layer of the subset. Given that each grid block had dimensions of 20 by 10 by 3 ft, using a 7 by 14 system in the X and Y directions resulted in a square domain in the XY plane. For reference, compared to the embedded PNMs, the finite difference grid blocks were 1,741 times larger in length in the X direction, 870 times larger in Y and 268 times larger in Z.

To limit the number of PNMs needed to initiate the three-dimensional simulations, the permeability values of each grid block in the subset were assigned to one of ten values. The selected permeability values were 10, 25, 50, 100, 200, 300, 400, 500, 750, and 1000 md. The smoothed Berea PNM, with an original permeability value of 418md, was adjusted by altering the radii of all throats in the network by a fixed multiplier until a PNM was obtained for each of the 10 desired permeability values. Relevant parameters such as throat cross sectional area and hydraulic conductance were adjusted accordingly for each PNM. The throat radii multiplier used for each of the 10 PNMs is provided in Table 24.

Table 24. Ten permeability values for three-dimensional simulation PNMs and corresponding radii multipliers.

<b>Permeability (md)</b>	<b>10</b>	<b>25</b>	<b>50</b>	<b>100</b>	<b>200</b>	<b>300</b>	<b>400</b>	<b>500</b>	<b>750</b>	<b>1000</b>
<b>Radii multiplier</b>	0.38	0.48	0.57	0.68	0.81	0.89	0.96	1.01	1.12	1.20

Permeability values for the subset were assigned from the values in Table 24 according to the value with the lowest absolute difference to the original permeability value in the X direction. Figure 85 provides permeability heat maps of the three layers in the three-dimensional subset after assignment to one of the 10 values (values in md).

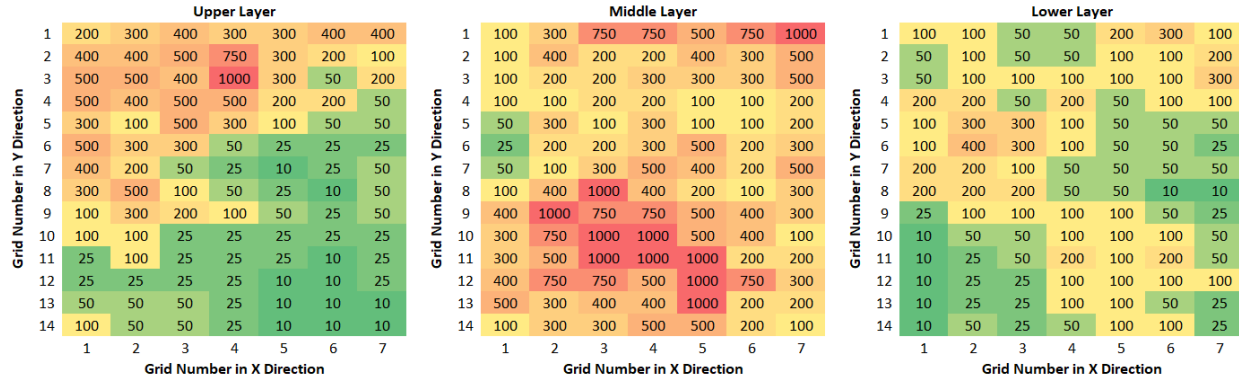


Figure 85. Permeability heat map for three-dimensional subset (values in md).

A single Berea PNM was embedded into each grid block with an initial permeability value equal to that of the mapping from the SPE 10 data subset depicted in Figure 85. It should be noted that the Y and Z permeability values of the three-dimensional subset used in this work were derived from the embedded PNMs and were not set to match those in the original SPE 10 data set. In a more realistic scenario with unique petrophysical parameter values in each grid block and possibly different lithologies, PNMs derived from representative core samples could be used to initialize the concurrently coupled model.

For the three-dimensional flow simulations a water injection well was placed in the upper right corner of the model and allowed to communicate with the system in all 3 layers. A fixed injection rate boundary condition of 5,000 bbl/day was applied to the system. For simplicity the injected fluid was evenly distributed into the three layers such that each of the three upper corner grid cells, (7,1,1), (7,1,2) and (7,1,3) had a boundary condition of 1666.67 bbl/day. To mimic a system under radial flow, no flow boundaries were assigned to the upper XY plane (Z=1), lower XY plane (Z=3), lower XZ plane (Y=1), and upper XZ plane (X=7). The remaining external boundaries, lower YZ plane (X=1) and upper XZ plane (Y=14), were assigned pressure values based on the radial solution to Darcy's law

$$p_b(r_b, t) = p_0 - \frac{Q\mu}{4\pi kh} Ei \left( -\frac{r_b^2 \phi \mu c_t}{4tk} \right) \quad (26)$$

where  $p_b$  is pressure at the external boundary face,  $r_b$  is the equivalent radius to the boundary face (computed from the equivalent circular area of the XY plane),  $Ei$  is the exponential integral function,  $p_0$  is the initial pressure (set to 6000 psi in all three-dimensional simulations),  $Q$  is injection flow rate,  $\mu$  is fluid viscosity (1 cp in all simulations),  $k$  represents median permeability in each layer,  $\phi$  is average layer porosity,  $c_t$  is total compressibility (set to 1E-6 psi<sup>-1</sup> in all three-dimensional simulations), and  $t$  is time. Pressure boundary conditions were evaluated for each

time step and incorporated permeability changes due to particle trapping. Although setting the pressure boundaries in this way biases flow towards lower permeability regions, it was applied consistently in all simulations and therefore enabled for valid comparisons of different simulation runs in which the only changing parameter was the particle species injected.

The remaining parameter needed to initiate flow simulations was an appropriate particle concentration and size range to inject into the system. Sharma et al. (1997) indicated in their Gulf of Mexico waterflooding case study that the well operator had filtered the injected water to 5 microns but later switched to 10-micron filters because of operational cost. Thus, an appropriate particle range for the three-dimensional simulations in this work was determined to be between 1 and 10 microns. Sharma et al. (1997) also cited particle concentrations ranging from 1 to 7 mg/L with a median value of about 3 mg/L. Assuming the median concentration value of 3 mg/L, a particle density equivalent to sandstone (2.65 g/cc), and 5-micron-diameter particles (middle of previously explained range), the total number of particles entering the system per day is  $2.44 \times 10^{13}$ . When the size differential of the PNMs to the finite difference grid blocks is taken into account, this corresponds to 60,080 particles per day or 84,620 particles per system pore volume passing through a given PNM. Considering the previous simulations with relatively high numbers of trapped particles involved 100,000 – 200,000 total injected particles, the concentration boundary condition was determined to be feasible. To allow the same number of particles to be injected for the subsequent three-dimensional A/B simulations involving different particle sizes, all simulations used the aforementioned concentration boundary condition.

The first three-dimensional simulation performed was to evaluate the concentration field of solute particles after one pore system pore volume of injection. This provided context to subsequent simulations with particle retention. Given the injection rate, one system pore volume of injection occurred at 0.71 days. The resulting solute concentration field in the three-dimensional system after one system pore volume of injection is provided in Figure 86.

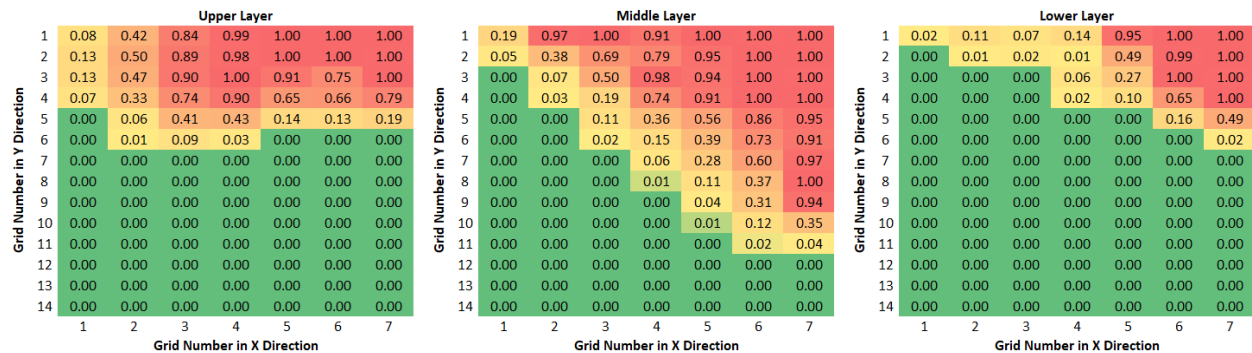


Figure 86. Solute concentration field after 1.0 system pore volumes injected.

The solute concentration field was different for each layer. In the upper layer, the solute particles remained in the lower half of the system in the Y direction due to the low permeability values in the upper half of the system in the Y direction. In the middle layer permeability values were higher on average and there was no distinct pattern in the permeability map. This resulted in fairly even radial spreading of the concentration field in the middle layer. The lower layer was similar to the

upper layer in that there was a flow bias in the X direction, however permeability values were lower on average so the concentration field developed more slowly.

A series of simulations were subsequently performed with uniform particle size distributions. Particle sizes were increased from 2 to 5 microns in diameter and concentration fields were recorded after one system pore volume. A simulation for 1-micron-diameter particles was omitted because these particles exhibited negligible retention and were thus effectively the same as solute particles for this system. Results of the concentration field for each particle size are provided in figures 87-90. Each simulation used 500 time steps and updated PNM properties a total of 10 times.

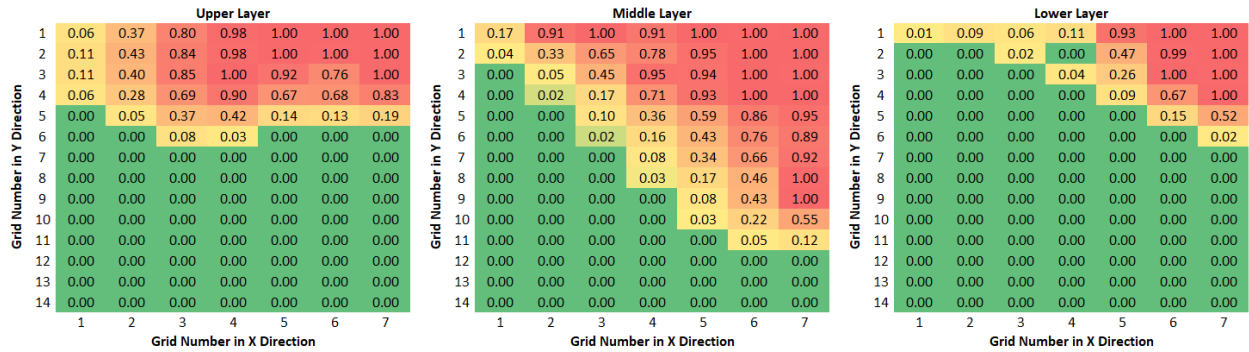


Figure 87. 2-micron-diameter particle concentration field after 1.0 system pore volumes injected.

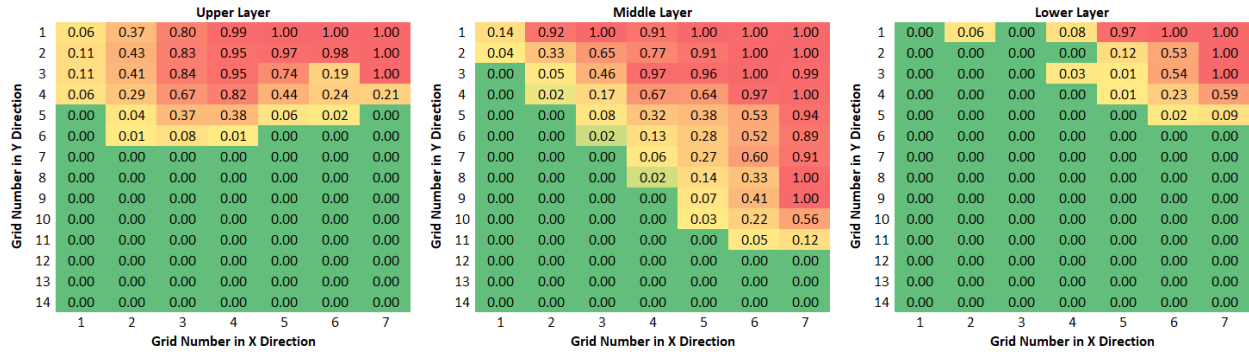


Figure 88. 3-micron-diameter particle concentration field after 1.0 system pore volumes injected.

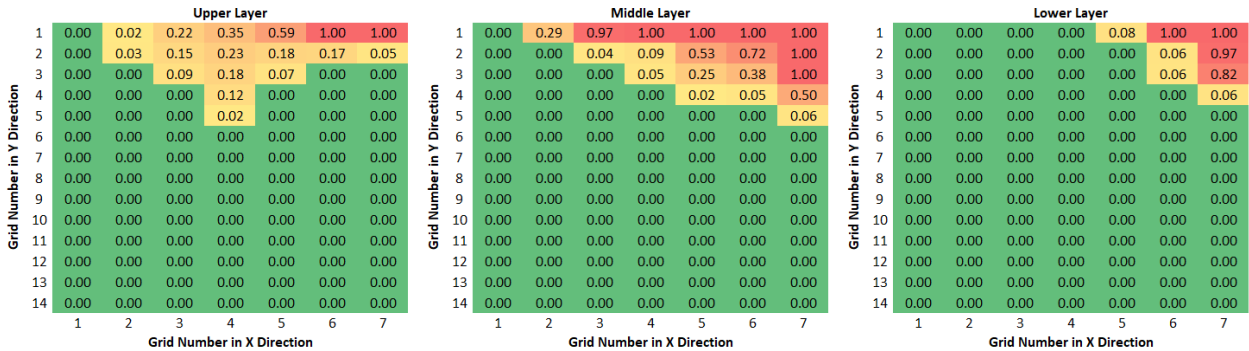


Figure 89. 4-micron-diameter particle concentration field after 1.0 system pore volumes injected.

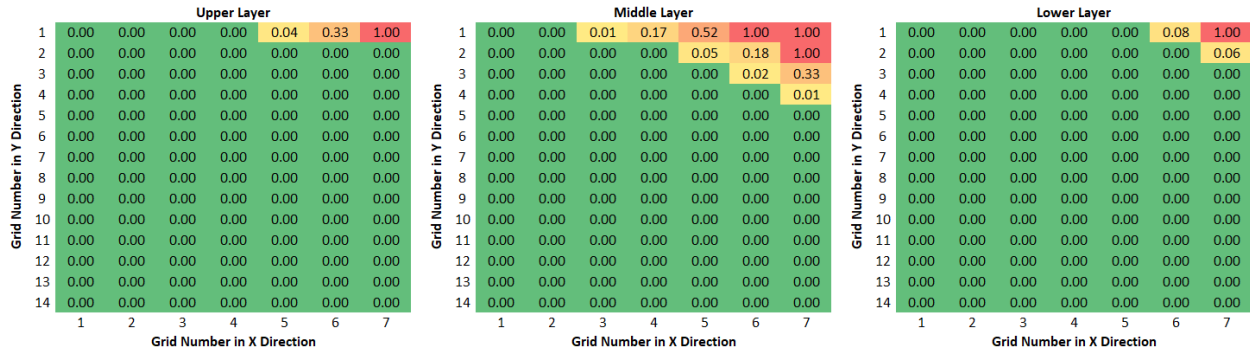


Figure 90. 5-micron-diameter particle concentration field after 1.0 system pore volumes injected.

The ability for particles to travel significant distances into the three-dimensional system was seen to diminish rapidly as particle size increased beyond 3 microns in diameter. Table 25 shows the percent of 5-micron-diameter particles that could pass through each of the 10 PNMs that made up the three-dimensional system. Even in the limited transport case of 5-micron-diameter particles, it can be inferred that a high percent of particles passed through each PNM during the simulation.

Table 25. Percent of 5-micron-diameter particles that pass through each PNM in the three-dimensional system.

PNM Permeability (md)	10	25	50	100	200	300	400	500	750	1000
% 5-micron diameter particles passed	0.6	38.3	51.3	90.5	98.1	99.4	99.6	99.8	99.9	99.9

Small amounts of retention over large distances can result in limited overall system transport. With only relatively small particles capable of significant transport in the three-dimensional continuum-scale system used in this work, minimal changes were observed in permeability and porosity. For example, the most severely damaged grid blocks in the 5-micron-diameter particle simulation (the grid blocks where particle injection was occurring) showed a reduction in permeability less than 0.5% from their original value.

Although there were limited changes in permeability and porosity, retention coefficients in the three-dimensional simulations changed significantly from the beginning of a given simulation to the end. Figures 91-94 depict the reduction of retention coefficient for each single particle size simulation. Values of 0.0 indicate that no reduction in retention coefficient occurred, while values of 1.0 indicate that the retention coefficient was reduced to zero, and values of N/A indicate that the retention coefficient for that particle size in that grid block was initially zero, and could therefore not be reduced.

For the case of 2-micron-diameter particles, particles exhibited no retention for the majority of grid cells. This was reflected by the high degree of similarity between the solute concentration field and the 2-micron-diameter particle concentration field. In general as particle sizes increased, fewer grid cells had initial retention coefficients of zero, and more grids exhibited large degrees of



alteration in retention coefficient. These large alterations in retention coefficient resulted in complex transport behavior and the different concentration profiles between the various cases. From a practical standpoint, the results of these simulations could be used to indicate that, for this system, significant amounts of particles will become retained over time, if the injected water is not filtered to remove particles larger than 4 microns in diameter. A finer scale model of the system could be made to perform a further analysis closer to the wellbore where the damage would be localized. Alternatively, these results could be used to indicate that for a species intended to penetrate deep into the three-dimensional system, such as a conformance control agent, it must be about 4 microns in diameter or smaller to have a significant impact.

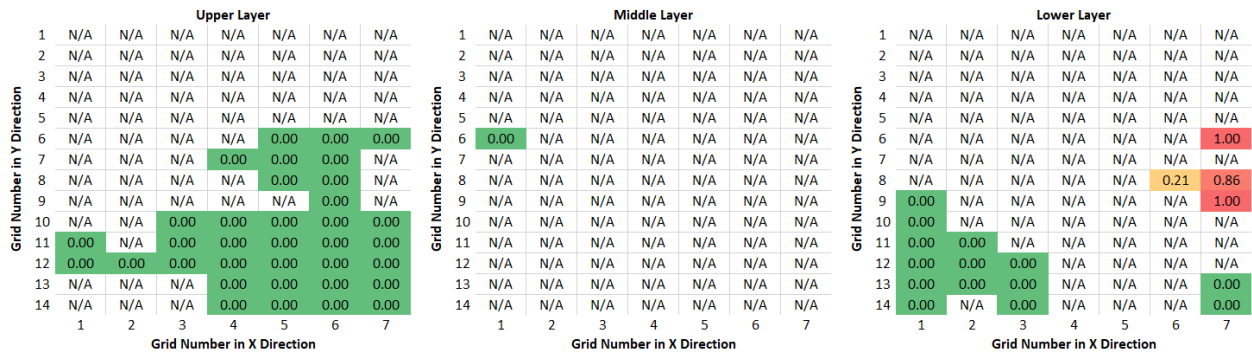


Figure 91. 2-micron-diameter particle retention coefficient reduction.



Figure 92. 3-micron-diameter particle retention coefficient reduction.

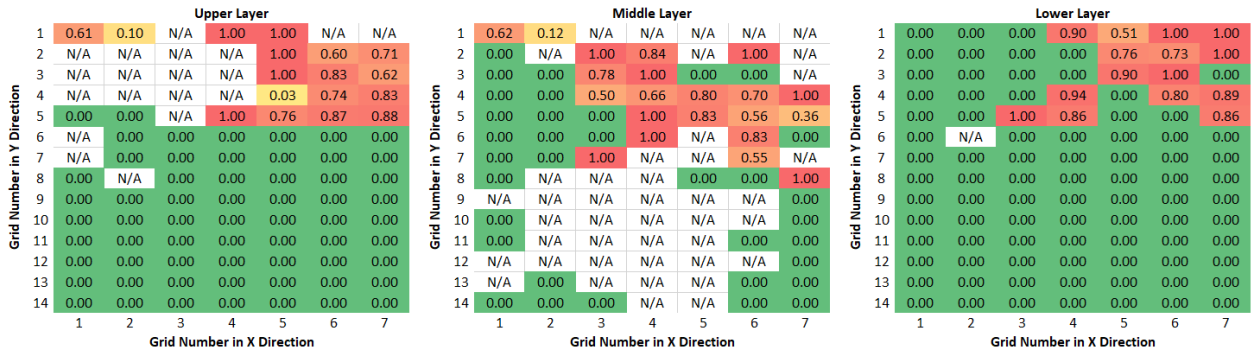


Figure 93. 4-micron-diameter particle retention coefficient reduction.



Figure 94. 5-micron-diameter particle retention coefficient reduction.

A final A/B simulation was performed to demonstrate the multispecies capabilities of the concurrently coupled model in a three-dimensional system and in turn the benefit of operating a concurrently coupled model. For the A/B simulation a random mix of 3- and 4-micron-diameter particles was injected in the three-dimensional system over 1.0 system pore volumes. The injected concentration of each particle species was reduced by half relative to that in the single species simulations so that the combined total concentration was equivalent to that of the single species simulations. Concentration maps for the 3- and 4-micron-diameter species at the end of the mixed injection simulation are provided in Figures 95 and 96. Concentration fields for the 3- and 4-micron-diameter single species injection cases are included for comparison.



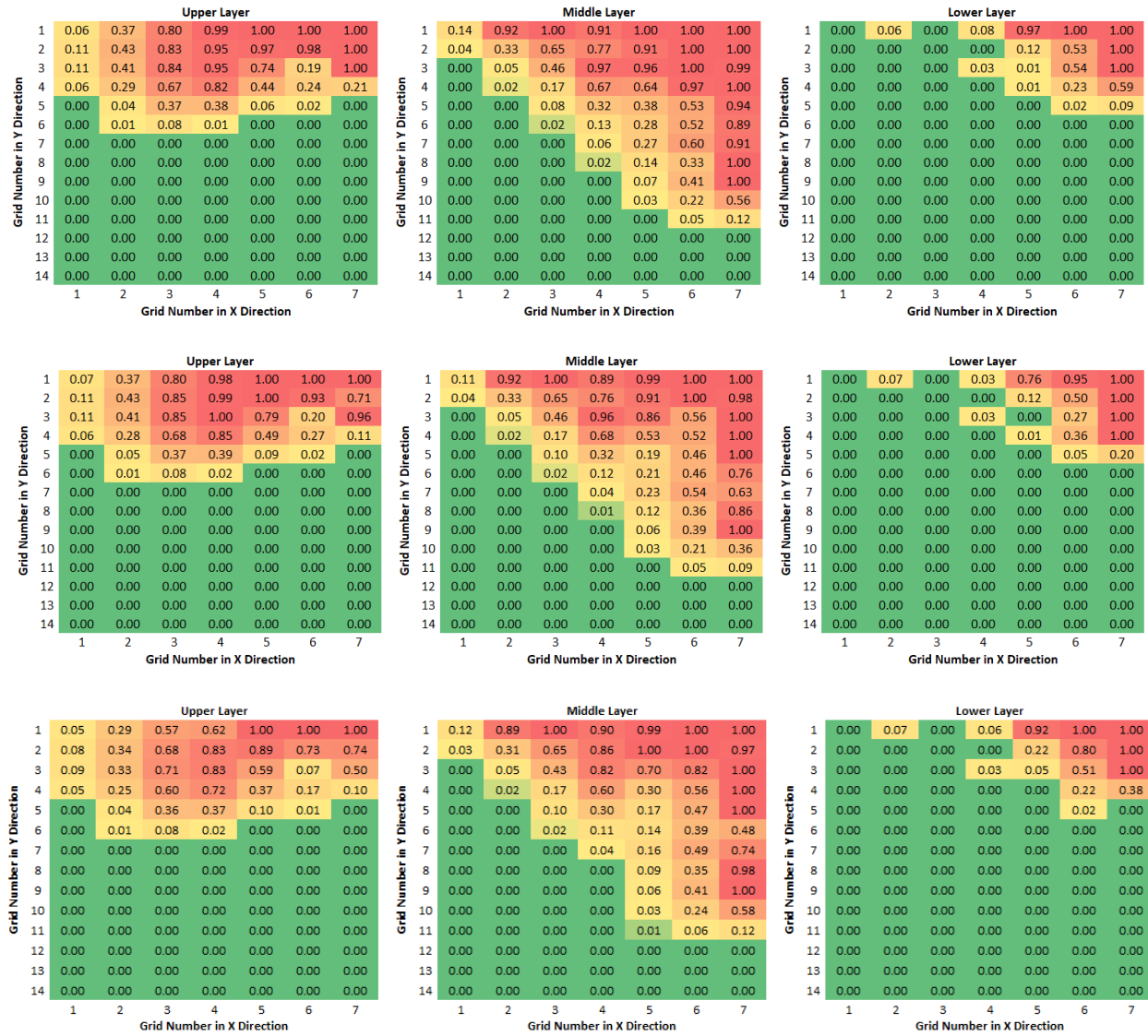


Figure 95. 3-micron-diameter particle concentration fields for single species (top), mixed species (middle), and 4-micron followed by 3-micron (bottom) cases.

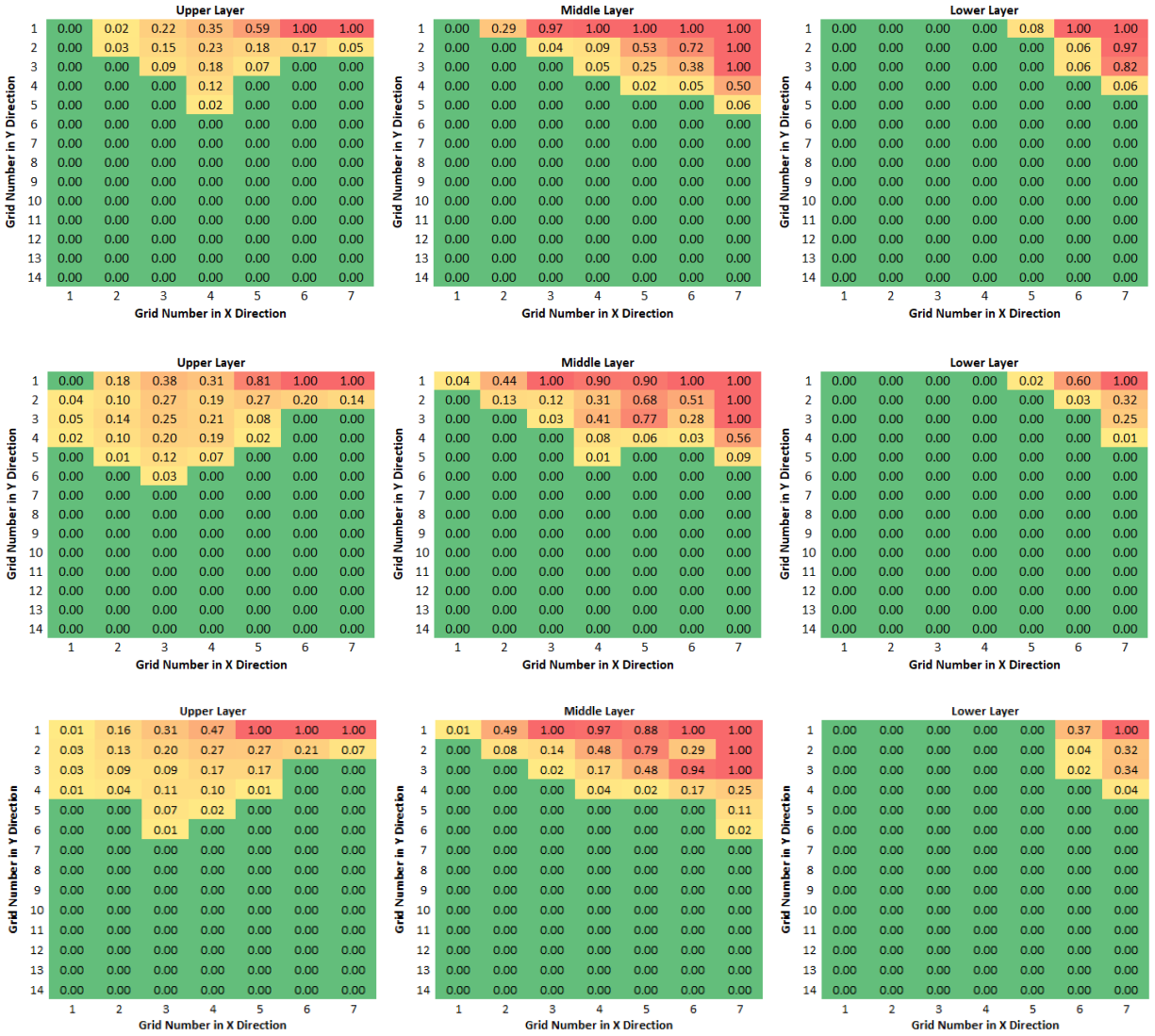


Figure 96. 4-micron-diameter particle concentration fields for single species (top), mixed species (middle), and 3-micron followed by 4-micron (bottom) cases.

The concentration field for the 3-micron-diameter particles species in the single species case did not differ greatly from that in the mixed 3- and 4-micron case. However, the concentration field for the 4-micron-diameter particles species in the single species case did differ noticeably from that in the mixed 3- and 4-micron case. The difference for the 4-micron-diameter particle concentration maps was most significant in the upper layer, where the mixed case resulted in more particle spreading than the single 4-micron species case. This matches qualitatively with the experimental work of Xu and Saiers (2009), who also noted lessened retention of a larger species when injected with a smaller species compared to a monodisperse injection of the larger species.

These results indicate that the concurrently coupled model was capable of identifying differences in particle transport and retention behavior for multi-species particle systems at the continuum-scale. These differences were determined by incorporating dynamic pore-scale processes in a continuum-scale model, the primary objective of this work. Due to the fact that the model was

flexible, any number of particle species and ratios thereof could have been simulated. The simulations were also able to run in about 10 hours, an acceptable amount of time, demonstrating computational efficiency. Computational time constraints were evident in that only 10 updates were made to the PNMs during the running of the simulations, however running the PNM updates in parallel rather than in series would result in a significant reduction in simulation time. More realistic continuous distributions of particle sizes could also be simulated, with acceptable simulation times and accuracy, by grouping particles of a similar size into species with averaged retention and dispersion coefficients.

## Conclusion

As demonstrated in previous experimental work and in the numerical simulations of this work, in systems where size exclusion is the dominant retention mechanism, particle size distribution and concentration have significant impacts on particle transport behavior. As a consequence of these pore-scale effects, the formulation of accurate continuum-scale particle filtration models has proved to be challenging. While phenomenological models for monodisperse and bidisperse systems have been developed, these models have limited flexibility and practical utility. These limitations arise from the models being dependent on empirical parameters, the generation of which requires experimental or numerical data that is time consuming to obtain. This work developed a continuum-scale model for particle transport and retention consisting of a traditional finite difference model concurrently coupled to pore-scale network models. Dynamically updating system properties with values obtained from embedded pore-scale models was shown to enable a relatively simple single-coefficient retention model to accurately and flexibly model complex particle transport behavior at the continuum-scale.

Application of the concurrently coupled model developed in this work led to additional findings, including the determination that the methodology used to upwind parameters at the embedded pore-scale model's boundary can have a significant impact on model behavior. Effective porosity was also shown to change due to particle filtration, and its potential impacts on determining particle concentrations was investigated. A key feature of the concurrently coupled model developed in this work was a robust methodology for determining pore-scale parameter values. Determining dynamic parameter values, such as the retention coefficient, at fixed points in time rather than using time averaged values was shown to enable frequent parameter updates and high accuracy of modeled transport behavior. Numerical simulation was shown to be advantageous relative to experimental methods for determining pore-scale parameter values. This was due to the ability of numerical simulation to investigate the effects, such as particle trapping, on a given system without altering that system.

The concurrently coupled model provided accurate simulation results for both monodisperse and bidisperse particle systems. Simulated results from both the monodisperse and bidisperse systems qualitatively matched those of experimental data. Accurate simulations were achieved without the use of experimentally derived empirical coefficients required by standard models. Thus, the model developed in this work was shown to be flexible and had practical utility. Additionally, the model accurately simulated particle transport in systems with greater than an order-of-magnitude size discrepancy between the embedded pore-scale network models and finite difference grid cells. Although the accuracy of the model could not be validated for larger continuum-scale systems due to the computational limitations of pore-scale models, and lack of experimental data, the model was capable of analyzing a realistic three-dimensional continuum-scale scenario.

Future work could further expand the utility of concurrently coupled models for particle transport and retention. Implementation of parallel processing to obtain updated parameters from embedded pore-scale models would significantly improve the computational efficiency relative to the series update methodology used in this work. If implemented, parallel computation could potentially allow for the simulation of a wide range of inputs to develop more robust empirical models or tabulations for coefficient values prior to running the concurrently coupled model. A useful

continuation of this work would be to investigate the accuracy of concurrently coupled models for particle transport in three-dimensional continuum-scale systems through comparisons to experimental work. Future work could incorporate pore-scale models with additional retention mechanisms such as adsorption and gravity settling. The use of alternate continuum-scale models, such as those using irregular frameworks, could also be investigated. Additionally, the model could be extended to multiphase and polydisperse particle systems. This work demonstrated that concurrently coupled models can accurately account for dynamic pore-scale phenomenon. Therefore, the methodology could be utilized for the investigation of a wide range of applications involving dynamic pore-scale phenomenon that impact continuum-scale systems, such as matrix acidization and wettability alteration.

## Appendix. Supplementary Input Data File for Chapter 3

```
** *****
**
** *IO
**
** *****
**
RESULTS SIMULATOR IMEX 201410

*INUNIT *FIELD
*OUTSRF *GRID *SEAWF
*****
**
**          *GRID
**
*****

*GRID *VARI 20 1 1
*KDIR *DOWN
*DI *IVAR
20*0.011489502

*DJ *JVAR
1*0.011489502
*PERMI *ALL
20*521
*PERMJ *ALL
20*521
*DK *ALL
20*0.007447901

*POR *ALL
20*0.1524
PERMK EQUALSI
** 0 = pinched block, 1 = active block
PINCHOUTARRAY CON      1
*DEPTH-TOP *ALL
20*4000
** 0 = null block, 1 = active block
NULL CON      1

*CROCKTYPE 1
*CCPOR 0.000003
*CPRPOR 4000

*****
**
**          *MODEL
**
*****

*MODEL *OILWATER_SEAWATER
```

```

*DENSITY *OIL 52.0000
*DENSITY *GAS .04400
*DENSITY *WATER 64.0000
*PVT BG 1
0 0 1.0 .1757549 2.5 0.00790592
1000 0.0000000001 1.0 .17575489 2.5 0.007905921
*BOT 1
0 1
8000 0.999
*VOT 1
0 1.
8000 1.
*REFPW 0
*BWI 1
*CW 0.00000303
*VWI 1.0
*CVW 0
*SVISC 1.
*****
**
**          *ROCKFLUID
**
*****

*ROCKFLUID

*KROIL *SEGREGATED
*RPT 1
*SWT
0. 0.0 1 0
1. 1 0 0

*SGT
0. 0.0 1 0 0
1. 1 0.0 0 0

*****
**
**          *INITIAL
**
*****

*INITIAL
*VERTICAL *BLOCK_CENTER *WATER_OIL
*REFDEPTH 4000
*REFPRES 4000
*DWOC 1000
*PB *CON 0

NUMERICAL
*DTMAX 0.000005863739
*DTMIN 0.000005863739

```

```
*****
**
**      *RUN
**
*****
```

```
*RUN
*DATE 2011 1 1
GROUP 'G' ATTACHTO 'FIELD'
*WELL 'I' *ATTACHTO 'G'
INJECTOR MOBWEIGHT 'I'
INCOMP SEAWATER
OPERATE MAX STW 0.000431995 CONT
OPERATE MAX BHP 100000.0 CONT
```

```
*XFLOW-MODEL 'I' *FULLY-MIXED
*WELL 'P' *ATTACHTO 'G'
PRODUCER 'P'
OPERATE MIN BHP 3999.0 CONT
*BHPDEPTH 'P' 4000.0
*XFLOW-MODEL 'P' *FULLY-MIXED
**      rad geofac wfrac skin
GEOMETRY K 0.000382983 0.56 0.25 0.0
      PERF      GEOA 'I'
** UBA      ff      Status Connection
      1 1 1      1.0 OPEN FLOW-FROM 'SURFACE'
**      rad geofac wfrac skin
GEOMETRY K 0.000382983 0.56 0.25 0.0
      PERF      GEOA 'P'
** UBA      ff      Status Connection
      20 1 1      1.0 OPEN FLOW-TO 'SURFACE'
*BHPDEPTH 'I' 4000.0
```

```
DATE 2011 1      1.000005863739
DATE 2011 1      1.000011727477
DATE 2011 1      1.000017591216
DATE 2011 1      1.000023454954
DATE 2011 1      1.000029318693
DATE 2011 1      1.000035182431
DATE 2011 1      1.000041046170
DATE 2011 1      1.000046909908
DATE 2011 1      1.000052773647
DATE 2011 1      1.000058637386
DATE 2011 1      1.000064501124
DATE 2011 1      1.000070364863
DATE 2011 1      1.000076228601
DATE 2011 1      1.000082092340
DATE 2011 1      1.000087956078
DATE 2011 1      1.000093819817
DATE 2011 1      1.000099683555
DATE 2011 1      1.000105547294
DATE 2011 1      1.000111411033
DATE 2011 1      1.000117274771
```



DATE 2011 1	1.000123138510
DATE 2011 1	1.000129002248
DATE 2011 1	1.000134865987
DATE 2011 1	1.000140729725
DATE 2011 1	1.000146593464
DATE 2011 1	1.000152457202
DATE 2011 1	1.000158320941
DATE 2011 1	1.000164184680
DATE 2011 1	1.000170048418
DATE 2011 1	1.000175912157
DATE 2011 1	1.000181775895
DATE 2011 1	1.000187639634
DATE 2011 1	1.000193503372
DATE 2011 1	1.000199367111
DATE 2011 1	1.000205230849
DATE 2011 1	1.000211094588
DATE 2011 1	1.000216958327
DATE 2011 1	1.000222822065
DATE 2011 1	1.000228685804
DATE 2011 1	1.000234549542
DATE 2011 1	1.000240413281
DATE 2011 1	1.000246277019
DATE 2011 1	1.000252140758
DATE 2011 1	1.000258004496
DATE 2011 1	1.000263868235
DATE 2011 1	1.000269731974
DATE 2011 1	1.000275595712
DATE 2011 1	1.000281459451
DATE 2011 1	1.000287323189
DATE 2011 1	1.000293186928
DATE 2011 1	1.000299050666
DATE 2011 1	1.000304914405
DATE 2011 1	1.000310778143
DATE 2011 1	1.000316641882
DATE 2011 1	1.000322505621
DATE 2011 1	1.000328369359
DATE 2011 1	1.000334233098
DATE 2011 1	1.000340096836
DATE 2011 1	1.000345960575
DATE 2011 1	1.000351824313
DATE 2011 1	1.000357688052
DATE 2011 1	1.000363551790
DATE 2011 1	1.000369415529
DATE 2011 1	1.000375279268
DATE 2011 1	1.000381143006
DATE 2011 1	1.000387006745
DATE 2011 1	1.000392870483
DATE 2011 1	1.000398734222
DATE 2011 1	1.000404597960
DATE 2011 1	1.000410461699
DATE 2011 1	1.000416325437
DATE 2011 1	1.000422189176
DATE 2011 1	1.000428052915

DATE 2011 1	1.000433916653
DATE 2011 1	1.000439780392
DATE 2011 1	1.000445644130
DATE 2011 1	1.000451507869
DATE 2011 1	1.000457371607
DATE 2011 1	1.000463235346
DATE 2011 1	1.000469099084
DATE 2011 1	1.000474962823
DATE 2011 1	1.000480826562
DATE 2011 1	1.000486690300
DATE 2011 1	1.000492554039
DATE 2011 1	1.000498417777
DATE 2011 1	1.000504281516
DATE 2011 1	1.000510145254
DATE 2011 1	1.000516008993
DATE 2011 1	1.000521872731
DATE 2011 1	1.000527736470
DATE 2011 1	1.000533600209
DATE 2011 1	1.000539463947
DATE 2011 1	1.000545327686
DATE 2011 1	1.000551191424
DATE 2011 1	1.000557055163
DATE 2011 1	1.000562918901
DATE 2011 1	1.000568782640
DATE 2011 1	1.000574646378
DATE 2011 1	1.000580510117
DATE 2011 1	1.000586373856
STOP	

RESULTS SPEC 'Permeability K'  
 RESULTS SPEC SPECNOTCALCVAL -99999  
 RESULTS SPEC REGION 'All Layers (Whole Grid)'  
 RESULTS SPEC REGIONTYPE 'REGION\_WHOLEGRID'  
 RESULTS SPEC LAYERNUMB 0  
 RESULTS SPEC PORTYPE 1  
 RESULTS SPEC EQUALSI 0 1  
 RESULTS SPEC SPECKEEMOD 'YES'  
 RESULTS SPEC STOP

**Figure A1. CMG simulation input file for numerical dispersion comparison**

## References

- Abou-Kassem, J. H., Farouq Ali, S.M., and Islam, M. R., 2006, Petroleum Reservoir Simulation - A Basic Approach: Gulf Publishing Company.
- Acharya, R. C., Van der Zee, S. E. A. T. M., and Leijnse, A., 2005, Transport modeling of nonlinearly adsorbing solutes in physically heterogeneous pore networks: *Water Resour. Res.*, v. 41, W02020.
- Ahrenholz, B., Tölke, J., and Krafczyk, M., 2006, Lattice-Boltzmann simulations in reconstructed parametrized porous media: *Int. J. Comput. Fluid Dyn.*, v. 20, no. 6, p. 369–377.
- Al-Raoush, R., Thompson, K. E., and Willson, C. S., 2003, Comparison of network generation techniques for unconsolidated porous media: *Soil Science Society of America Journal*, v. 67, no. 6, p. 1687–1700.
- Arns, C. H., Bauget, F., Limaye, A., Sakellariou, A., Senden, T. J., Sheppard, A. P., Sok, R. M., Pinczewski, W., Bakke, S., Berge, L. I., Øren, P.-E., and Knackstedt, M. A., 2004, Pore Scale Characterisation of Carbonates Using X-ray Microtomography, Society of Petroleum Engineers.
- Baghdikian, S. Y., Sharma, M. M., and Handy, L. L., 1989, Flow of Clay Suspensions Through Porous Media, Society of Petroleum Engineers.
- Balhoff, M. T., Thompson, K. E, and Hjortsø, M., 2007, Coupling pore networks to continuum Models: *Comput. Geosci.*, v. 33, no. 3, p. 393–410.
- Balhoff, M. T., Thomas, S. G., and Wheeler, M. F., 2008, Mortar coupling and upscaling of pore-scale models: *Comput. Geosci.*, v. 12, no. 1, p. 15-27.
- Battiato, I., Tartakovsky, D. M., Tartakovsky, A. M., and Scheibe, T. D., 2011, Hybrid models of reactive transport in porous and fractured media: *Advances in Water Resources*, v. 34, no. 9, p. 1140-1150.
- Bear, J., 1972, Dynamics of Fluids in Porous Media: Dover Publications, Inc., New York.
- Bear, J., 1979, Hydraulics of Groundwater: McGraw-Hill, New York, p.210.
- Bera, A., and Belhaj, H., 2016, Application of nanotechnology by means of nanoparticles and nanodispersions in oil recovery - a comprehensive review: *J. Nat. Gas Sci. Eng.*, v. 34, p. 1284–1309.
- Bhattad, P., Willson, C., and Thompson, K., 2011, Effect of Network Structure on Characterization and Flow Modeling Using X-ray Micro-Tomography Images of Granular and Fibrous Porous Media: *Transport in Porous Media*, v. 90, no. 2, p. 363-391.

- Bijeljic, B., and Blunt, M. J., 2007, Pore-scale modelling of transverse dispersion in porous Media: *Water Resour. Res.*, v. 43, W12S11.
- Bijeljic, B., Muggeridge, A. H., and Blunt, M. J., 2004, Pore-scale modeling of longitudinal dispersion: *Water Resour. Res.*, v. 40, W11501.
- Blunt, M. J., Bijeljic, B., Dong, H., Gharbi, O., Iglauer, S., Mostaghimi, P., Paluszny, A., and Pentland, C., 2013, Pore-scale imaging and modeling: *Adv. Water Resour.*, v. 51, p. 197-216.
- Blunt, M. J., Jackson, M. D., Piri, M., and Valvatne, P. H., 2002, Detailed physics, predictive capabilities and macroscopic consequences for pore-network models of multiphase flow: *Adv. Water Resour.*, v. 25, no. 8–12, p. 1069–1089.
- Bouwer, H., 1984, Elements of soil science and groundwater hydrology: *Groundwater Pollution Microbiology*, pp. 9-38.
- Bradford, S. A., J. Simunek, M. Bettahar, M. T. van Genuchten, and S. R. Yates, 2006, Significance of straining in colloid deposition: Evidence and implications, *Water Resour. Res.*, v. 42.
- Bruderer, C., and Bernabé, Y., 2001, Network modeling of dispersion: Transition from Taylor dispersion in homogeneous networks to mechanical dispersion in very heterogeneous ones: *Water Resour. Res.*, v. 37, p. 897–908
- Bryant, S. L., and M. Blunt, 1992, Prediction of relative permeability in simple porous media: *Physical Review A*, v. 46, no. 4, p. 2004-2011.
- Bryant S. L., Cade, C. A., and Mellor, D. W., 1993a, Permeability prediction from geologic models: *AAPG Bull.*, v. 77, no. 8, p. 1338–1350.
- Bryant, S. L., King, P. R., and Mellor, D. W., 1993b, Network model Evaluation of permeability and spatial correlation in a real random sphere packing: *Transp. Porous Media*, v. 11, p. 53-70.
- Bryant, S. L., Mellor, D. W., and Cade, C. A., 1993c, Physically representative network models of transport in porous media: *AIChE J.*, v. 39, no. 3, p. 387-396.
- Bryntesson, L. M., 2002, Pore network modelling of the behaviour of a solute in chromatography media: Transient and steady-state diffusion properties: *J. Chromatogr. A*, v. 945, no. 1, p. 103–115.
- Celia, M. A., Rajaram, H., and Ferrand, L. A., 1993, A multi-scale computational model for multiphase flow in porous media: *Advances in Water Resources*, v. 16, no. 1, p. 81-92.

- Chen, Z., 2007, *Reservoir Simulation: Mathematical Techniques in Oil Recovery*: Society for Industrial and Applied Mathematics.
- Chen, C., Packman, A. I., Zhang, D., and Gaillard, J.-F., 2010, A multi-scale investigation of interfacial transport, pore fluid flow, and fine particle deposition in a sediment bed: *Water Resour. Res.*, v. 46, W11560.
- Chu, J., Engquist, B., Prodanović, M., and Tsai, R., 2012, A Multiscale Method Coupling Network and Continuum Models in Porous Media I: Steady-State Single Phase Flow: *Multiscale Modeling & Simulation*, v. 10, no. 2, p. 515-549.
- Chu, J., Engquist, B., Prodanović, M., and Tsai, R., 2013, A Multiscale Method Coupling Network and Continuum Models in Porous Media II—Single- and Two-Phase Flows, in Melnik, R., and Kotsireas, I. S., eds., *Advances in Applied Mathematics, Modeling, and Computational Science*, v. 66, Springer US, p. 161-185.
- Cirpka, O. A., Olsson, A., Ju, Q. S., Rahman, M. A., and Grathwohl, P., 2006, Determination of transverse dispersion coefficients from reactive plume lengths; *Ground Water*, v. 44, p. 212–221.
- Craft, B. C., and Hawkins, M. F., 1959, *Applied petroleum reservoir engineering*. United States: Prentice-Hall: Englewood Cliffs, NJ, United States.
- Crank, J., 1975, *The mathematics of diffusion* by J. Crank. Oxford, [Eng]: Clarendon Press.
- Cussler, E. L., 1997, *Diffusion: Mass Transfer in Fluid Systems* (2nd ed.). New York: Cambridge University Press.
- Dakshinamurthy, N., Verma, N. K., Abdul Salam, T., Al-Sammak, I., Koronfol, S., Dernaika, M., and Teh, W. J., 2014, Computation of Relative Permeability Curves in Middle Eastern Carbonates Using Digital Rock Physics: *International Petroleum Technology Conference*.
- Darcy, H., 1856, *Les Fontaines Publiques de la Ville de Dijon*: Victor Dalmond.
- Dodd, C. G., and Kiel, O. G., 1959, Evaluation of Monte Carlo methods in studying fluid-fluid displacement and wettability in porous rock: *J. phys. Chem.*, v. 63, p. 299-324.
- Donaldson, E. C., Baker, B. A., and Carroll, H. B., 1977, *Particle Transport In Sandstones*, Society of Petroleum Engineers.
- Dong, H., and Blunt, M. J., 2009, Pore-network extraction from micro-computerized tomography Images: *Phys. Rev. E*, v. 80, no. 036307.
- Elimelech, M., and O'Melia, C. R., 1990, Kinetics of deposition of colloidal particles in porous Media: *Environ. Sci. Technol.*, v. 24, no. 10, p. 1528–1536.

- Ergun, S., 1952, Fluid flow through packed columns: Chemical Engineering Progress, v. 48, p. 89-94.
- Fatt, I., 1956, The Network Model of Porous Media, Petroleum Transactions: AIME, v. 207, p. 144-181.
- Feng, Q., Li, S., Han, X., and Wang, S., 2015, Network simulation for formation impairment due to suspended particles in injected water: J. Pet. Sci. Eng., v. 133, p. 384-391.
- Ferguson, C. K., and Klotz, J. A., 1954, Filtration From Mud During Drilling, Society of Petroleum Engineers.
- Finney, J., 1968, Ph.D. dissertation: London University.
- Fischer, U., and Celia, M. A., 1999, Prediction of relative and absolute permeabilities for gas and water from soil water retention curves using a pore-scale network model: Water Resour. Res., v. 35, p. 1089–1100
- Fourar M., Radilla, G., Lenormand, R., and Moyne, C., 2004, On the non-linear behavior of a laminar single-phase flow through two and three-dimensional porous media: Adv. Water Resour., v. 27, p. 669–677.
- French, L. B., 2015, Multiscale Modeling of Particle Transport in Petroleum Reservoirs, Master thesis, Department of Petroleum Engineering, Louisiana State University.
- Gao, C., 2007, Factors Affecting Particle Retention In Porous Media: Emirates Journal for Engineering Research, v. 12, no. 3, p. 1-7.
- Gao, C., 2008, Understanding capture of non-Brownian particles in porous media with network model: Asia-Pac. J. Eng., v. 3, no. 3, p. 298–306.
- Geuzaine, C., and Remacle, J.-F., 2009, Gmsh: A 3-D finite element mesh generator with built-in pre- and post-processing facilities: Int. J. Numer. Meth. Engng., v. 79, p. 1309–1331.
- Ghaddar, C. K., 1995, On the permeability of unidirectional fibrous media: A parallel computational approach: Physics of Fluids (1994-present), v. 7, no. 11, p. 2563-2586.
- Golzar, M., Saghravani, S. F., and Moghaddam, M. A., 2014, Experimental Study and Numerical Solution of Poly Acrylic Acid Supported Magnetite Nanoparticles Transport in a One-Dimensional Porous Media: Advances in Materials Science and Engineering, p. 4-6.
- Harris, C. C., 1965, Latin Square as a network model of random packing: Nature, v. 205, p. 535-556.
- Heiba, A. A., Jerauld, G. R., Davis, H. T., and Scriven, L. E., 1986, Mechanism-Based Simulation of Oil Recovery Processes, Society of Petroleum Engineers.

- Herrera, P., 2009, Particle and streamline numerical methods for conservative and reactive transport simulations in porous media, Ph.D. thesis, University of British Columbia.
- Hirsch, C., 2010, Numerical Computation of Internal and External Flows - Fundamentals of Computational Fluid Dynamics (2nd Edition); Elsevier, p. 290-291.
- Huang, T., Crews, J. B., and Willingham, J. R., 2008, Using Nanoparticle Technology to Control Fine Migration, Society of Petroleum Engineers.
- Iassonov, P., Gebrenegus, T., and Tuller, M., 2009, Segmentation of X-ray computed tomography images of porous materials: a crucial step for characterization and quantitative analysis of pore structures: *Water Resour. Res.*, v. 45.
- Iassonov, P., and Tuller, M., 2010, Application of segmentation for correction of intensity bias in X-ray computed tomography images: *Vadose Zone J.*, v. 9, no. 1, p. 187–91.
- Imdakm, A. O., and Sahimi, M., 1987, Transport of large particles in flow through porous media: *Physical Review A*, v. 36, no. 11, p. 5304-5309.
- Imdakm, A. O., and Sahimi, M., 1991, Computer simulation of particle transport processes in flow through porous media: *Chemical Engineering Science*, v. 46, no. 8, p. 1977-1993.
- Jha, R. K., Bryant, S., and Lake, L. W., 2011, Effect of Diffusion on Dispersion: Society of Petroleum Engineers.
- John, D. E., and Rose, J. B., 2005, Review of factors affecting microbial survival in Groundwater: *Environ. Sci. Technol.*, v.39, no. 19, p. 7345– 7356.
- Kim, D., Peters, C. A., and Lindquist, W. B., 2011, Upscaling geochemical reaction rates accompanying acidic CO<sub>2</sub>-saturated brine flow in sandstone aquifers: *Water Resour. Res.*, v. 47, W01505.
- Kozeny, J., 1927, Ueber kapillare Leitung des Wassers im Boden: *Sitzungsber Akad. Wiss., Wien*, v. 136, no. 2a, p. 271-306.
- Lane, N. and Thompson, K. E., 2010, Image-Based Pore-Scale Modeling using the Finite Element Method, In: *Advances in Computed Tomography for Geomaterials: GeoX 2010*. Eds. K.A. Alshibli and A.H. Reed.
- Leonard, B. P., 1979, A stable and accurate convection modelling procedure based on quadratic upstream interpolation: *Comput. Meth. Appl. Mech. Eng.* 19, 59.
- Leonard, B.P., 1993, Order of Accuracy of QUICK and Related Convection-Diffusion Schemes; Technical Report NASA TM 106402.
- Li, L., Peters, C. A., and Celia, M. A., 2006, Upscaling geochemical reaction rates using pore-scale network modeling, *Adv: Water Resour.*, v. 29, p. 1351–1370.

- Li, X. Q., Scheibe, T. D., and Johnson, W. P., 2004, Apparent decreases in colloid deposition rate coefficients with distance of transport under unfavorable deposition conditions: A general phenomenon: *Environ. Sci. Technol.*, v. 38, no. 21, p. 5616–5625.
- Li, Z., Zhang, D. X., and Li, X., 2010, Tracking colloid transport in porous media using discrete flow fields and sensitivity of simulated colloid deposition to space discretization: *Environ. Sci. Technol.*, v. 44, no. 4, p. 1274–1280.
- Lindquist, W.B., and Venkatarangan, A., 1999, Investigating 3D geometry of porous media from high resolution images: *Phys. Chem. Earth A*, v. 25, no. 7, p. 593–599.
- Long, W., and Hilpert, M., 2009, A correlation for the collector efficiency of Brownian particles in clean-bed filtration in sphere packings by a Lattice-Boltzmann method: *Environ. Sci. Technol.*, v. 43, no. 12, p. 4419–4424.
- Mayo, S. C., Davis, T. J., Gureyev, T. E., Miller, P. R., Paganin D., Pogany, A., Stevenson, A. W., and Wilkins, S. W., 2003, X-ray phase-contrast microscopy and microtomography: *Opt. Express*, v. 11, p. 2289–2302.
- McCain, W. D. Jr., Spivey, J. P., and Lenn, C. P., 2011, *Petroleum Reservoir Fluid Property Correlations*: PennWell.
- McDowell-Boyer, L. M., Hunt, J. R., and Sitar, N., 1986, Particle transport through porous media: *Water Resour. Res.*, v. 22, no. 13, p. 1901–1921.
- Mehmani, Y., and Balhoff, M. T., 2015a, Mesoscale and hybrid models of fluid flow and solute Transport: *Rev. Mineral Geochem*, v. 80, p. 433–459.
- Mehmani, Y., and Balhoff, M. T., 2015b, Eulerian network modeling of longitudinal dispersion: *Water Resour. Res.*, v. 51, p. 8586–8606.
- Mehmani, Y., Oostrom, M., and Balhoff, M. T., 2014, A streamline splitting pore-network approach for computationally inexpensive and accurate simulation of species transport in porous media: *Water Resour. Res.*, v. 50, p. 2488–2517.
- Mehmani, Y., Sun, T., Balhoff, M. T., Eichhubl, P., and Bryant, S., 2012, Multiblock pore-scale modeling and upscaling of reactive transport: Application to carbon sequestration: *Transp. Porous Media*, v. 95, no. 2, p. 305–326.
- Mohanty K. K., Davis, H. T., and Scriven, L. E., 1987, *Physics of oil entrapment in water-wet rock*, Society of Petroleum Engineers.
- Molnar, L. L., Johnson, W. P., Gerhard, J. I., Willson, C. S., and O’Carroll, D. M., 2015, Predicting colloid transport through saturated porous media: A critical review: *Water Resour. Res.*, v. 51, no. 9, p. 6804–6845.



- Nicholson, D., and Petropoulos, J. H., 1971, Capillary models for porous media: III. Two-phase flow in a three-dimensional network with Gaussian radius distribution: *J. Phys. D: Appl. Phys.*, v. 4, p. 181-189.
- Nicholson, D., and Petropoulos, J. H., 1975, Capillary models for porous media: V. Flow properties of random networks with various radius distributions: *J. Phys. D: Appl. Phys.*, v. 8, p. 1430-1440.
- Ogata, A., and Banks, R. B., 1961, A solution of the differential equation of longitudinal dispersion in porous media; *U.S. Geol. Surv. Prof. Pap.*, 411-A.
- Øren P-E, and Bakke, S, 2002, Process based reconstruction of sandstones and prediction of transport properties: *Transport Porous Med.*, v. 46, p. 311–343.
- Pan, C., Hilpert, M., and Miller, C. T., 2004, Lattice-Boltzmann simulation of two-phase flow in porous media: *Water Resour. Res.*, v. 40.
- Payatakes, A. C., Ng, K. M., and Flumerfelt, R. W., 1980, Oil ganglion dynamics during immiscible displacement: Model formulation: *AIChE J.*, v. 26, no. 3, p. 430–443.
- Payatakes, A. C., Rajagopalan, R., and Tien, C., 1974a, Application of porous media models to the study of deep bed filtration: *Can. J. chem. Engng.*, v. 52, p. 722-731.
- Payatakes, A. C., Tien, C., and Turian, R. M., 1973, A new model for granular porous media: *AIChE J.*, v. 19, p. 58-76.
- Payatakes, A. C., Tien, C., and Turian, R. M., 1974b, Trajectory calculation of particle deposition in deep bed filtration: *AIChE J.*, v. 20, p. 889-905.
- Peaceman, D. W., 1977, Interpretation of Well-Block Pressures in Numerical Reservoir Simulation, Society of Petroleum Engineers.
- Petra, C. G., Schenk, O., and Anitescu, M., 2014, Real-time stochastic optimization of complex energy systems on high-performance computers: *IEEE Computing in Science & Engineering*, v. 16, no. 5, p. 32-42.
- Porubcan, A. A., and S. Xu, 2011, Colloid straining within saturated heterogeneous porous media, *Water Res.*, v. 45, no. 4, p. 1796–1806.
- Rahmani, A. R., Bryant, S. L., Huh, C., Ahmadian, M., Zhang, W., and Liu, Q. H., 2015, Characterizing Reservoir Heterogeneities Using Magnetic Nanoparticles, Society of Petroleum Engineers.
- Rajagopalan, R., Tien, C., 1976, Trajectory analysis of deep-bed filtration with the sphere-in-cell porous media model: *AIChE J.*, v. 22, no. 3, p. 523–533.

- Ramstad, T., Oren, P. E., and Bakke, S., 2009, Simulation of Two Phase Flow in Reservoir Rocks Using a Lattice Boltzmann Method, Society of Petroleum Engineers.
- Reeves, P. C., and Celia, M. A., 1996, A Functional Relationship Between Capillary Pressure, Saturation, and Interfacial Area as Revealed by a Pore-Scale Network Model: *Water Resour. Res.*, v. 32, no. 8, p. 2345–2358.
- Rege, S. D., and Fogler, H. S., 1987, Network Model for Straining Dominated Particle Entrapment in Porous-Media: *Chemical Engineering Science*, v. 42, no. 7, p. 1553-1564.
- Rege, S. D., and Fogler, H. S., 1988, A Network Model for Deep Bed Filtration of Solid Particles and Emulsion Drops: *AIChE J.*, v. 34, no. 11, p. 1761-1772.
- Rhodes, M. E., Bijeljic, B., and Blunt, M. J., 2008, Pore-to-field simulation of single-phase transport using continuous time random walks: *Advances in Water Resources*, v. 31, no. 12, p. 1527-1539.
- Rhodes, M. E., and Blunt, M. J., 2006, An exact particle tracking algorithm for advective-dispersive transport in networks with complete mixing at nodes: *Water Resour. Res.*, v. 42, no. 4.
- Rink, M., and Schopper, J. R., 1968, Computations of network models of porous media: *Geophys. Prospect.*, v. 16, p. 277-297.
- Sahimi, M., Gavalas, G. R., and Tsotsis, T. T., 1990, Statistical and continuum models of fluid-solid reactions in porous media: *Chem. Eng. Sci.*, v. 45, no. 6, p. 1443-1502.
- Salama, M. M., 1998, Sand Production Management: Offshore Technology Conference.
- Scheibe, T. D., Tartakovsky, A. M., Tartakovsky, D. M., Redden, G. D., and Meakin, P., 2007, Hybrid numerical methods for multiscale simulations of subsurface biogeochemical processes: *J. Phys:Conf Ser* 78:012063. IOP Publishing.
- Seetha, N., Raoof, A., Mohan Kumar, M. S., and Majid Hassanizadeh, S., 2017, Upscaling of nanoparticle transport in porous media under unfavorable conditions: Pore scale to Darcy scale: *Journal of Contaminant Hydrology*, v. 200, p. 1-14.
- Sharma, M. M., 1985, Transport of Particulate Suspensions in Porous Media: Applications to Filtration and Formation Damage in Sandstones: Ph.D. Diss., Univ. So. California.
- Sharma, M. M., Pang, S., Wennberg, K. E., and Morgenthaler, L. N., 1997, Injectivity decline in water-injection wells: An offshore Gulf of Mexico case study: *SPE Prod. Facil. J.*, v. 15, no. 1, p. 6–13.
- Sharma, M. M., and Yortsos, Y. C., 1987a, Transport of particulate suspensions in porous media: model formulation: *AIChE J.* v. 33, p. 1636-1643.

- Sharma, M. M., and Yortsos, Y. C., 1987b, A network model for deep bed filtration processes: *AIChE J.*, v. 33, no. 10, p. 1644-1653.
- Shen, Y., 2014, Image-Based Pore-Scale Modeling of Inertial Flow in Porous Media and Propped Fractures: *LSU Doctoral Dissertations*, 1000.
- Sheng, Q., and Thompson, K. E., 2013, Dynamic coupling of pore-scale and reservoir-scale models for multiphase flow: *Water Resour. Res.*, v. 49, no. 9, p. 5973–5988.
- Sheng, Q., Thompson, K. E., Fredrich, J. T., and Salino, P. A., 2011, Numerical Prediction of Relative Permeability from MicroCT Images: Comparison of Steady-State versus Displacement Methods, *Society of Petroleum Engineers*.
- Shopper, J. R., 1966, A theoretical investigation of the formation factor/permeability/porosity relationship using a network model: *Geophys. Prospect.*, v. 14, p. 301-310.
- Silin, D., and Patzek, T., 2006, Pore space morphology analysis using maximal inscribed spheres: *Physica A*, v. 371, p. 336–360.
- Siqueira, A. G., Bonet, E. J., and Shecaira, F. S., 2003, A 3D Network Model of Rock Permeability Impairment Due to Suspended Particles in Injection Water, *Society of Petroleum Engineers*.
- Socolofsky, S. A., and Jirka, G. H., 2005, Special Topics in Mixing and Transport Processes in the Environment: Engineering – Lectures, fifth ed., Coastal and Ocean Engineering Division, Texas A&M University
- Soo, H., and Radke, C. J., 1984. The flow mechanism of dilute stable emulsions in porous media: *Ind. Engng Chem. Fundam.*, v. 23, p. 342-347.
- Soo, H., and Radke, C. J., 1985, Flow of dilute stable liquid and solid dispersions in porous media: *AIChE J.*, v. 31, p. 1926-1929.
- Soo, H., and Radke, C. J., 1986, A filtration model for the flow of dilute, stable emulsions in porous media - I. Theory: *Chem. Engng. Sci.*, v. 41, no. 2, p. 263-272.
- Sun, T., Mehmani, Y., and Balhoff, M. T., 2012, Hybrid multiscale modeling through direct substitution of porescale models into near-well reservoir simulators: *Energy & Fuels*, v. 26, no. 9, p. 5828–5836.
- Tartakovsky, A. M., Meakin, P., Scheibe, T. D., and EichlerWest, R. M., 2007, Simulations of reactive transport and precipitation with smoothed particle hydrodynamics: *J. Comput. Phys.*, v. 222, no. 2, p. 654–672.
- Thibodeaux, T. W., 2018, Image-based Modeling of Flow through Porous Media: Development of Multiscale Techniques for the Pore Level. *LSU Doctoral Dissertations*.

- Thompson, K. E., Willson, C. S., White, C. D., Nyman, S., Bhattacharya, J. P., and Reed, A. H., 2008, Application of a new grain-based reconstruction algorithm to microtomography images for quantitative characterization and flow modeling, Society of Petroleum Engineers.
- Thovert, J. F., Salles, J., and Adler, P. M., 1993, Computerized characterization of the geometry of real porous media: their discretization, analysis and interpretation: *J. Microsc.*, v. 170, p. 65–79.
- Tien, C., and Payatakes, A. C., 1979, Advances in Deep Bed Filtration: *AIChE J.*, v. 25, no. 5, p. 737-759.
- Todd, A.C., Somerville, J.E. and Scott, G., 1984, The application of depth of formation damage measurements in predicting water injectivity decline, Society of Petroleum Engineers.
- Tufenkji, N., and M. Elimelech, 2004, Deviation from the classical colloid filtration theory in the presence of repulsive DLVO interactions, *Langmuir*, v. 20, no. 25., p. 10,818–10,828.
- United Nations, 2003, Water for people, water for life: UNESCO-WWAP, Paris.
- Van den Akker, H. E. A., 2010, Toward A Truly Multiscale Computational Strategy For Simulating Turbulent Two-Phase Flow Processes: *Industrial & Engineering Chemistry Research*, v. 49, no. 21, p. 10780-10797.
- Van Es, B., Koren, B., de Blank, H., 2014, Finite-difference schemes for anisotropic diffusion; *J. Comput. Phys.*, v. 272, p. 526–549.
- Van Genuchten, M.Th., and Alves, W. J., 1982, Analytical Solutions of the One-Dimensional Convective-Dispersive Solute Transport Equation; Technical Bulletin 1661, US Department of Agriculture, Washington DC.
- Vetter, O.J., Kandarpa, V., Stratton, M. and Veith, E., 1987, Particle invasion into porous medium and related injectivity problems, Society of Petroleum Engineers.
- Wenrong, M., Shihong, S., Tianhua, L., Wenzhong, L., and Guoheng, H., 1996, Pore and Throat Network Model and Its Application to the Optimal Selection of Temporary Plugging Particles, Society of Petroleum Engineers.
- Wildenschild, D., and Sheppard, A. P., 2012, X-ray imaging and analysis techniques for quantifying pore-scale structure and processes in subsurface porous medium systems: *Adv. Water Resour.*, v. 51, p. 217–246.
- Xiong, Q., Baychev, T. G., and Jivkov, A. P., 2016, Review of pore network modelling of porous media: Experimental characterisations, network constructions and applications to reactive transport: *Journal of Contaminant Hydrology*, v. 192, p. 101-117.

- Xu, S., and J. E. Saiers, 2009, Colloid straining within water-saturated porous media: Effects of colloid size nonuniformity, *Water Resour. Res.*, v. 45.
- Yang, H., and Balhoff, M. T., 2017, Pore-network modeling of particle retention in porous media: *AIChE J.*, v. 63, no. 7, p. 3118–3131.
- Yang, X., Mehmani, Y., Perkins, W. A., Pasquali, A., Schönherr, M., Kim, K., Perego, M., Parks, M. L., Trask, N., Balhoff, M. T., Richmond, M. C., Geier, M., Krafczyk, M., Luo, L.-S., Tartakovsky, A. M., Scheibe, T. D., 2015, Intercomparison of 3D pore-scale flow and solute transport simulation methods: *Adv. Water Resour.*, v. 95, p. 176–189.
- Yao, K. M., Habibian, M. T., and O'Melia, C. R., 1971, Water and waste water filtration: Concepts and applications: *Environ. Sci. Technol.*, v. 5 no. 11, p. 1105–1112.
- Yoon, J. S., Germaine, J. T., and Culligan, P. J., 2006, Visualization of particle behavior within a porous medium: mechanisms for particle filtration and retardation during downward transport: *Water Resour. Res.*, v. 42, no. 6, p. 1–16.
- Zhang, T., Roberts, M., Bryant, S. L., and Huh, C., 2009, Foams and Emulsions Stabilized With Nanoparticles for Potential Conformance Control Applications, *Society of Petroleum Engineers*.
- Zheng, C., and Wang, P. P., 1999, MT3DMS: A Modular Three-Dimensional Multispecies Transport Model for Simulation of Advection, Dispersion, and Chemical Reactions of Contaminants in Groundwater Systems: Documentation and User's Guide: Alabama University, Tuscaloosa, AL.

## **Vita**

John Rayner Blears, also known as Jack, was born in Chicago, Illinois and received his bachelor's degree in physics from Washington University in St. Louis in 2013. Wanting to work in the field of energy, Jack decided to pursue a master's degree in petroleum engineering at Louisiana State University, which he completed in 2015. Jack continued his education in the field of petroleum engineering, enrolling in the PhD program directly following his master's degree. In January 2019, while continuing to perform research towards his doctoral degree, Jack began working as a consultant for Darcy Partners to help to speed the adoption of novel technologies in the oil and gas industry. Jack intends to complete his doctoral degree in December 2019.